



Arnold Schwarzenegger
Governor

California Regional Wind Energy Forecasting System Development Volume 3: Wind Tunnel Modeling of Wind Flow over Complex Terrain

Prepared For:

California Energy Commission
Public Interest Energy Research Program

Prepared By:

Electric Power Research Institute, Inc.



PIER FINAL TASK REPORT

September 2006
CEC-500-2006-089



Prepared By:

Electric Power Research Institute, Inc.
C. McGowin and P. Hirsch
Palo Alto, CA, 94303
Contract No. 500-02-014
Work Authorization WA-111

Prepared For:

Public Interest Energy Research (PIER) Program
California Energy Commission

Michael Kane
Dora Yen-Nakafuji
Contract Manager

Elaine Sison-Lebrilla
Program Area Team Lead

Elaine Sison-Lebrilla
Manager
Energy Generation Research Office

Martha Krebs, Ph. D.
Deputy Director
Energy Research and Development Division

B.B. Blevins
Executive Director

DISCLAIMER

This report was prepared as the result of work sponsored by the California Energy Commission. It does not necessarily represent the views of the Energy Commission, its employees, or the State of California. The Energy Commission, the State of California, its employees, contractors and subcontractors make no warrant, express or implied, and assume no legal liability for the information in this report; nor does any party represent that the uses of this information will not infringe upon privately owned rights. This report has not been approved or disapproved by the California Energy Commission nor has the California Energy Commission passed upon the accuracy or adequacy of the information in this report.

CITATIONS

This report was prepared by

University of California Davis, Department of Mechanical and Aeronautical Engineering
One Shields Avenue
Davis, CA 95616-5294

Principal Investigators

B. White

W. Lubitz

This report describes research sponsored by EPRI and the California Energy Commission.

The report is a corporate document that should be cited in the literature in the following manner:

California Regional Wind Energy Forecasting System Development, Volume 3: Wind Tunnel Modeling of Wind Flow over Complex Terrain, Electric Power Research Institute, Palo Alto, CA, and California Energy Commission, Sacramento, CA: 2006. 1013264.

PRODUCT DESCRIPTION

The rated capacity of wind generation in California is expected to grow rapidly in the future beyond the approximately 2100 MW in place at the end of 2005. The main drivers are the state's 20 percent Renewable Portfolio Standard requirement in 2010 and the low cost of wind energy relative to other renewable energy sources.

As wind is an intermittent generation resource and weather changes can cause large and rapid changes in output, system operators will need accurate and robust wind energy forecasting systems in the future. In response to this need, the California Energy Commission (Energy Commission) and EPRI initiated the California Regional Wind Energy Forecasting System Development Project in 2003 to develop and test short- and intermediate-term (for example, next-hour and next-day) forecast algorithms with improved forecast accuracy relative to the results of a previous project completed in 2002.

Volume 3 of the final report presents the detailed results of the research on wind tunnel and empirical modeling of wind flow over the complex terrain at Altamont Pass. Volumes 1, 2, and 4 present the executive summary of the research results and the detailed results of the research on short- and intermediate-term forecasting, high-resolution wind flow modeling over complex terrain, and development of the California Wind Generation Research Dataset (CARD).

Results and Findings

Wind tunnel testing of a scale model of a portion of the Altamont Pass wind resource area demonstrated the complex wind flow and the variation of wind speeds and power densities between individual wind turbines and nearby meteorological towers. Wind energy forecasts based on an empirical method that matches conditions to historical conditions provided more accurate forecasts than persistence.

Challenges and Objectives

Electricity systems with significant intermittent wind capacity create a challenge to the system operator. Rapid changes of wind generation relative to load require rapid dispatching of generation and transmission resources to balance generation vs. load, regulate voltage and frequency, and maintain system performance within limits established by Control Performance Standards 1 and 2 (CPS1 and CPS2). This is especially true during periods when wind generation is fluctuating rapidly relative to system load, for example, during passage of thunderstorms and weather fronts. Wind energy forecasts can help the system operator anticipate rapid changes of wind energy generation vs. load and make informed decisions. The overall project objectives are

to develop and demonstrate the capabilities of wind energy forecasting technology for both same-day and longer-term forecasts.

Applications, Values, and Use

The wind plant power curve developed via wind tunnel testing of a scale model of the wind plant site provides a superior method for estimating wind generation as a function of wind speed, direction, and other conditions measured by a nearby meteorological tower, especially in complex terrain as exists at Altamont Pass.

EPRI Perspective

The wind tunnel and empirical modeling described in this report addressed the variability of wind turbine/meteorological tower wind speed ratios between adjacent turbines and the performance of a forecasting algorithm based on numerical weather forecasts and the model results. Together with the complementary high-resolution numerical modeling described in Volume 2, this research is likely to contribute to further improvements in the accuracy of both next-hour and next-day wind power forecasting. Other volumes of the final report include Volume 1 (Executive Summary, 1013262), Volume 2 (Next-Hour and Next-Day Forecasting, 1013263), and Volume 4 (California Wind Generation Research Dataset (CARD), 1013265).

It is important to continue research on wind energy forecasting in California both to implement the forecast algorithms to provide real-time forecasts to utility and the California Independent System Operator (CA ISO) system operators and to complete the development and testing of accurate same-day and next-day forecast algorithms.

Approach

Researchers developed wind tunnel and “empirical” plant-scale power curves for a wind farm in the Altamont Pass, California; investigated wind flow over generalized terrain in the wind tunnel to inform development of the empirical power curve method; and developed and operated an automated wind power forecasting system that operates on a desktop PC. The forecast system uses a database searching technique to forecast power production

ABSTRACT

The rated capacity of wind generation in California is expected to grow rapidly in the future beyond the approximately 2100 MW in place at the end of 2005. The main drivers are the state's 20 percent Renewable Portfolio Standard requirement in 2010 and the low cost of wind energy relative to other renewable energy sources.

As wind is an intermittent generation resource and weather changes can cause large and rapid changes in output, system operators will need accurate and robust wind energy forecasting systems in the future. In response to this need, the California Energy Commission (Energy Commission) and EPRI initiated the California Regional Wind Energy Forecasting System Development Project in 2003 to develop and test short- and intermediate-term (for example next-hour and next-day) forecast algorithms with improved forecast accuracy relative to the results of a previous project completed in 2002.

Volume 3 of the final report presents the detailed results of the research on wind tunnel and empirical modeling of wind flow over the complex terrain at Altamont Pass. Volumes 1, 2, and 4 present the executive summary of the research results and the detailed results of the research on short- and intermediate-term forecasting, high-resolution wind flow modeling over complex terrain, and development of the California Wind Generation Research Dataset (CARD).

Wind tunnel investigations were conducted of the effect of wind direction and hill geometry on wind speed-up above a hill. Field data from an Altamont Pass, California, site were used to evaluate several speed-up prediction algorithms, both with and without wind direction adjustment. These algorithms were found to be of limited usefulness for the complex terrain case evaluated. Wind tunnel and numerical simulation-based methods were developed for determining a wind farm power curve (the relation between meteorological conditions at a point in the wind farm and the power production of the wind farm). Together with two other methods based on fits to historical data, the methods ultimately exhibited similar power production forecast performance, with annual mean absolute errors of 5 to 7 percent of rated wind capacity. A series of experiments and investigations were conducted to inform the development of a day-ahead wind power forecasting system. An experimental near-real time wind power forecasting system was designed and constructed that operates on a desktop PC and forecasts 12 to 48 hours in advance. The system uses model output of the Eta regional-scale forecast (RSF) to forecast the power production of a wind farm in the Altamont Pass, California, from 12 to 48 hours in advance. The complex terrain at Altamont Pass complicates wind flow and therefore downscaling of the RSF forecast data to the wind farm. Because forecasts based on application of the geostrophic drag law and regression methods to predict surface wind speeds did not perform well, an alternate database matching method was developed. The method searches for the historical date that provides the best match to current conditions, and the forecast is based on

the historical data for that date. Testing showed the alternate method forecasts both wind speed and power production more accurately than persistence

Keywords

Wind power, Wind resource data, Wind tunnel testing, Wind energy forecasting, Altamont Pass, California

ACKNOWLEDGEMENTS

Several organizations and individuals contributed to and provided data and information for the California Regional Wind Energy Forecasting System Development Project addressed in this and other volumes of the final report. They include Dr. Dora Yen-Nakafuji and Michael Kane of the California Energy Commission; David Hawkins of the California Independent System Operator (CA ISO); Dr. Marc Schwartz of the National Renewable Energy Laboratory (NREL); Dr. Robert Farber of Southern California Edison (SCE); Cliff Murley of the Sacramento Municipal Utility District (SMUD); Mark Smith of FPL Energy; Julie Morris of PPM Energy; Rick Koebbe and Bob Szymanski of Pacific Winds, Inc./PowerWorks; Inc.; Ed Duggan and Jeremiah Sota of Oak Creek Energy Systems; Brian Ulberg MDU Resources; John Zack, Kenneth T. Waight III, Pamela Barlow, Joe Nocera, and Dan Mead of AWS Truewind, LLC; Professor Bruce White and Dr. David Lubitz of the University of California at Davis; and Dr. Steve Chin of Lawrence Livermore National Laboratory (LLNL). The project was supported by the Public Interest Energy Research Program of the California Energy Commission.

CONTENTS

- 1 INTRODUCTION 1-1**
 - First Energy Commission-EPRI Wind Energy Forecasting Project, 2001-2003..... 1-2
 - Current Regional Wind Energy Forecasting System Development Project, 2004-2005 1-2
 - Objectives and Scope 1-3
 - Report Organization 1-3

- 2 ATMOSPHERIC BOUNDARY LAYER WIND TUNNEL APPLICATION TO WIND ENERGY FORECASTING..... 2-1**
 - UC Davis Atmospheric Boundary Layer Wind Tunnel..... 2-1
 - Simulation of the Atmospheric Boundary-Layer 2-3
 - Altamont Pass 2-4
 - Eta Regional Scale Forecast..... 2-7

- 3 WIND SPEED-UP OVER HILLS 3-1**
 - Speed-Up Prediction Background 3-1
 - Speed-Up At Altamont Pass..... 3-5
 - Wind Tunnel Tests of Generalized Hills 3-10
 - Test Specifications 3-10
 - Hill Models 3-10
 - Effects of Model Roughness..... 3-13
 - Two-Dimensional Ridge and Three-Dimensional Circular Hill..... 3-13
 - Hill Aspect Ratio 3-14
 - Hill Shoulder 3-15
 - Effects of Wind Direction 3-15
 - Analysis of Prediction Schemes 3-21
 - Modified LSD Prediction Scheme..... 3-23
 - Generalized Hill Test Conclusions..... 3-24

- 4 THE WIND FARM POWER CURVE..... 4-1**

Power Curve Derived From Wind Tunnel Data.....	4-1
Wind Tunnel Modeling of Altamont Pass Terrain	4-1
Atmospheric Stability.....	4-7
Error Assessment of Prediction Scheme.....	4-8
Error Levels of Power Production Prediction Schemes: July 1, 2001 – June 30, 2003.....	4-10
Error Bias.....	4-14
Atmospheric Stability.....	4-14
Predictions Of Zero Power Production	4-15
Characteristics of the Error in the Prediction Schemes	4-17
Figure 4-6 Predicted versus actual power production for the Met 127 turbine cluster between July 1, 2001 and June 30, 2003	4-18
Comparison of Predictions with Varying Input Wind Speeds	4-18
Optimum Prediction Scheme for Met 127.....	4-19
Predicting Power Using A Statistically-Derived Equation.....	4-20
Power Curve Based on Curve Fitting Historical Data.....	4-21
Power Curve Based On Numerical Simulation.....	4-21
Two-Dimensional Potential Flow Simulation	4-22
Determining Speed-Up Factor	4-26
Program Implementation	4-26
Iteration and Convergence	4-29
Initial Validation: Cosine Hills	4-31
Powerworks Meteorological Towers.....	4-32
Power Curve Generation Using the Potential Flow Solver	4-33
Altamont Wind Farm Power Prediction Accuracy.....	4-34
Forecasting with the Power Curves.....	4-37
5 DOWNSCALING AND FORECASTING	5-1
Uncertainty of the Eta Regional Scale Forecast (RSF).....	5-1
Comparison of Interpolation Methods: Bicubic, Bilinear, and Nearest Point	5-1
Downscaling.....	5-4
Geostrophic Drag Law.....	5-4
Multiple Linear Regression	5-6
Forecast Matching.....	5-6
Comparison of Matching Method to Persistence.....	5-8
Confidence Interval Estimation.....	5-8

Comparison of Different Matching Variables.....	5-8
Times-Series Matching.....	5-10
Comparison to Other Forecasting Methods.....	5-10
Effect of Database Size.....	5-14
Matching Using Different Input Regional Scale Forecasts	5-16
6 CONCLUSIONS	6-1
7 REFERENCES	7-1
A APPENDIX - MET 127 R VALUES DETERMINED BY ABLWT AND POTENTIAL FLOW SIMULATIONS.....	A-1

LIST OF FIGURES

Figure 1-1 California Mean Wind Power Map at 50-m Elevation and 2005 Rated Capacity of Wind Generation at Principal Wind Resource Areas (California Energy Commission, 2006)	1-1
Figure 2-1 Schematic of UC Davis wind power forecasting system	2-1
Figure 2-2 Schematic of UC Davis Atmospheric Boundary Layer Wind Tunnel	2-3
Figure 2-3 Location of Altamont Pass, California.....	2-5
Figure 2-4 Wind speed vs. direction at Altamont Pass Met 127 meteorological tower during January, 2003 (left), showing typical winter winds, and June 2003 (right), showing typical summer winds.....	2-6
Figure 2-5 Locations of Eta model grid points in the vicinity of the Altamont Pass wind farm.....	2-8
Figure 3-1 Map of western side of Altamont Pass showing location of LLNL meteorological tower and Powerworks meteorological towers 438 and 624. North is up.	3-6
Figure 3-2 Elevation transect from LLNL meteorological tower to Met 438. Dotted line shows hill slope approximation used for prediction schemes.....	3-6
Figure 3-3 Average speed-up factor at Meteorological Tower 438 as a function of wind direction relative to the perpendicular to the ridgeline.....	3-9
Figure 3-4 Roughness element arrangement used in ABLWT development section for generalized hill tests. The two-dimensional hill model at $\theta = 0^\circ$ and the measurement probe support with sighting laser and height probe installed are also visible.	3-11
Figure 3-5 Dimensionless velocity profiles in empty UC Davis Atmospheric Boundary Layer Wind Tunnel test section with artificial grass covering floor at three locations: at center, and 68 cm upwind, and downwind of center.	3-12
Figure 3-6 Schematic diagram of the hill models.....	3-12
Figure 3-7 Hilltop speed-up factor profiles for four hill aspect ratios: $A = 0.25, 1, 4$ and infinity. WT is the wind tunnel measurement. LSD is the predicted speed-up using Eqn. 3.9b with $C1 = 2.3, C2 = 0.2, C3 = 2.0$	3-14
Table 3-5 Measured values of ΔS at the shoulder location ($x = 0, y = L2, \theta = 0^\circ$) at different heights above ground z , for hills of different aspect ratio $A = L2/L1$	3-15
Figure 3-8 Speed-up factor versus wind direction for two-dimensional hill at hilltop. Wind from 0° is perpendicular to ridgeline.....	3-16
Figure 3-9 Speed-up factor versus wind direction for two-dimensional hill at half-height on slope (“face”). Wind from 0° is perpendicular to ridgeline, with measurement point on windward side..	3-17

Figure 3-10 Speed-up factor versus wind direction for two-dimensional hill at base of hill. Wind from 0° is perpendicular to ridgeline, with measurement point on windward side.....	3-18
Figure 3-11 Speed-up factor versus wind direction for elliptical hill at hilltop. The wind direction from 0° is perpendicular to the ridgeline, from the 90° wind direction is parallel to the ridgeline.	3-18
Figure 3-12 Speed-up factor versus wind direction for elliptical hill at half-height on slope. Wind from 0° is perpendicular to ridgeline, with measurement point on windward side. Wind from 90° is parallel to ridgeline.....	3-19
Figure 3-13 Speed-up factor versus wind direction for elliptical hill at base of hill. Wind from 0° is perpendicular to ridgeline, with measurement point on windward side. Wind from 90° is parallel to ridgeline.....	3-19
Figure 3-14 Speed-up factor versus height for circular hill at hilltop at top, face and base.....	3-20
Figure 3-15 Speed-up factor versus wind direction for circular hill at half-height on slope. Point is centered on upwind face when wind is from 0°. Point is on shoulder of hill when wind is from 90°.....	3-20
Figure 3-16 Speed-up factor versus wind direction for circular hill at base of hill.....	3-21
Figure 3-17 Speed-up factors for the two-dimensional hill top at $z = 10$ mm predicted by the non-linear Weng et al. formulation, using four different wind direction interpolation methods.....	3-22
Figure 4-1 Model in wind tunnel simulating 60° wind direction.	4-3
Figure 4-2 Model in wind tunnel simulating 150° wind direction.	4-4
Figure 4-3 Map of modeled terrain, with area covered by model panels outlined.....	4-4
Figure 4-4 Curve fit predicting dimensionless wind speed (R) as a function of wind direction in radians.....	4-5
Figure 4-5 Power curve for a Kennetech 56-100 100 kW rated wind turbine.	4-6
Figure 4-6 Predicted versus actual power production for the Met 127 turbine cluster between July 1, 2001, and June 30, 2003	4-18
Figure 4-7 Grid layout and variable definitions used in Potential10.f90.....	4-25
Figure 4-8 Example of the effect of lee slope filling (ALPHA = 0.12) on the Met 926 359° terrain transect.....	4-28
Figure 4-9 Potential flow solver predictions of hill top speed-up factor versus height for cosine cross-section hills of varying h/L	4-31
Figure 4-10 Hilltop speed-up factors predicted for cosine hill of $h/L = 0.54$ by empirical prediction methods, potential flow solver and UC Davis wind tunnel.....	4-32
Figure 4-11 Potential10.f90 predictions of speed-up factor as a function of wind direction for the Powerworks meteorological towers.	4-33
Figure 4-12 Mean absolute error (MAE) of Met 127 power predictions versus wind speed, as a percentage of observed wind farm capacity.	4-36
Figure 4-13 Mean absolute error (MAE) of Met 127 power predictions versus actual Met 127 power production, as percentages of observed wind farm capacity.....	4-36
Figure 5-1 Map of Altamont Pass site ("Site") and Oakland radiosonde site ("OAK"). Elevations in meters.....	5-1

Figure 5-2 Mean absolute error in Eta forecasted wind speed at Oakland sounding location for four different levels, as a percentage of the average measured wind speed observed at that level.	5-3
Figure 5-3 Mean absolute error in Eta forecasted wind speed at Oakland sounding location for four different levels (Continued)	5-4
Figure 5-4 Comparison of the wind speed measured at the meteorological tower versus the wind speed at the 700 mb level of the Eta initialization ("zero-hour forecast") runs.	5-7
Figure 5-5 Mean absolute errors of match and persistence forecasts as functions of forecast interval. Forecasts were performed for the period, Nov. 30, 2002, and July 31, 2004.	5-9
Figure 5-6 Comparison of Met 127 wind speed forecast MAE versus the standard deviation of the Met 127 wind speed in the 25 closest matching historical forecasts.	5-9
Figure 5-7 Mean absolute error of time-series matching and persistence forecasts of total Altamont power production between July 2001 and June 2004.	5-11
Figure 5-8 Mean absolute error (MAE) of the match and persistence forecasts as a function of wind speed. January 1 to December 31, 2004.	5-12
Figure 5-9 Mean absolute error (MAE) of the match and persistence forecasts as a function of month for the period January 1 to December 31, 2004.	5-13
Figure 5-10 Mean absolute error (MAE) of the match and persistence forecasts as a function of wind speed. January 1 to December 31, 2004.	5-13
Figure 5-11 Mean absolute error (MAE) versus forecast interval for persistence, small database match and large database match temperature forecasts.	5-15
Figure 5-12 Mean absolute error (MAE) versus forecast interval for persistence, small database match and large database match wind speed forecasts. Forecast period November 30, 2002, to July 31, 2004	5-15
Figure 5-13 Mean absolute error (MAE) versus forecast interval for persistence, small database match and large database match power production forecasts. Forecast period is November 30, 2002, to July 31, 2004.....	5-16
Figure 5-14 Mean absolute errors of the Eta- and COAMPS-based power production match forecasts as functions of the forecast interval during the period, June 1, 2004 to May 31, 2005.	5-18
Figure 5-15 Mean absolute errors of the Eta- and COAMPS-based wind speed match forecasts as functions of the forecast interval during the period June 1, 2004, to May 31, 2005.	5-18
Figure 5-16 Mean absolute errors of the Eta- and COAMPS-based power production match forecasts as functions of the Met 127 observed wind speed during the period, June 1, 2004, to May 31, 2005.....	5-19
Figure 5-17 Mean absolute errors of the Eta- and COAMPS-based wind speed match forecasts as functions of the Met 127 observed wind speed during the period June 1, 2004, to May 31, 2005..	5-19
Table A-1 <i>Potential10</i> and <i>ABLWT</i> Wind Speed Ratios (R)	A-2
Table A-1 <i>Potential10</i> and <i>ABLWT</i> Wind Speed Ratios (R) (Cont'd)	A-3
Table A-2 Differences Between <i>Potential10</i> and <i>ABLWT</i> Wind Speed Ratios (R)	A-4

LIST OF TABLES

Table 2-1 Selection of parameters available from Eta model output	2-9
Table 3-1 Constants used in original and new guidelines for different hill and terrain types.....	3-4
Table 3-2 Speed-up factors predicted by various prediction methods for Meteorological Tower 438 relative to the LLNL tower, at a height of $z = 24.4$ m above ground.....	3-7
Table 3-3 Observed ΔS and standard deviation for each stability class at Meteorological Tower 438. Wind direction between 235 deg and 245 deg, July 1, 2001, to June 30, 2003.	3-8
Table 3-4 Average ΔS observed for different wind direction inclusion criteria, such as which location was used to measure the wind direction, and how size range of directions included	3-8
Table 3-5 Measured values of ΔS at the shoulder location ($x = 0, y = L2, \theta = 0^\circ$) at different heights above ground z , for hills of different aspect ratio $A = L2/L1$	3-15
Table 3-6 Hilltop speed-up prediction accuracy comparison for each combination of speed-up prediction algorithm and wind direction interpolation method.	3-23
Table 4-1 Average Met 127/Met 225 wind speed ratio for different seasons and times of day. (Winter is Dec., Jan. and Feb., spring is Mar., Apr. and May, and so on.) Wind tunnel prediction of average wind speed ratio for neutral conditions was 0.98.....	4-8
Table 4-2.....	4-9
Table 4-3 Uncertainty levels observed for each power production prediction scheme and for all conditions, day and night conditions, and conditions corresponding to each Pasquill-Gifford stability class observed at the LLNL mast. Uncertainties expressed as mean errors (ME) and mean absolute errors (MAE) of the predictions.....	4-11
Table 4-4 Uncertainty levels observed for each power production prediction scheme for different wind directions and actual power production levels.	4-12
Table 4-5 Uncertainty levels observed for each prediction scheme considering only data with wind directions considered reliable, for all conditions, day and night conditions, and conditions corresponding to each Pasquill-Gifford stability class observed at the LLNL mast.....	4-12
Table 4-6 Uncertainty levels observed in each prediction scheme for different wind directions and actual power production levels..	4-13
Table 4-7 Mean and mean absolute errors of power production prediction schemes, excluding data points with unreliable wind directions and increasing predicted power production by a factor of 93/87 to account for unmodeled turbines.....	4-15

Table 4-8 Mean and mean absolute errors (ME and MAE) of each power production prediction scheme vs. wind direction and actual power production level, excluding observations with unreliable wind direction measurements.	4-16
Table 4-9 Number of observations at Met 127 turbine cluster, categorized by whether the predicted and actual power production levels are zero or non-zero.....	4-16
Table 4-10 Number of observations of Met 127 power production for several criteria of Met 127 recorded wind speed.....	4-17
Table 4-11 ME and MAE for power production schemes after adjusting the input wind speed by the specified amounts.....	4-19
Table 4-12 ME and MAE for recommended and four other power production prediction schemes, based on Met 127 observations between July 1, 2001 and June 30, 2003, excluding observations with missing data or unreliable Met 127 wind direction data. Units of ME and MAE are kWh/0.5h.	4-20
Table 4-13 Values of S predicted for cosine hill for: NXIN = 251, DX = 10, Horizontal Spacing Factor = 1.0, NY = 90, DY = 1, DELTA = 1.1, UREF = 10, RHO = 1.2.	4-28
Table 4-14 Values of ΔS predicted for the Met 127 0° transect. Inputs are NXIN = 35, Horizontal Spacing Factor = 1.1, NY = 90, DELTA = 1.1, UREF = 10, RHO = 1.2. Run time is the total time for iteration on a 3.2 GHz, Pentium 4 computer.	4-30
Table 4-15 Overall mean error (ME) and mean absolute error (MAE) of Met 127 power predictions, as percentages of observed wind farm capacity for four wind farm power curve methods, June 25, 2001, to June 11, 2005.	4-35
Table 4-16 Mean error (ME) and mean absolute error (MAE) of Met 127 power predictions, as percentages of observed wind farm capacity, for four different wind farm power curve methods. Includes only observations for which Met 127 wind direction data were considered acceptable between June 25, 2001 to June 11, 2005.	4-35
Table 4-17 Power curve performance for entire forecast period, December 1, 2001 to September 30, 2002.. ME and MAE values are expressed as percentage of observed wind farm capacity.....	4-37
Table 4-18 Power curve performance for December, 2001. ME and MAE values are expressed as percentages of observed wind farm capacity.	4-38
Table 4-19 Power curve performance for May 2002.....	4-38
Table 4-20 Power curve performance for July 2002.....	4-38
Table 5-1 Mean Error (ME) and Mean Absolute Error (MAE) of predictions of wind speed at case study wind farm meteorological tower (in m/s) using geostrophic drag law.....	5-6
Table 5-2 Observed accuracy of the matching method at forecasting wind speed at the case study wind farm meteorological tower anemometer and the wind farm power production. Forecasts were prepared for each of the Eta forecasts in the UC Davis archive (consisting of forecasts from 0 to 48 hours in the future, initialized at 0:00 and 12:00 GMT)	5-8
Table 5-3 ME and MAE of Eta matching forecasts using different combinations of matching Eta variables, compared with persistence forecasting.....	5-10
Table 5-4 Mean absolute error(MAE) as a percentage of observed wind farm capacity for four different forecast methods at the Altamont Pass wind farm. Skill score is percent improvement in MAE relative to persistence.....	5-12

Table 5-5 Overall performance of small and large database matching forecasts relative to persistence for six parameters.5-14

Table 5-6 Overall mean error (ME) and mean absolute error (MAE) of match forecasts of several Altamont Pass wind power and meteorological parameters between June 1, 2004, and May 31, 2005.5-17

1 INTRODUCTION

California has good potential for developing new wind generation capacity beyond the approximately 2100 MW of rated capacity in place at the end of 2005 (American Wind Energy Association, 2006). California’s Renewables Portfolio Standard, which calls for 20% renewables in the generation mix by the end of 2010, is expected to result in a large increase of the installed wind capacity in the state. Most of the current capacity is located in the five principal wind resource areas of the state (Solano, Altamont, Pacheco, Tehachapi, and San Gorgonio), shown in Figure 1-1. The new capacity is expected to be installed in these and other promising wind resource areas in Northern and Southern California.

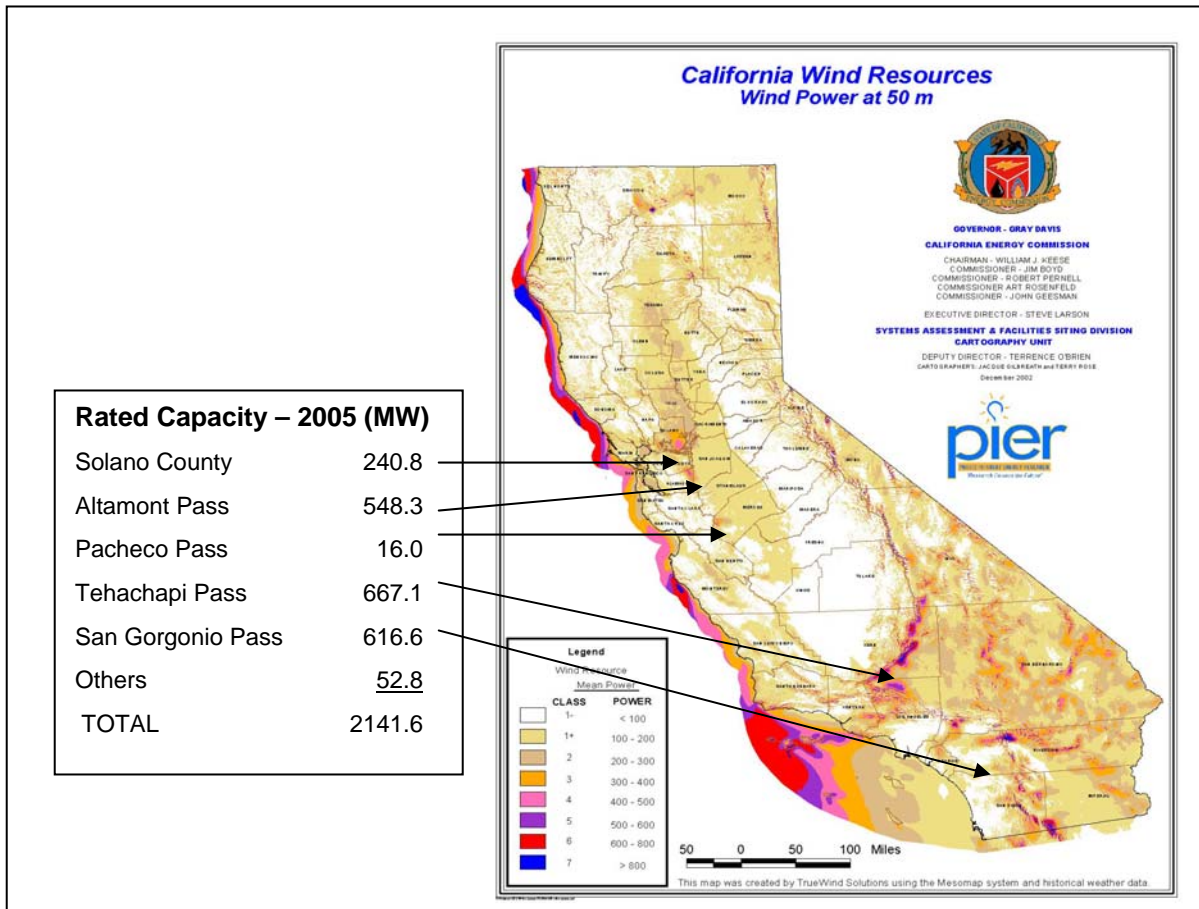


Figure 1-1 California Mean Wind Power Map at 50-m Elevation and 2005 Rated Capacity of Wind Generation at Principal Wind Resource Areas (California Energy Commission, 2006)

Wind generation is an intermittent resource and can not be dispatched or brought on-line on demand to meet an increase in load unless the wind is blowing at sufficient speed to generate the required power. Large concentrations of wind generation in one area can affect electricity grid operations, load following, and reserve requirements. System operators will need increasingly accurate wind forecast tools to manage wind and other intermittent generation resources connected to the California grid. Accurate next-hour and next-day forecasts will make it possible to optimize the response to rapid changes in wind generation to balance load and supply reserve and regulation resources.

First Energy Commission-EPRI Wind Energy Forecasting Project, 2001-2003

In 2002, the California Energy Commission (Energy Commission) and EPRI completed testing of two forecasting systems at Altamont and at San Geronio (Energy Commission and EPRI, 2003a and 2003b; EPRI 2003a). Two wind energy forecasting system developers, Risoe National Laboratory and TrueWind Solutions, applied their meteorology-based, meso-scale modeling algorithms to generate twice-daily, 48-hour forecasts of hourly wind speed and energy generation, during a 12-month period. The host wind projects were the 90-MW Wind Power Partners/Windworks project, operated by Powerworks at Altamont Pass, and the 66.6-MW Mountain View 1 and 2 wind project, operated by Seawest at San Geronio Pass. Based on the monthly and annual mean absolute errors (MAE) of the forecast vs. observed data, the Risoe and TrueWind forecasts performed better than simple persistence and climatology forecasts. However, the forecast errors were still significant, indicating that additional research is needed to incorporate improved forecast technology and forecast performance.

Current Regional Wind Energy Forecasting System Development Project, 2004-2005

In 2004, Energy Commission, EPRI, and California Independent System Operator (CA ISO) initiated a new 18-month project to build on the first project and develop and test improved wind energy forecast algorithms for both short-term forecasts (regional five-minute forecasts over three hours) and intermediate-term forecasts (hourly wind plant forecasts over 48 hours) in the principal wind resource areas of the state. The project was completed during 2005, and the results are presented in the four-volume report, *California Regional Wind Energy Forecasting System Development and Testing* (Energy Commission and EPRI, 2006a, 2006b, 2006c, and 2006d).

This volume of the final report, *California Regional Wind Energy Forecasting System Development – Volume 3: Wind Tunnel Modeling of Wind Flow over Complex Terrain*, describes the detailed investigation of using wind tunnel data, empirical models, and numerical weather forecasts to generate wind energy forecasts. The other report volumes include *Volume 1: Executive Summary*; *Volume 2: Wind Energy Forecasting System Development and Testing and Numerical Modeling of Wind Flow over Complex Terrain*; and *Volume 4: California Wind Generation Research Dataset (CARD)* (Energy Commission and EPRI, 2006a, 2006b, and 2006d).

Objectives and Scope

The primary objective was to develop and evaluate the performance of a wind farm power method incorporating wind tunnel data. During this study, the initial work and methods of Cheng (2002), as reported in the EPRI reports on the previous project, (Energy Commission and EPRI, 2003a and 2003b), were revised and improved, incorporating additional refinements such as including wind direction and air density dependence in the database of wind tunnel measurements and in the power prediction algorithm. Additionally, several other plant power curves were developed for comparison purposes.

Another objective was to develop and test an alternate wind farm power curve method based on “empirical” algorithms. This was done to allow the development of a plant power curve at sites for which performing a full set of wind tunnel tests is not feasible. A wind tunnel investigation of flow over generalized terrain was performed to inform the development of this method. The initial method of developing this power curve was to apply the “speed-up” prediction methods used in wind engineering. Ultimately, it was found that these methods would not likely provide sufficient accuracy for wind power forecasting application. An alternative method was developed based on using two-dimensional potential flow simulations of the terrain near the wind farm. When compared to the wind tunnel power curve, the power curve based on the potential simulation method was almost as accurate.

Another objective was to develop a next-day automated wind power forecasting system that could operate on a desktop computer, without requiring computationally intensive numerical methods. It was realized that it would be difficult to achieve forecasting accuracy better than the commercial forecasters that have significant resources at their disposal. Therefore, the goal of this system was to be able to test various methods of performing each step in the forecasting process leading to the final predictions.

Report Organization

The report consists of seven chapters, including Chapter 1, Introduction.

Chapter 2, Atmospheric Boundary Layer Wind Tunnel Application to Wind Energy Forecasting, describes the application of the wind tunnel modeling data collected in the wind tunnel to a wind energy forecasting system.

Chapter 3, Wind Speed-Up Over Hills, describes wind tunnel and empirical modeling of wind flow over idealized hill shapes.

Chapter 4, The Wind Farm Power Curve, describes development of a wind plant power curve using wind tunnel measurements and other methods.

Chapter 5, Downscaling and Forecasting, describes development of a desktop PC wind energy forecasting system based on download of Eta model wind forecasts, downscaling the forecasts to the wind plant met tower location, and matching conditions to historical conditions to develop a forecast.

Introduction

Chapter 6, Summary, summarizes the results and key findings of the project.

Chapter 7 presents the references.

2

ATMOSPHERIC BOUNDARY LAYER WIND TUNNEL APPLICATION TO WIND ENERGY FORECASTING

Figure 2-1 shows a schematic of the wind power forecasting system implemented at UC Davis during this project. The system operates on a desktop PC. Eta and COAMPS regional scale model outputs are automatically downloaded as they become available. Archived model output data also can be used. Using the downloaded model output, one of several methods is selected to forecast the wind speed and direction at the wind farm meteorological tower. The forecast performance can be checked by comparing the forecast and actual wind speed and direction data from the wind farm meteorological tower data provided by the wind farm operator. Next, the wind speed and direction at the meteorological tower are used to predict the wind speed and power production of the wind farm. The power production forecast performance can be checked by comparing the forecast and actual wind farm power production data. The accuracy of the power production model alone can be determined by replacing the forecast wind speed and direction with the actual wind speed and direction recorded at the meteorological tower as inputs and comparing the resulting forecast and actual recorded power production.

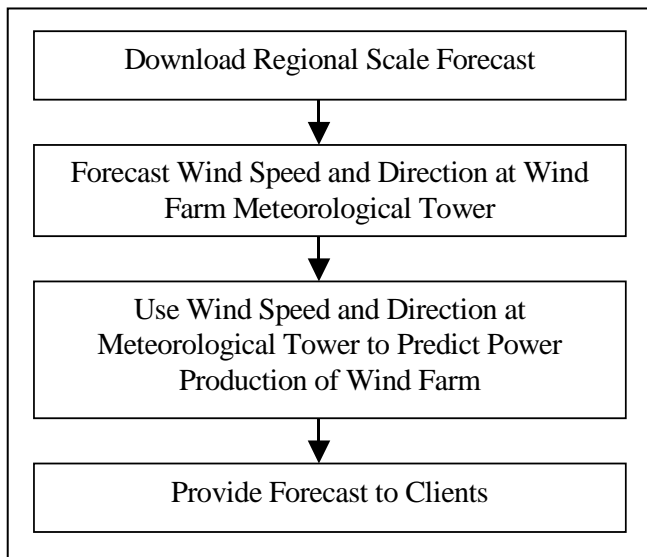


Figure 2-1 Schematic of UC Davis wind power forecasting system. UC Davis Atmospheric Boundary Layer Wind Tunnel

Atmospheric boundary layer wind tunnels (ABLWTs) have been used to simulate near-surface winds for over 40 years and have been shown to be capable of predicting wind fields in complex

terrain, dispersion of airborne pollutants, and wind-induced pressure distributions on buildings (Cermak, 2003).

The UC Davis ABLWT is designed for simulating neutral atmospheric boundary layer flows past surface objects. It is an open-return type tunnel, as seen in Figure 2-2, composed of five sections: an entrance section, a flow development section, a test section, a diffuser section, and a 56-kW(75 hp) DC motor and fan. A bell-shaped entrance section provides a small contraction area ratio. An air filter, to screen out airborne particles and reduce the large-scale pressure fluctuations, is followed immediately by a honeycomb flow straightener and a series of spires to "pre-form" the boundary layer.

A 12-m (39-ft)-long flow development section is used to generate a mature boundary layer at the test section. An adjustable ceiling and diverging walls in the development section maintain a zero-pressure-gradient flow throughout the tunnel. Roughness elements, placed on the floor of this section, generate the proper boundary-layer height in the test section. The test section is 3.7 m (12 ft) long, 1.7 m (5.5 ft) high and 1.2 m (4 ft) wide. Plexiglas[®] windows on each side allow observation, and a sealing sliding door provides access. The tunnel ceiling height increases in the downwind direction to maintain a horizontal pressure gradient of zero. Measurements are made using a three-dimensional traversing probe system that is mounted to the ceiling of the test section. This system allows for precise placement of a sensor at any point within the test section. Small 1-milliwatt (mW) lasers were mounted on the traverser to sight vertical height and horizontal position to within 1 mm.

Mean velocity and turbulence intensity were measured using a TSI Inc. single wire, end-flow hot-wire probe, Model 1210-20. A 90° angle adapter, TSI Model 1152, was used to provide access to upstream points when attached to an end-flow probe. The right angle bend was used to limit the undesirable flow interactions of the model with the probe support by orienting the hot wire directly upwind of its support. A TSI single sensor, plug-in, Model 1150, 50-cm probe provided support and electrical connection with the signal conditioner. A three-dimensional traversing probe system is mounted to the ceiling of the test section (Figure 1-2, Section B-B). This system allows for precise placement of a sensor at any point within the test section. Small 1-mW lasers are mounted on the traverser to sight vertical height and horizontal position to within ±0.5 mm.

A 10-m shielded tri-axial cable connects the hot wire to a two-channel constant temperature thermal-anemometry unit with a signal conditioner, TSI model IFA 100. The analog signal from the signal conditioner is passed to a 12-bit analog-to-digital (A/D) converter (United Electronics Industry Win 30 DS) and then to a Pentium 166 computer for analysis and data storage by a National Instruments LabView program. The A/D conversion process causes no loss in accuracy of the measurement data. LabView was used to sample the hot-wire signal at a rate of 1000 Hz in all of the work documented here.

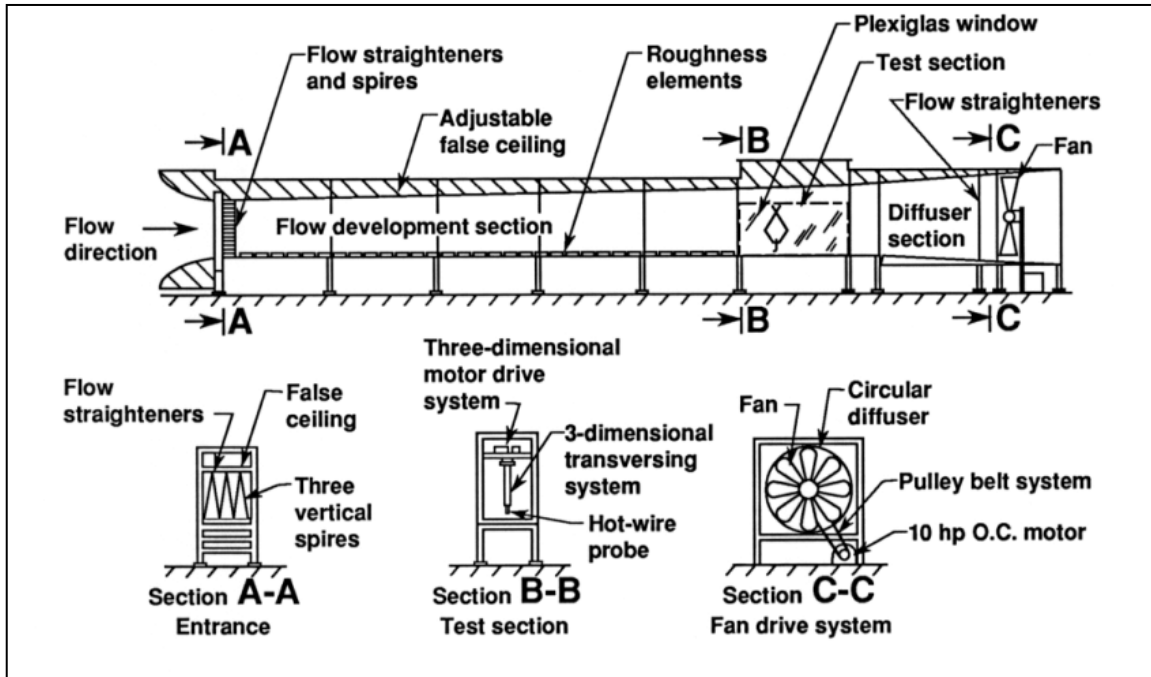


Figure 2-2 Schematic of UC Davis Atmospheric Boundary Layer Wind Tunnel.

Before testing begins, each hot-wire anemometer is calibrated against a pitot-static tube connected to a precision manometer. The output voltage of the hot wire and the wind speed at the pitot-static tube are recorded over the expected range of wind speeds. A third-order polynomial curve is fit to the data to generate the calibration curve. The hot-wire voltage is logged for a minimum of 30 seconds at each point being measured. Post-processing of the signal data is performed by custom written software that uses the calibration curve and logged hot-wire readings to calculate mean wind speed, RMS wind speed, and turbulence intensity. Thermal anemometry has been widely used in measuring turbulent characteristics for its ease in handling fast fluctuations in turbulence. Typically, hot-wire measurements made close to the surface have an uncertainty of less than $\pm 5\%$ of the true values.

Simulation of the Atmospheric Boundary Layer

The boundary layer within the wind tunnel simulates the same turbulent characteristics found in the full-scale atmospheric boundary-layer. It is important that the atmospheric boundary-layer approaching the modeled region have the same characteristics as it does in full-scale. Otherwise, the changes in local velocity over the model will not be accurately simulated. The region upwind of the modeled terrain is a flat region of the Livermore Valley, so it was not necessary to build a specific model of this upwind region.

The relationship between the mean velocity U and height above the surface z , for a boundary-layer of height δ and a mean velocity at height δ of U_∞ , is described by the power law:

$$\frac{U}{U_{\infty}} = \left(\frac{z}{\delta} \right)^{\alpha} \quad (2.1)$$

The wind tunnel power-law exponent α must closely match the full-scale value of α . Using the empirical power law estimation methods, from Counihan (1975) and a full-scale surface roughness, z_0 estimated at 15.6 cm, from a wind study done by Chapman and Gouveia (1987), α was estimated to be 0.17 for the approach to Altamont Pass. However, using the empirical method from Jensen (1958), and a geostrophic wind speed, U_{∞} of 30 mph and δ of 457 m (1160 ft), from meteorological data used in the study, α was estimated to be 0.20.

Given this range of the power-law exponent α , this full-scale condition was achieved in the UC Davis ABLWT by systematically arranging a pattern of 3.5" x 5.75" x 0.75" (thin blocks) and 3.25" x 7.75" x 1.5" (thick blocks) wooden blocks over the entire flow-development section of the wind tunnel. The block pattern roughly consisted of half of each type of block configured in alternating sets of four and five blocks per row. The simulated power-law exponent α is equal to 0.19.

In addition, the approaching mean velocity profile should also agree with the logarithmic, or "law-of-the-wall," wind profile, within the lower region of the boundary layer:

$$\frac{U}{U_{\infty}} = \frac{1}{\kappa} \ln \left(\frac{z}{z_0} \right) \quad (2.2)$$

where κ is von Karman constant. The surface layer, the lower 10 to 15% of the boundary layer, is governed by Eqn. 1.2. For proper wind tunnel modeling, the model must be geometrically scaled to remain within this bound. From previous data, the simulated atmospheric boundary height of the ABLWT is about 0.7 m, although this will vary over the complex terrain model.

Boundary-layer similitude also requires surface matching of roughness Reynolds numbers and Re_z independence, in which Re_z is greater than 2.5 as described by Schlichting (1979). The roughness Reynolds number ($Re_z = u_* z_0 / \nu$), is about 14 when the wind tunnel free-stream velocity $U_{\infty} = 3.1$ m/s, friction velocity, $u_* = 0.22$ m/s, and the roughness height $z_0 = 0.00095$ m. Therefore, with Re_z well above 2.5, the simulated atmospheric flow is aerodynamically "rough," similar to conditions seen in full-scale conditions.

Altamont Pass

A portion of the Altamont Pass wind resource area, near Livermore, California, was used as the case study for several of the experiments in this research project. The site is located about 50 km east of San Francisco (Figure 2-3), where wind conditions can be influenced by diurnal sea breezes, and a series of rolling hills that separate the San Francisco Bay Area from the San Joaquin Valley. Although no longer the largest wind energy producer, the Altamont Pass still contains one of the world's largest concentrations of wind turbines.

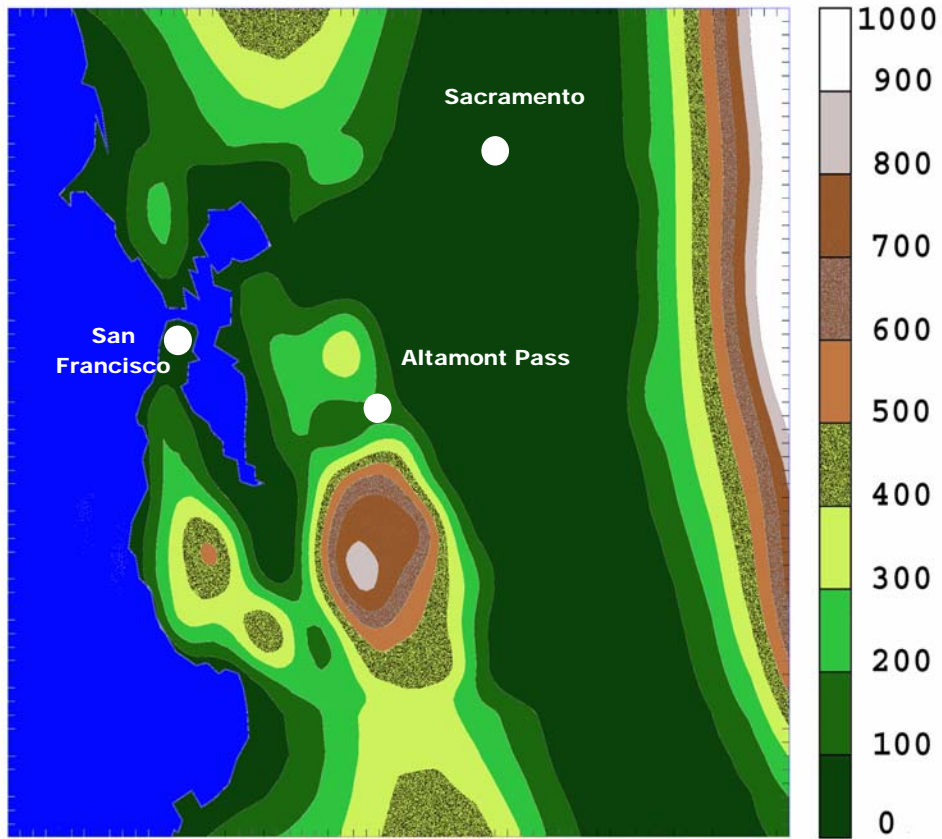


Figure 2-3 Location of Altamont Pass, California.

The case study wind farm consists of 900 Kennetech 56-100 wind turbines owned by Powerworks. The turbines are arrayed along ridgelines in the Pass. For reporting purposes, the turbines are divided into 10 clusters, each of which has an associated meteorological tower. For example, the cluster associated with meteorological tower 127 (“Met 127”) consists of 93 turbines.

The winds in the Altamont Pass area are strongest during the summer and lowest during the winter. For a site approximately 1 km east of the Met 127 site tested in this study, Davis and Nierenberg (1980) observed a monthly average wind speed of 10.3 mph during July 1979, versus 7.3 m/sec for December 1979. The level of seasonal variation was similar for several other sites they observed within the Altamont Pass region. Winds tend to blow from the southwest in the summer, while direction is more variable in the winter (see Figure 2-4).

Winds also can vary significantly over relatively short distances due to the effects of complex terrain. Holets (1985) compared observations from eight hilltop sites in the Altamont Pass area and found significant variation between sites. For 11 summer days in 1981, Holets observed average wind speed differences between the sites of 3.7 m/sec to 4.6 m/sec. Brown and Watt (1988) observed a mean annual wind speed ratio of 0.83 comparing a reference site to a nearby anemometer mast.

It has been observed that stable conditions often result in high near-surface wind speeds in the lowest 100 m above ground (Nierenberg, 1989). McCarthy (1987) observed that a deep marine inversion layer, relative to the height of the pass, often resulted in good (eastern) lee slope flow, while a shallow inversion layer resulted in separation zones on the lee (eastern) slope, and "spotty" flow in general. McCarthy observed that stably stratified flow is an important factor in producing high winds on the lee (eastern) slope of the pass.

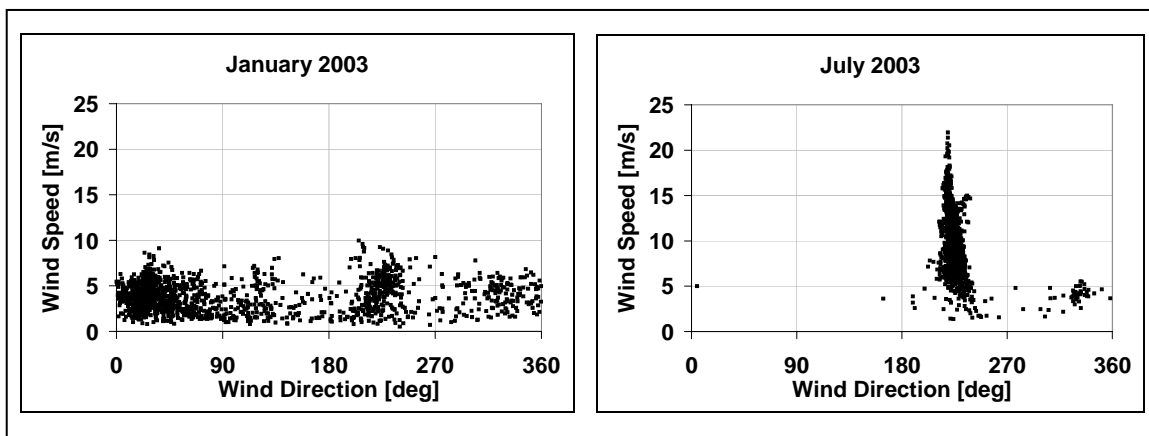


Figure 2-4 Wind speed vs. direction at Altamont Pass Met 127 meteorological tower during January 2003 (left), showing typical winter winds, and June 2003 (right), showing typical summer winds.

It should be noted that while there is great confidence in the power production figures provided by Powerworks (since this is also metered by the utilities purchasing the power, and is also required by the state of California in order to receive tax credits associated with wind energy production), the meteorological data appears to be of lower quality. In addition to the Met 438 barometer being inoperable, a qualitative analysis of the remained constant over long time periods, suggesting a "stuck" wind vane.

One year out of 2.5 years of data for Met 127 were deemed to contain unreliable wind direction data. The following time periods between June 25, 2001 and June 11, 2005 have unreliable wind direction data: June 25 to Aug. 17, 2001, Sept 27 and 28, 2001, April 12 to July 1, 2002, March 2 to March 27, 2003, April 9 to May 31, 2003, Aug. 21, 2003 to May 24, 2004, and October 11, 2004, to June 11, 2005.

Eta Regional Scale Forecast

The primary regional scale forecast (RSF) used in this study was the NOAA Eta 40 km model. On January 25, 2005, the Eta model was renamed the North American Mesoscale, or "NAM" model. For consistency, the term "Eta" refers to the Eta/NAM model.

The Eta model is a regional-scale, non-hydrostatic operational weather forecasting system. It is maintained by the United States National Weather Service (NWS). The model is run twice a day, at 00:00 and 12:00 GMT, and produces forecasts at three-hour intervals from zero hours ahead (the so called "initialization run" since this is essentially the observed data interpolated over the domain) to 84 hours ahead. Immediately after a forecast is completed, it is made available on several FTP servers for downloading by the public.

The Eta model provides predictions of weather conditions on a 40-km square grid overlaid across the continental United States and surrounding regions. The grid itself is based on a Lambert conformal projection centered on the central United States. Grid points and, therefore, vector components are generally *not* aligned exactly along true north-south or east-west. Figure 2-5 shows the locations of the model grid points in the Altamont Pass area.

At each grid point, a large number of predicted parameters are available. Table 2-1 summarizes the most important parameters in this study. The Eta model forecasts many parameters in addition to those in the table. There are multiple vertical levels above each grid point, each level denoted by the air pressure in millibars. For most atmospheric observations, there are 39 main levels, ranging from the highest at 50 mb to the lowest at 1000 mb. Additional parameters are reported that are either level insensitive or may occur at different pressure heights. These parameters are associated with additional levels that include the surface, and various elevations above ground for variables that are critical near the surface. For example, Eta predicts wind speeds 10 m above ground using data from the two lowest regular levels. This information is provided for diagnostic purposes only (Black, 2003), since it can not be representative of any specific location at such a low grid resolution.

All time references in the Eta model are at Greenwich Mean Time (GMT), effectively the time observed in the time zone of London, England. To convert GMT to Pacific Standard Time, it is

necessary to subtract six or seven hours from the time expressed in GMT, depending on whether Daylight Saving Time is being observed. Note that many meteorological records, even if expressed in the local time zone, do not observe Daylight Saving Time, because it results in a one-hour discontinuity in the records when it starts or ends.

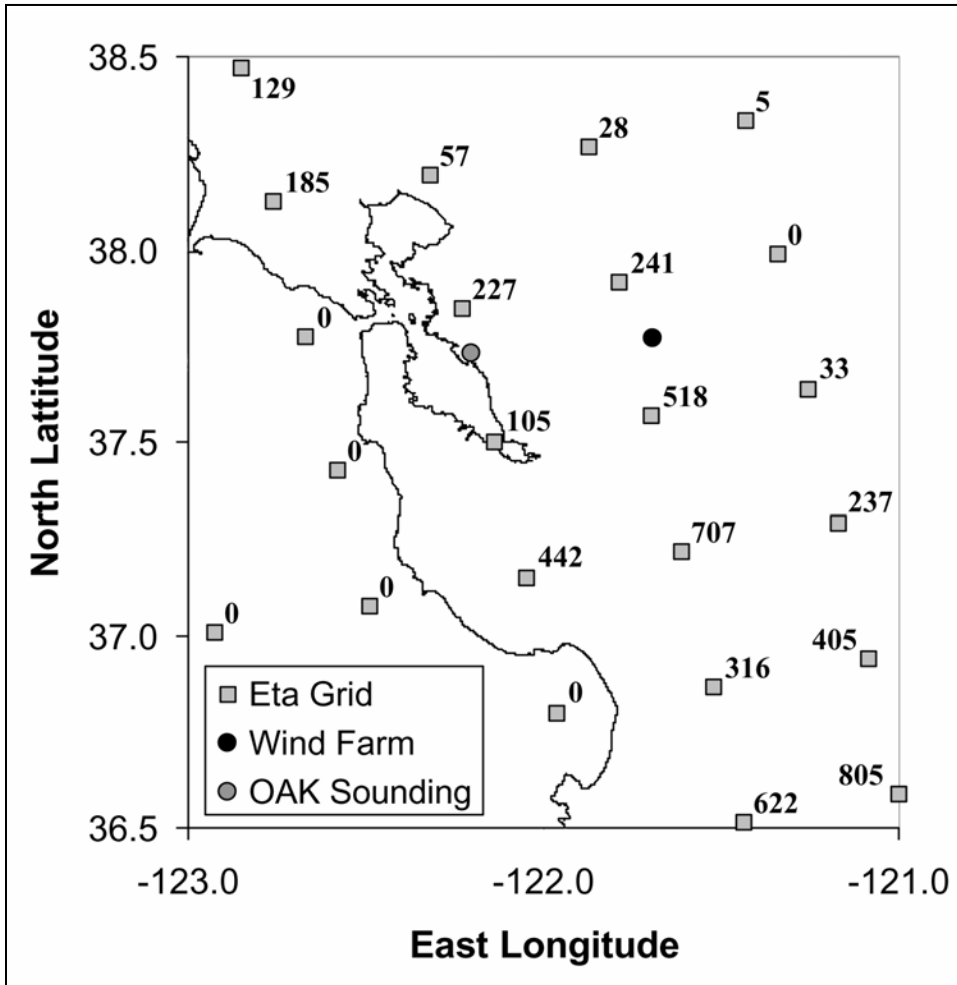


Figure 2-5 Locations of Eta model grid points in the vicinity of the Altamont Pass wind farm. Numbers adjacent to the points indicate the Eta-modeled terrain height in meters. The location of the Oakland radiosonde launch site is also indicated.

Table 2-1 Selection of parameters available from Eta model output.

Observation	Symbol	Units
Sea-level pressure	MSLET:MSL	Pascals
Sea-level pressure again	PRMSL:MSL	Pascals
U comp. of wind speed at 10 m above ground	UGRD:10 m above gnd	m/sec
V comp. of wind speed at 10 m above ground	VGRD:10 m above gnd	m/sec
Height of level above sea level	HGT:nnnn mb*	Meters
U comp. of wind speed	UGRD:nnnn mb*	m/sec
V comp. of wind speed	VGRD:nnnn mb*	m/sec
W comp. of wind speed	VVEL:nnnn mb*	m/sec
Air temperature	TMP:nnnn mb*	Kelvin
Relative Humidity	RH:nnnn mb*	Percent

* nnnn is replaced by the pressure height of the reading. For all readings indicated with (*), available pressures range from 25 to 1000 mb in steps of 25 mb. The physical (as opposed to pressure) height above sea level of a reading can be determined by looking at the "HGT: nnnn mb" record for pressure.

3

WIND SPEED-UP OVER HILLS

Wind-tunnel and computer simulations have been shown to accurately predict flow in complex terrain (Bowen, 2003); however, often only a few representative wind directions and locations in the flow field are measured. In many cases, it is not feasible to conduct wind-tunnel or numerical simulation studies of a site, but is still necessary to estimate local topography and atmospheric stability effects on the flow field.

A tool that could reasonably predict the results of an ABLWT investigation without requiring a wind tunnel test or significant computational resources would have many applications, including rapid wind resource assessment and the development of wind plant-scale power curves for use in forecasting applications. Review of the available methods for predicting the results of an ABLWT simulation without resorting to a full computational fluid dynamics solution indicate they are limited to those that applying empirical formulae to extreme simplifications of the problem, for example calculate the wind speed at the peak of a hill of ideal shape and oriented a right angle to the wind direction (for example Weng et al., 2000). Postulating that it might be possible to extend the applicability of these existing methods to address situations such as non-perpendicular wind directions and more complex three-dimensional hill shapes, further investigation indicated that only limited data are available to address these cases, and that general data such as the impacts of variable wind direction were not available in the literature. Therefore, experiments were designed to investigate the impact of varying wind direction relative to the hill orientation.

Speed-Up Prediction Background

Much work has been done developing simplified models for predicting wind "speed-up" in complex terrain. Speed-up is the increase of near-surface winds above a hill as compared to the wind over a flat surface at the same height above the surface. It is expressed in dimensionless units as the fractional speed-up ratio:

$$\Delta S = \frac{U(z) - U_o(z)}{U_o(z)} \quad (3.1)$$

where U is the wind speed at height z above the hill, and U_o is the upstream speed of the hill at the same height. It is assumed that the approach to the hill is a flat surface with the same surface roughness as the hill.

Jackson and Hunt (1975) developed an analytical method to predict speed-up over a two-dimensional, smooth hill without flow separation, which was subsequently improved (Hunt et al. 1988). They approached the problem by dividing the region above the hill into several layers. An outer layer was defined where the flow is far enough removed from the surface that it can be modeled as potential flow. A middle layer is located below the outer layer where the flow is not affected by friction with the surface but is close enough to the hill that it can not be considered irrotational flow. The inner layer is adjacent to the surface, and the flow is dominated by surface friction. Other researchers have made minor extensions of the Jackson and Hunt methods. For example, Mason and Sykes extended the method of Jackson and Hunt (1975) to a single three-dimensional axisymmetric hill. The body of work based on Jackson and Hunt remains essentially the only satisfactory analytical method of estimating speed-up over hills.

Kaimal and Finnigan (1994) extended the results of Jackson and Hunt (1975) to formulate a set of widely used simple guidelines to estimate the maximum speed-up ΔS_{\max} expected over simple topographic features with slopes low enough to not experience separation (i.e., geometric divergence angles of less than 15° to 18° relative to the mean flow direction):

$$\Delta S_{\max} \approx 1.6h / L_1 \quad \text{for axisymmetric hills} \quad (3.2a)$$

$$\Delta S_{\max} \approx 2.0h / L_1 \quad \text{for 2D ridges} \quad (3.2b)$$

Here L_1 is the horizontal distance from the hill peak of height h to the point on the slope at height $h/2$ (the "half-height" of the hill). This set of equations is generally considered to usually be accurate to $\pm 15\%$.

Numerous experimental studies investigated speed-up over two-dimensional hills. Gong and Ibbetson (1989) performed wind tunnel tests on a two-dimensional ridge and a circular hill, both with cosine squared cross-sections. Miller and Davenport (1998) conducted wind tunnel tests of two-dimensional model hills and presented tables of speed-up values for different approach slopes and upwind conditions. Weng et al. (2000) also present guidelines for two-dimensional hills, based on hill geometry and surface roughness and also report the results of several wind tunnel tests. Taylor (1998) conducted numerical simulations of flow over low- and moderate-slope hills and presented an equation to predict speed-up based on hill parameters. Kim et al. (1997) experimentally and numerically investigated the effects of hill slope on speed-up over two-dimensional sine wave hills. Finite volume numerical simulations were conducted for flow over four actual hills for which field data were available (Kim et al., 2000).

The surface roughness of the surrounding terrain affects speed-up over a hill (Weng et al. [2000], Miller and Davenport [1998]), especially as the ratio of surface roughness to hill length scales decreases. In numerical and field studies of actual hills, Kim et al. (2000) observed that the flow field over a hill is affected by the presence of other hills nearby, and that these hills must be included for accurate results. Lange and Hojstrup (2001) evaluated the accuracy of predictions made by the WASP[®] program for the power output of proposed offshore wind turbines (which are in very simple terrain) and found that, while predictions were good overall, observed errors in the prediction correlated with the presence of land at distances of about 10 km from the sites.

Further complicating matters, flow separation occurs in the lee of steep hills. Finnigan (1988) compiled separation data from multiple field and wind tunnel studies. Separation did not occur when maximum slopes were less than 0.27 (15°), always occurred when maximum slope was at least 0.32 (18°), and was intermittent when slopes were between these values. For two-dimensional, sinusoidal hills, Kim et al (1997) and Miller and Davenport (1998) both used the criterion that separation occurred for hills with slopes exceeding 0.4 (22°). Once separation occurs, accurate speed-up predictions became significantly more difficult. A number of studies addressed flow over actual three-dimensional terrain. Perhaps, the most significant such study was conducted at Askervein Hill, Scotland (Taylor and Teunissen, 1987).

There have been several empirical speed-up prediction algorithms published that provide formulae or look-up tables to predict speed-up for arbitrary hills. The ESDU (1990) wind speed prediction algorithm incorporates a correction factor for sites on or near two-dimensional escarpments that was derived from wind tunnel data and field work of Bowen and Lindley (1977) and the numerical studies of Deaves (1980). The correction factor (called K_L) is presented in a series of lookup graphs for different escarpment slopes.

Taylor and Lee (1984) present a simple speed-up prediction algorithm (the “original Guidelines”) that allowed the prediction of ΔS above a hilltop at various heights above ground z . Speed-up can be predicted over a hill that is either isolated or located among regularly repeating hills, as would occur in rolling terrain. The original Guidelines predict a maximum speed-up ΔS_{\max} based on hill height h and the hill half-length L_1 . It is then assumed that ΔS varies exponentially with height z :

$$\Delta S_{\max} = Bh / L_1 \quad (3.3a)$$

$$\Delta S = \Delta S_{\max} \exp(-Az / L_1) \quad (3.3b)$$

where A and B are constants given in Table 3-1, that depend on the type of hill and surrounding terrain. The original Guidelines can be applied in cases of moderate to high wind speeds on hills with maximum slopes <0.3 , $L_1/z_o > 100$ and $L_1 < 2$ km.

Weng et al. (2000) refined the original Guidelines using a series of numerical simulations, including some non-linear, and based on the results proposed a set of “new Guidelines.” The new Guidelines allow for the variation of surface roughness z_o , and the prediction of speed-up at the tops of steeper hills, with slopes up to about 0.5. The non-linear equations in the new Guidelines are:

$$\Delta S_{\max} = \frac{h}{L_1} \left(B_1 + B_2 \ln \left(\frac{L_1}{z_o} \right) \right) \left(1 + B_3 \frac{h}{L_1} + B_4 \left(\frac{h}{L_1} \right)^2 \right) \quad (3.4a)$$

$$A_3 = A_{31} + A_{32} \ln(L_1/z_o) \quad (3.4b)$$

$$\ln \frac{\Delta S(z)}{\Delta S_{\max}} = A_1 + A_2 \frac{z}{L_1} - A_3 \exp(-A_3 z/L_1) \quad (2.4c)$$

where the constants A_i and B_i , given in Table 2-1, depend on the hill and surrounding terrain types.

Table 3-1 Constants used in original and new guidelines for different hill and terrain types.

Topography	Original		New							
	A	B	A_1	A_2	A_{31}	A_{32}	B_1	B_2	B_3	B_4
Isolated 2D hill	3.0	2.0	-0.63	-1.36	-0.55	0.69	2.40	-0.051	0.029	-0.51
Isolated 3D hill	4.0	1.6	-0.64	-1.49	-0.34	0.64	2.05	-0.048	0.24	-0.40
2D rolling terrain	3.5	1.55	-0.60	-1.64	-2.03	0.90	2.20	-0.049	-0.64	-0.19
3D rolling terrain	4.4	1.1	-0.63	-1.92	-1.67	0.64	1.58	-0.036	0.069	-0.85
2D escarpment	2.5	0.8								

There have been only minimal laboratory investigations of speed-up over non-symmetric three-dimensional hills that have different horizontal lengths and widths (i.e., aspect ratios not equal to one) in addition to different heights. Lemelin, Surry and Davenport (1988), hereafter referred to as LSD, used a series of numerical simulations with the MS3DJH/3R model to derive a set of speedup prediction formulae to predict speedup anywhere above an elliptic paraboloid hill defined by three length scales: in the direction of the approach wind L_1 , perpendicular to the approach wind L_2 , and peak height h .

$$A = L_2/L_1 \quad \phi = h_p/L_p \quad (3.5a)$$

$$\Delta S = C_1 \phi \left(\frac{A}{A+C_2} \right) \left(\frac{1}{1+3(x/2L_p)^2} \right)^2 \left(\frac{1}{1+C_3(z/L_p)} \right)^2 \quad \phi \leq 0.4 \quad (3.5b)$$

$$\Delta S = 0.4C_1 \left(\frac{A}{A+C_2} \right) \left(\frac{1}{1+3(x/5h_p)^2} \right)^2 \left(\frac{1}{1+C_3(z/2.5h_p)} \right)^2 \quad \phi > 0.4 \quad (3.5c)$$

where h_p and L_p are the local height of the hill and the local primary hill half-length at the point of interest. The values of the constants are $C_1 = 2.3$, $C_2 = 0.4$ and $C_3 = 2.0$. At the hill top, $h_p = h$ and $L_p = L_1$. Then the equations become

$$\Delta S = C_1 \left(\frac{h}{L_1} \right) \left(\frac{A}{A+C_2} \right) \left(\frac{1}{1+C_3(z/L_1)} \right)^2 \quad \phi \leq 0.4 \quad (3.6a)$$

$$\Delta S = 0.4C_1 \left(\frac{A}{A + C_2} \right) \left(\frac{1}{1 + C_3(z/2.5h)} \right)^2 \quad \phi > 0.4 \quad (3.6b)$$

This model was derived for low to moderate slopes (simulations were done at $h/L = 0.28$) and $150 \leq L_1/z_0 \leq 100,000$. While the LSD formulation appears to be unique in that it includes the hill aspect ratio, the equations do not predict the negative speed-up values that occur at the base of very steep hills, and like most methods, it only considers winds at right angles to the hill.

No comprehensive results could be found that determine speed-up as a function of the approach direction of the wind. Also, most non-field studies investigated either two-dimensional, semi-infinite hills with the approaching wind direction perpendicular to the long axis of the model, or three-dimensional axisymmetric circular hills for which the flow is not direction dependent.

If these studies address wind direction at all, most empirical speed-up prediction methods use simple correction factors to account for the wind direction. Baker (1985) conducted model and full-scale tests of 27° (0.51) slope railroad embankments and found the speed-up algorithm outlined by ESDU (1990) worked well when the flow was perpendicular to the embankment. Baker noted that for non-orthogonal winds, only the velocity component normal to the embankment is accelerated and derived the following equation to modify the ESDU “ K_L ” factor ($K_L = 1 + \Delta S$) to include wind direction, where the speed-up factor is:

$$\Delta S(\theta) = \left((1 + \Delta S_o)^2 \cos^2 \theta + \sin^2 \theta \right)^{1/2} - 1 \quad (3.7)$$

and θ is the angle of the wind direction off perpendicular and $\Delta S_o = \Delta S(\theta = 0^\circ)$ is the ΔS that would be estimated with a wind direction perpendicular to the embankment.

An FAA (1988) model of speed-up for a two-dimensional ridge, given in a document on the siting of wind shear detectors near airport runways, is similar to the original Guidelines, except that the model adds a wind direction correction in which the horizontal length scale of the ridge is measured across the ridge in the same direction as the wind is blowing. The half-length of the hill is the length in the direction of the approach wind, calculated using the relation $L_o = L_1/\cos \theta$. L_1 and L_o are the half-lengths of the hill in the directions perpendicular to the ridgeline and aligned with the wind, respectively. θ is the angle of the approach wind direction relative to the direction normal to the ridgeline. (i.e. $\theta = 0^\circ$ is a wind normal to the ridge, $\theta = 90^\circ$ is a wind parallel to the ridgeline.)

Speed-Up At Altamont Pass

The speed-up prediction schemes outlined above exhibit a wide variability of accuracy when used to predict the speed-up over actual hills. Weng et al. (2000) compare their Guidelines, as well as those of Taylor and Lee (1984) with field measurements from several sites. The accuracy of both methods depended most strongly on the site characteristics. For example, the Askervein Hill predictions agreed well with actual measurements, while predictions for Nyland Hill

significantly underestimated ΔS at all heights. Geographic sensitivity is significant for all of the prediction schemes outlined above.

It was desired to assess the degree of accuracy that might be achieved at the Altamont Pass case study site, especially since most of the field data used to evaluate the prediction schemes are from single hills surrounded by relatively flat terrain. Fortunately, field data were found that could be applied directly to the unmodified prediction schemes. As shown in Figure 3-1, the Powerworks meteorological tower 438 (“Met 438”) is situated on the crest of a ridgeline that is oriented approximately perpendicular to the prevailing summer wind direction of 240° . The fully-instrumented LLNL meteorological tower is situated on a bearing of 240° from Met 438, about 4.5 km away in flat terrain, providing reference conditions for speed-up factor calculations.

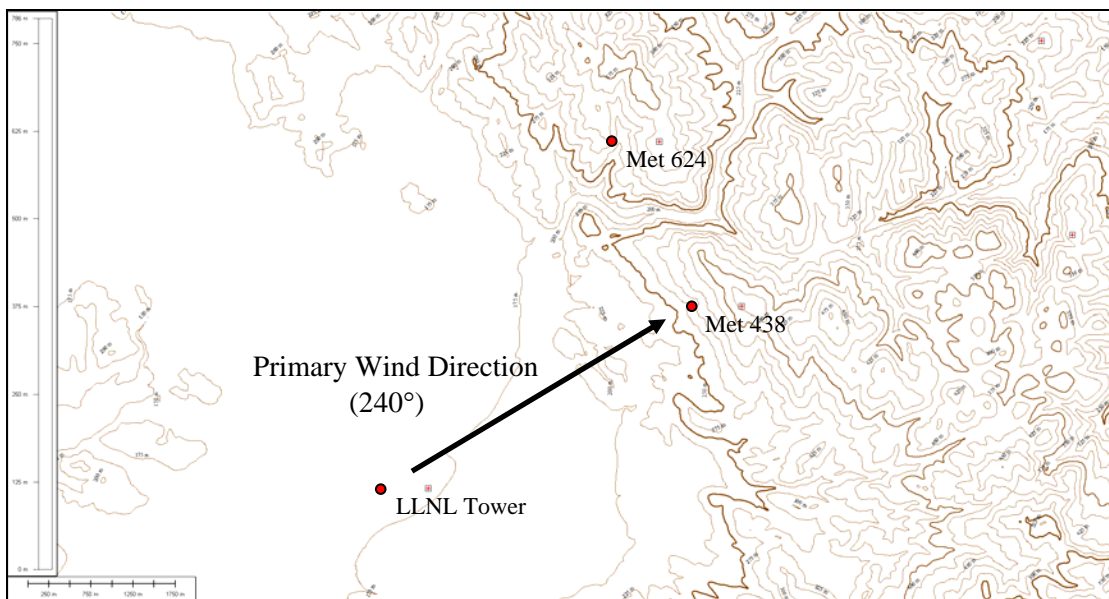


Figure 3-1 Map of western side of Altamont Pass showing location of LLNL meteorological tower and Powerworks meteorological towers 438 and 624. North is up.

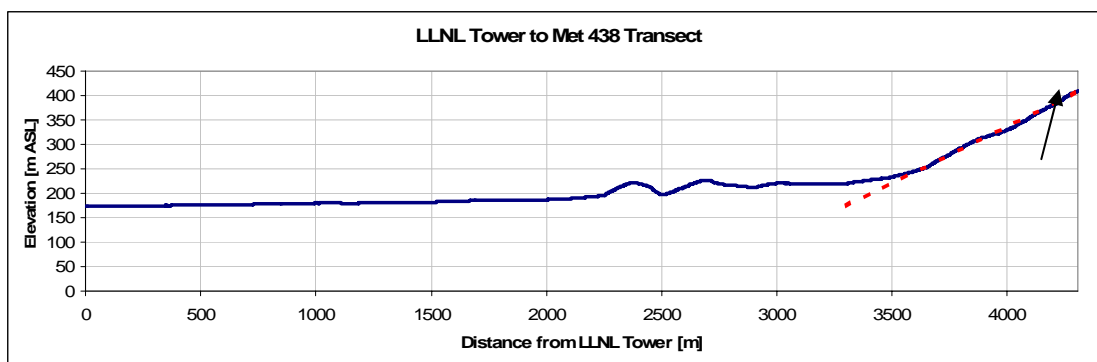


Figure 3-2 Elevation transect from LLNL meteorological tower to Met 438. Dotted line shows hill slope approximation used for prediction schemes.

As shown in Figure 3-2, the terrain between the LLNL tower and Meteorological Tower 438 consists of mostly flat plain, followed by a steep uniform rise to the ridge crest location of Meteorological Tower 438. The prediction scheme parameters can be directly estimated. The hill type is assumed to be a two-dimensional ridge with $h = 235$ m and $L = 503$ m. The land use is open grassland with $z_0 = 15$ mm. Using these parameters, the prediction schemes were used to predict the speed-up at $z = 24.4$ m (the height of the Met 438 anemometer). Table 3-2 shows the predicted speed-up factors, which range between 0.62 and 0.935. This range of variation is typical for these methods.

Table 3-2 Speed-up factors predicted by various prediction methods for Meteorological Tower 438 relative to the LLNL tower, at a height of $z = 24.4$ m above ground.

Prediction Method	ΔS at Anemometer Height
Equation 2.2b	0.935
FAA	0.808
Lemelin, Surry and Davenport	0.784
Taylor and Lee	0.808
Weng et al. (Linear)	0.691
Weng et al. (Non-Linear)	0.620

Calculation of the measured speed-up factor at a given time was complicated by the differing observation heights at the LLNL tower (10 m and 40 m) and Meteorological Tower 438 (24.4 m). A power law profile was fit to the LLNL 10-m and 40-m wind speed readings and used to extrapolate the LLNL wind speed to 24.4 m. Equation 3.1 was then used to calculate ΔS .

This method was used to generate a dataset of speed-up observations at Met 438 on a half-hourly basis between July 1, 2001, and June 30, 2003. Observations when the wind direction was between 235° and 245° were used in the comparison purposes.

All of the prediction schemes are limited to address only the case of a neutrally stable atmosphere. It has already been observed that stability significantly impacts flow in the Altamont Pass. The observations were grouped by Pasquill-Gifford stability class (“A” = unstable, “C” = neutral, “F” = very stable). Table 3-3 shows the average speed-up factor calculated for Met 438, as well as the standard deviation, and the number of times each stability class was observed when winds were between 235° and 245° . The average speed-up under neutral (class “C”) conditions was $\Delta S = 0.87$, which is within the range of values in Table 3-2. Interestingly, the least sophisticated methods (such as Eqn. 3.2b) gave the best predictions in this case.

Neutral conditions correspond to a minimum speed-up. It is believed that under stable conditions, winds can be high aloft but are prevented from mixing down to the plains. Under unstable conditions, it is believed that additional heating of the terrain to the east of the Pass results in a relative increase in wind speeds through the Pass. It should be noted that the standard deviation of ΔS within a stability class remains very high, suggesting that, at any given time, there may be a significant variation in actual conditions. This result suggests that the ability of the prediction schemes to accurately predict ΔS at an arbitrary, specific time is limited.

Table 3-3 Observed ΔS and standard deviation for each stability class at Meteorological Tower 438. Wind direction between 235 deg and 245 deg, July 1, 2001, to June 30, 2003.

Pasquill-Gifford Stability Class	ΔS	Standard Deviation	Number of Observations
A	1.12	0.47	6
B	1.27	1.67	133
C	0.87	0.52	200
D	1.52	1.10	563
E	2.93	1.74	151
F	3.28	2.38	51
All	1.64	1.47	1104

Defining the wind direction is somewhat problematic, since in reality it is possible for the wind direction at the one meteorological tower to be different from the direction at the second. ΔS is dependent on which tower is used to define wind direction and the range of wind directions that are included in the average. Table 3-4 illustrates this feature by tabulating the ΔS determined increasingly wider wind direction ranges based on both the LLNL tower and Met 438.

Table 3-4 Average ΔS observed for different wind direction inclusion criteria, such as which location was used to measure the wind direction, and how size range of directions included.

Wind Direction Range		Anemometer Location	Average ΔS		Num. Observations	
			All Data	Class C	All Data	Class C
235	245	LLNL	1.64	0.87	1104	200
225	255	LLNL	1.58	0.89	3409	614
210	270	LLNL	1.52	0.85	6398	1169
235	245	M438	1.51	0.81	1463	315
225	255	M438	1.62	0.83	4803	991
210	270	M438	1.98	0.85	9214	1565

By relaxing the requirement that the LLNL tower be upwind of Meteorological Tower 438 to calculate ΔS , the variation of ΔS with respect to wind direction can be investigated. Figure 3-3 presents the results. The wind direction at Meteorological Tower 438 was used as the representative wind direction in this case, since at off angles, the wind direction might vary appreciably in the plain relative to a ridge top location. As the wind vector varies northward from 240° (which is 0° relative wind direction), ΔS decreases as the wind direction becomes more aligned with the ridgeline until the a relative wind direction reaches about 60°. For negative relative wind directions and those at larger angles, ΔS increases when perhaps it would be expected to decrease. This could be due to a low number of observations and the fact that the actual ridge is different from the idealized two-dimensional modeled ridge, especially to the southeast where the ridgeline changes direction and increases in height.

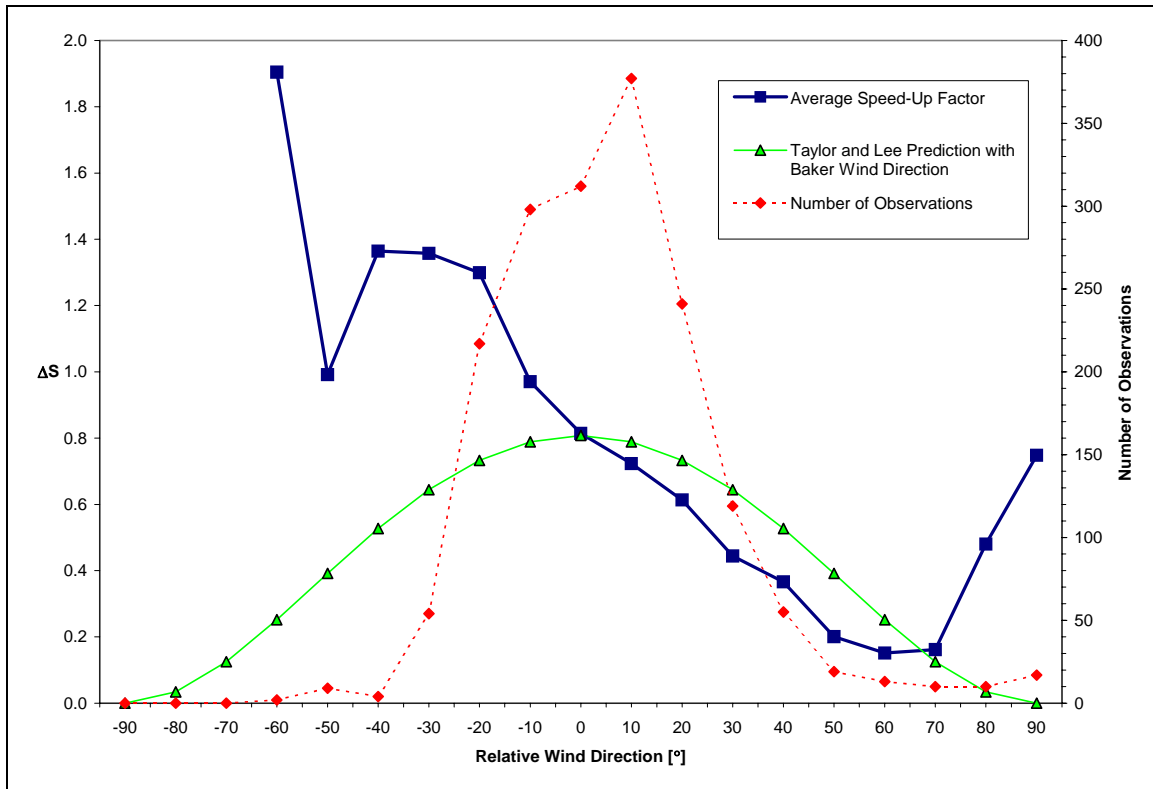


Figure 3-3 Average speed-up factor at Meteorological Tower 438 as a function of wind direction relative to the perpendicular to the ridgeline. A wind direction of 240° is perpendicular to the ridgeline and therefore corresponds to a relative wind direction of 0°. The chart also shows the number of observations included in each average. For comparison, results from the Taylor and Lee prediction scheme with a Baker wind direction modification are also shown.

The observed speed-up was also investigated for Powerworks meteorological tower 624 (“Met 624”). It is also situated near the entrance to the Pass, although it is on a promontory, has more terrain complexity in the direction of LLNL, and is not aligned as well relative to LLNL and the prevailing wind direction. For Meteorological Tower 624, $h = 196$ m and $L = 656$ m. In this case, for class “C” field measurements, ΔS was 0.96, although the lower slope of this hill (Meteorological Tower 624, $h/L = 0.30$) would have caused us to predict a lower ΔS than for Meteorological Tower 438 ($h/L = 0.47$).

Overall, the observed speed-up factors exhibited significant variability, even within the same stability class and wind direction range. Further application of the unmodified prediction schemes to sites within the Altamont Pass was hampered by the extremely complex terrain that made it difficult to estimate h and L at a given site, the fact that winds rarely blow perpendicularly to the ridgeline, and the lack of nearby flat reference sites.

Wind Tunnel Tests of Generalized Hills

For speed-up predictions to be applicable to wind energy uses, the wind direction must be factored into the prediction algorithm. Additionally, the algorithm must include more than circular or two-dimensional hill shapes. Since very little systematic data were available in the literature documenting how speed-up varies based on these parameters, researchers decided to conduct a series of tests of generalized hills in the ABLWT .

Test Specifications

For this test, a mechanical height probe and the laser spotting system were used to position the hot-wire anemometer. Hot-wire measurements were taken at 1000 Hz for 90 seconds. This corresponds to a full-scale time period of 46 to 286 minutes and Altamont Pass wind speeds from 4 to 25 m/s. A power law exponent of $\alpha = 0.19$ was achieved by systematically arranging a pattern of 8.9 x 14.6 x 1.9 cm (thin blocks) and 8.3 x 19.7 x 3.8 cm (thick blocks) wooden blocks over the flow-development section of the wind tunnel. The block pattern roughly consisted of half of each type of block configured in alternating sets of four and five blocks per row. The artificial grass used in the test section (mean height of 3 mm) was extended upwind and under the blocks. Additionally, the first three rows of blocks upwind of the test section were replaced with smaller blocks (Figure 2-4) to create a smooth flow transition from the roughness elements to the hill model. Figure 3-5 shows typical mean velocity profiles produced by this arrangement.

Hill Models

Three different hill models were manufactured from polystyrene foam. All of the hills had a sinusoidal cross-section and a height of $h = 38$ mm. An axisymmetric hill with a circular base was produced by revolving the cosine cross-section. An elliptical hill was made by stretching the circular hill so that the resulting elliptical footprint had a base length four times longer than the base width. A semi-infinite ("two-dimensional") hill model also was constructed with a cosine cross-section. Model surface roughness was maintained on the circular and elliptical hills by reproducing the topography using 2.5 mm steps, while the two-dimensional model was covered in artificial grass. The equation of the height of the surface $z(x,y)$ of these hills is

$$z = \frac{h}{2} + \frac{h}{2} \cos\left(\frac{\pi}{2L_1} (x^2 + A^2 y^2)^{1/2}\right) \quad (2.8)$$

where x and y are the horizontal distances from the hill peak. L_1 and L_2 are the half-lengths of the hill in the x and y directions. The half-length is the distance from the peak to the point on the slope where $z = h/2$. The aspect ratio of the hill is $A = L_2/L_1$. For the circular, elliptical, and two-dimensional models, $A = 1.0, 4.0$ and 0 respectively. All models had a primary half-length L_1 of 71.5 mm. See Figure 3-6 for details.



Figure 3-4 Roughness element arrangement used in ABLWT development section for generalized hill tests. The two-dimensional hill model at $\theta = 0^\circ$ and the measurement probe support with sighting laser and height probe installed are also visible.

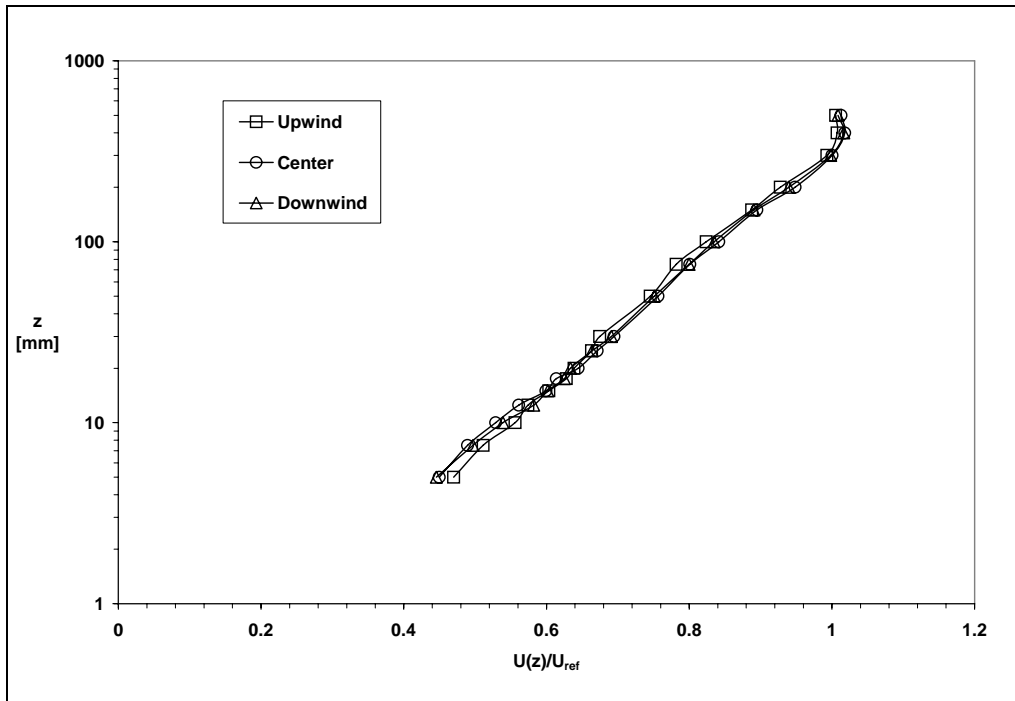


Figure 3-5 Dimensionless velocity profiles in empty UC Davis Atmospheric Boundary Layer Wind Tunnel test section with artificial grass covering floor at three locations: at center, and 68 cm upwind, and downwind of center.

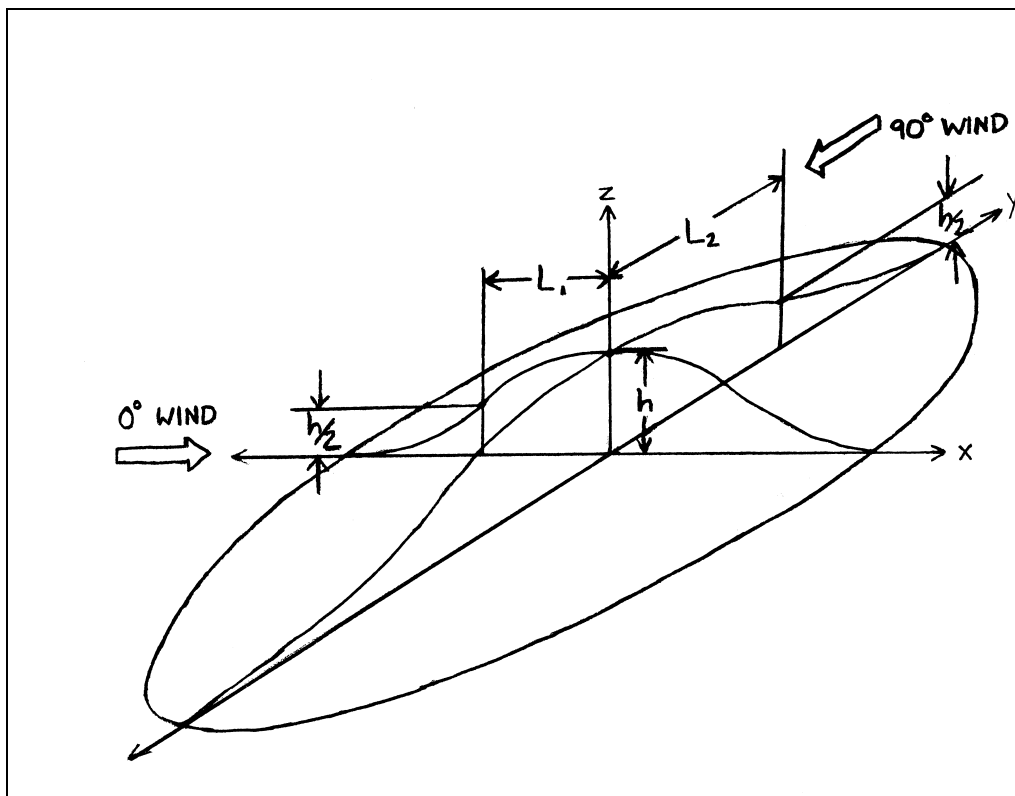


Figure 3-6 Schematic diagram of the hill models.

Effects of Model Roughness

The model surface must be rough enough to maintain a turbulent flow over the model surface. Generally, this means that the roughness Reynolds number must be greater than about 2.5. Practically, this means that the model must not be "aerodynamically smooth." Model roughness can be provided by coating or covering the surface in a suitable material. Previous investigators of speed-up over two-dimensional hills used studded rubber sheets (Gong and Ibbetson, 1989), artificial grass (Kim et al., 1997), uniformly spread sand (Baker et al., 1985), and textured wall paper (Carpenter and Locke, 1999).

Roughness also can be achieved by using "steps" or "terraces." This latter type of roughness can be a by-product of model construction. If the terrain is carved from a large block of material using mapped contours to guide the cutting tool, the result is a "stepped" model where the edge of each step follows one of the mapped contour lines. The maximum step size depends on the scale of the features modeled, since larger steps cause a greater departure from geometric similarity. Derickson and Peterka (2004) tested a 1:4000 scale model of complex terrain of Lantau Island, Hong Kong, in an ABLWT, using a model with 3-mm steps. The space between the steps was then carefully filled with plaster to make a "smoothed" model, and the test was run again. Little difference was observed in the resulting near-surface velocity profiles measured at several points on the model.

However, if the steps become too large, they begin to interfere with the properties of the flow. Lindley et al. (1981) modeled Gebbies Pass, New Zealand, at 1:4000 scale in both stepped and "smooth" configurations, and found the stepped model performed very poorly. This may be attributable to the large step size of 1 cm, and the fact that the range between the highest and lowest points of the model encompassed only 11 steps. Although generally low, the effect of model roughness is most pronounced at and downstream of separation points on the model, since the exact location of a separation point is a strong function of perturbations in the local model geometry and generally unsteady in time. Miller and Davenport (1998) performed ABLWT tests on two-dimensional sinusoidal hill models with maximum slopes of 0.5 (steep enough to expect lee side flow separation), and reported up to 40% greater velocities at the surface on the hill peak, although the difference decreased rapidly with height and was minimal above $z/h \approx 0.5$.

The circular and elliptical hill models in this study were fabricated with 2.5 mm steps. The two-dimensional ridge was covered in artificial grass to ensure a consistent surface roughness regardless of orientation in the wind tunnel. For all three hills, artificial grass covered the entire floor of the test section. Previous experiments showed that if the test section floor was left as an untreated bare plywood surface, an internal boundary layer formed in the test section, causing unacceptable variation in velocity measurements with test section position.

Two-Dimensional Ridge and Three-Dimensional Circular Hill

Most previous wind tunnel studies concentrated on two hill configurations: two-dimensional ridges with the wind blowing perpendicularly across the ridge and three-dimensional axisymmetric hills with a circular "footprint". Both of these configurations were tested in the UC

Davis ABLWT. Results were reasonably consistent with other studies. Interestingly, Eqns. 3.2 a and b overpredicted the maximum speed-up ΔS_{\max} , generally by more than 15%, for every data set except Gong and Ibbetson's (1989), which show very good agreement between measurements and Eqns. 3.2 a and b.

Hill Aspect Ratio

Combining results from the 0° and 90° wind direction tests of the three hill models, it is possible to observe how ΔS changes as a function of the hill aspect ratio A . Figure 3-7 shows the hilltop speed-up profiles for four of the aspect ratios tested. ($A = 0$ is not plotted as $\Delta S \approx 0$.) The figure also presents the speed-up data predicted by the LSD method.

Equation 3.6b was optimized by varying the constants C_1 , C_2 and C_3 to “best fit” the wind tunnel data in Figure 3-7. Best fit was determined by minimizing the total absolute error between the wind tunnel measurements and the LSD prediction for the five profiles. The minimum average absolute error of 0.023 was obtained using almost the same constants specified by LSD: $C_1 = 2.3$, $C_2 = 0.2$ (instead of 0.4) and $C_3 = 2.0$.

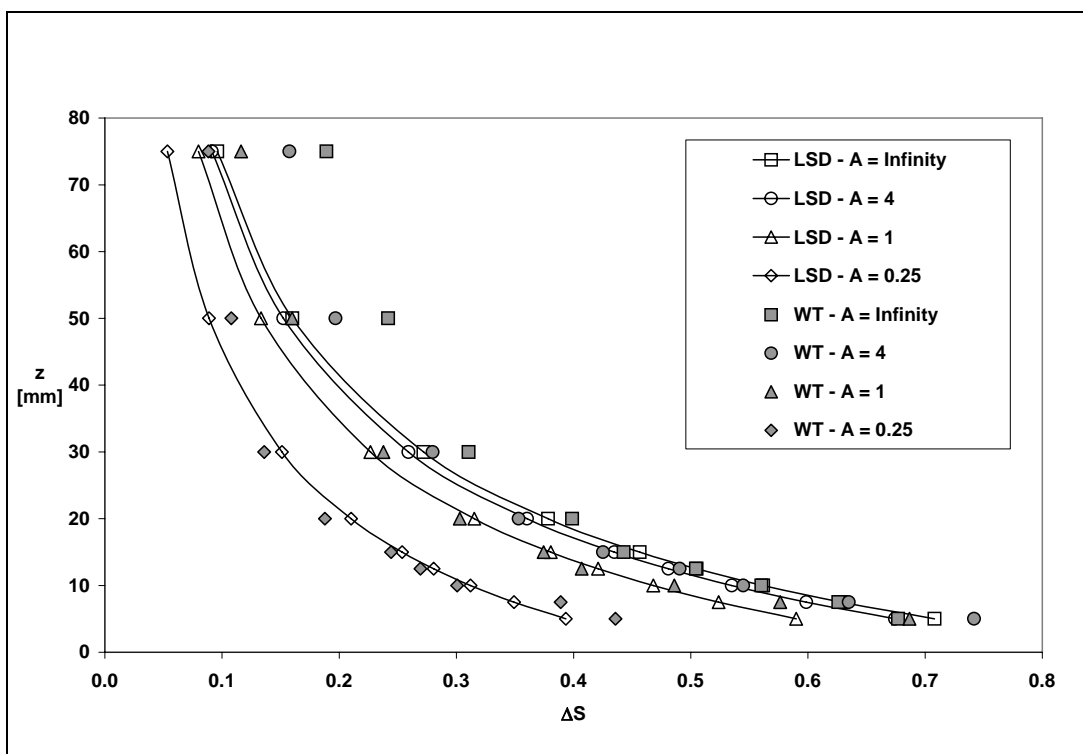


Figure 3-7 Hilltop speed-up factor profiles for four hill aspect ratios: $A = 0.25$, 1, 4 and infinity. WT is the wind tunnel measurement. LSD is the predicted speed-up using Eqn. 3.9b with $C_1 = 2.3$, $C_2 = 0.2$, $C_3 = 2.0$.

Hill Shoulder

It is interesting to note the variation of the speed-up factor at the “shoulder” measurement locations as the aspect ratio is changed. The shoulder locations are those where $x = 0$ with a 0° wind. Measurement points available included $y = 0$ (the hilltop) and $y = L_2$ (the “shoulder face”). Wind tunnel width limitations precluded taking base measurements ($y = 2L_2$) for $A = 4$. It is apparent that the values of ΔS peak for the circular hill ($A = 1$), as shown in Table 2-5. This effect is believed to be due to lateral (“y direction”) acceleration of the flow horizontally on the windward face of the hill, in addition to the longitudinal (“x direction”) acceleration that is the primary cause speed-up.

Table 3-5 Measured values of ΔS at the shoulder location ($x = 0$, $y = L_2$, $\theta = 0^\circ$) at different heights above ground z , for hills of different aspect ratio $A = L_2/L_1$.

z [mm]	A					
	Infinity	4	1	0.25	0	
5	0.677	0.487	0.532	0.249	-0.043	
7.5	0.626	0.409	0.437	0.239	-0.027	
10	0.560	0.331	0.360	0.174	-0.024	
12.5	0.504	0.257	0.289	0.158	-0.018	
15	0.443	0.210	0.250	0.150	-0.009	
20	0.399	0.169	0.225	0.115	0.004	
30	0.310	0.099	0.157	0.085	0.011	
50	0.242	0.051	0.095	0.063	0.017	
75	0.189	0.006	0.081	0.053	0.027	

Effects of Wind Direction

Measurements were taken at five similar points on both the two-dimensional and elliptical hills: at the base and half-height on both windward and leeward slopes, and at the hilltop. Profiles also were taken at both half-height points along the long axis of the elliptical hill. Measurements were taken at $z = 5, 7.5, 10, 12.5, 15, 20, 30, 50$ and 75 mm above each point, giving a range of z/h between 0.13 and 1.97. The elliptical and two-dimensional models were rotated and individually tested in the ABLWT to simulate wind from $0^\circ, 15^\circ, 30^\circ, 45^\circ, 60^\circ, 75^\circ$ and 90° relative to the short axis of the hill. Since the models were symmetric, this was sufficient to characterize the velocity profile for wind from $+90^\circ$ to -90° at 15° intervals. As the two-dimensional hill model was rotated, additional sections were added to the model so that it extended to flush interfaces with both side walls of the test section at angles up to 75° . For the 90° test, the two-dimensional hill model was terminated at the downwind edge of the test section and two meters upwind into the development section by smoothly bringing the artificial grass surface down to floor level over approximately 0.5 meters.

Additionally, for each model and wind direction, profiles of mean velocity and turbulence intensity were taken upwind of the hill location for all directions up to 60° . This was not possible for the 75° and 90° directions, where portions of the hill models themselves were effectively upwind. For these directions, an average of the mean velocity profiles for the other directions

was used to calculate speed-up factors. Since the profiles showed minimal variation, this was not considered to have introduced significant error.

Generally, the range of speed-up factors observed for the two-dimensional hill was somewhat greater than the range observed over the elliptical hill. For the top of the two-dimensional hill (Figure 3-7), speed-up factors at angles near 0° were the highest ($\Delta S = 0.677, 0.718$) at the lowest measurement point 5 mm above the surface and decreased as height above the surface increased ($\Delta S = 0.504$ at $z = 12.5$ mm). At angles greater than 45° , the variation in ΔS decreases, as the component of the wind parallel to the slope increases, until at 90° , $\Delta S < 0.06$ for all of the measurement points.

On the slope face (Figure 3-9), ΔS reached a much lower maximum of 0.24, and showed less variation with either height or direction than the hilltop. Except for very close to the surface, speed-up at a given height varies roughly linearly from a maximum at $\theta = 0^\circ$ to $\Delta S \approx 0$ at $\theta = 90^\circ$.

The hill base area is a region of reduced velocity near the surface at low values of θ . For the two-dimensional hill (Figure 3-10), the minimum $\Delta S = -0.27$ occurs at $z = 5$ mm and $\theta = 0^\circ$, and speed-up factors go to zero by $z/h = 2$. Similar minimum values of ΔS are observed at $\theta = 0^\circ$ for the elliptical hill (Figure 2-13, minimum $\Delta S = -0.30$) and circular hill (Figure 2-16, minimum $\Delta S = -0.25$). It is interesting to note that for all three hills, ΔS trends uniformly from a minimum at $\theta = 0^\circ$ to a maximum at $\theta = 90^\circ$. While this maximum is about zero for the two-dimensional hill, it is higher for the elliptical hill (maximum $\Delta S = 0.14$). The overall trend is higher still for the circular hill.

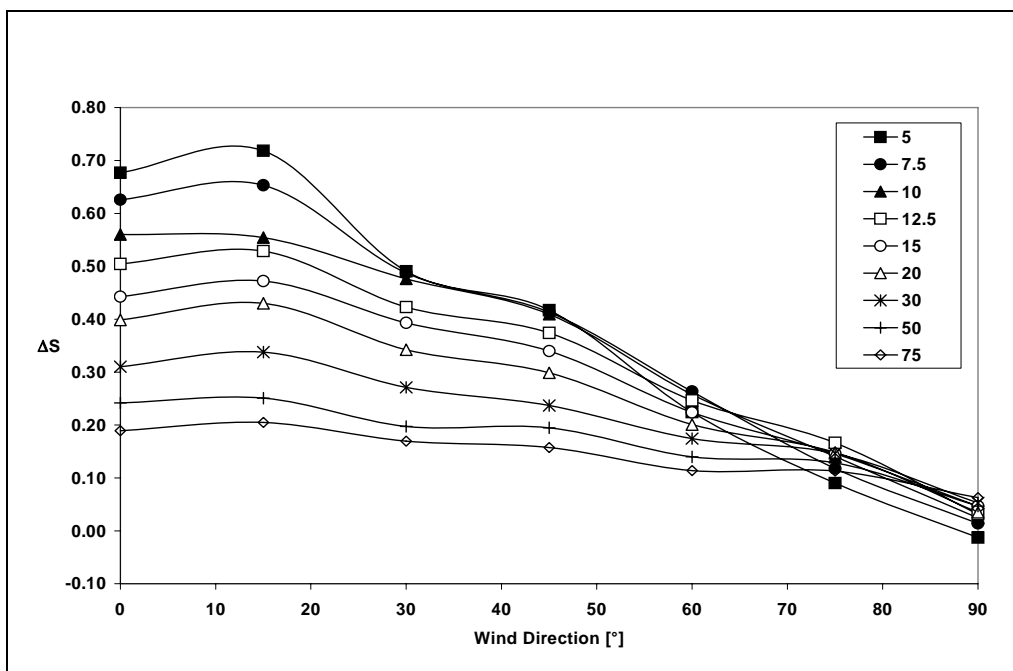


Figure 3-8 Speed-up factor versus wind direction for two-dimensional hill at hilltop. Wind from 0° is perpendicular to ridgeline. Wind from 90° is parallel to ridgeline.

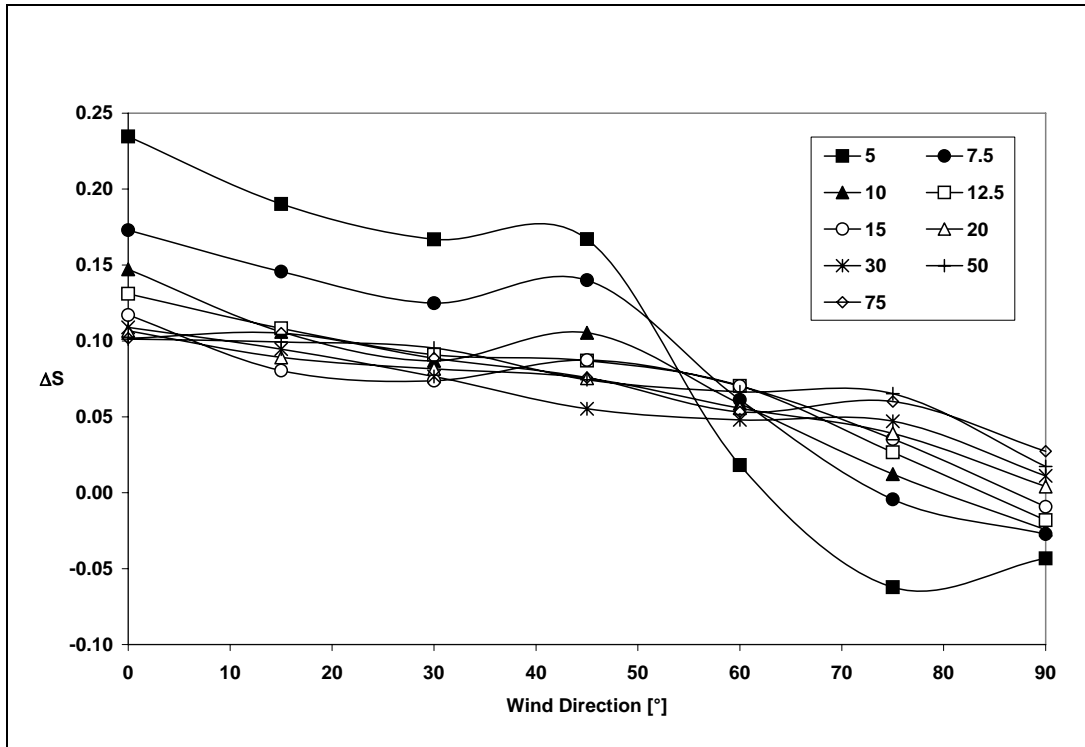


Figure 3-9 Speed-up factor versus wind direction for two-dimensional hill at half-height on slope (“face”). Wind from 0° is perpendicular to ridgeline, with measurement point on windward side. Wind from 90° is parallel to ridgeline.

The variation of ΔS with θ at the hill face measurement point also depends strongly on the hill aspect ratio. For the two-dimensional hill, ΔS trends from maximum values at $\theta = 0^\circ$ to $\Delta S \approx 0$ at $\theta = 90^\circ$ (Figure 2-9). For the elliptical hill (Figure 2-12), the variation of ΔS is less pronounced, with ΔS slightly lower at $\theta = 0^\circ$ than at $\theta = 90^\circ$. The trend for the circular hill is opposite that of the two-dimensional hill. ΔS trends from minimum values at $\theta = 0^\circ$ to maximum values at $\theta = 90^\circ$.

Some of the variation in ΔS for the base and face points appears to be caused by a “cross flow” phenomenon. As the wind strikes the circular hill, a percentage of air is pushed up and over the summit, with the remaining air pushed horizontally around the sides of the hill. This would cause speed-up factors to be higher around a hill of aspect ratios near one, while this effect would be minimal as the aspect ratio approached 0 or ∞ .

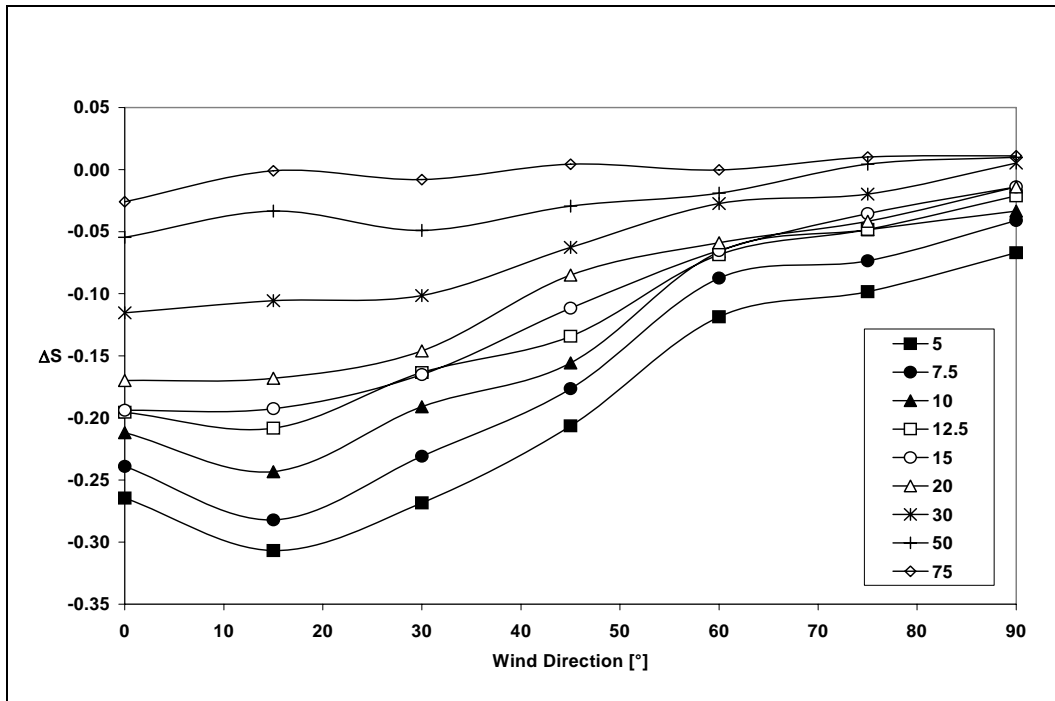


Figure 3-10 Speed-up factor versus wind direction for two-dimensional hill at base of hill. Wind from 0° is perpendicular to ridgeline, with measurement point on windward side. Wind from 90° is parallel to ridgeline.

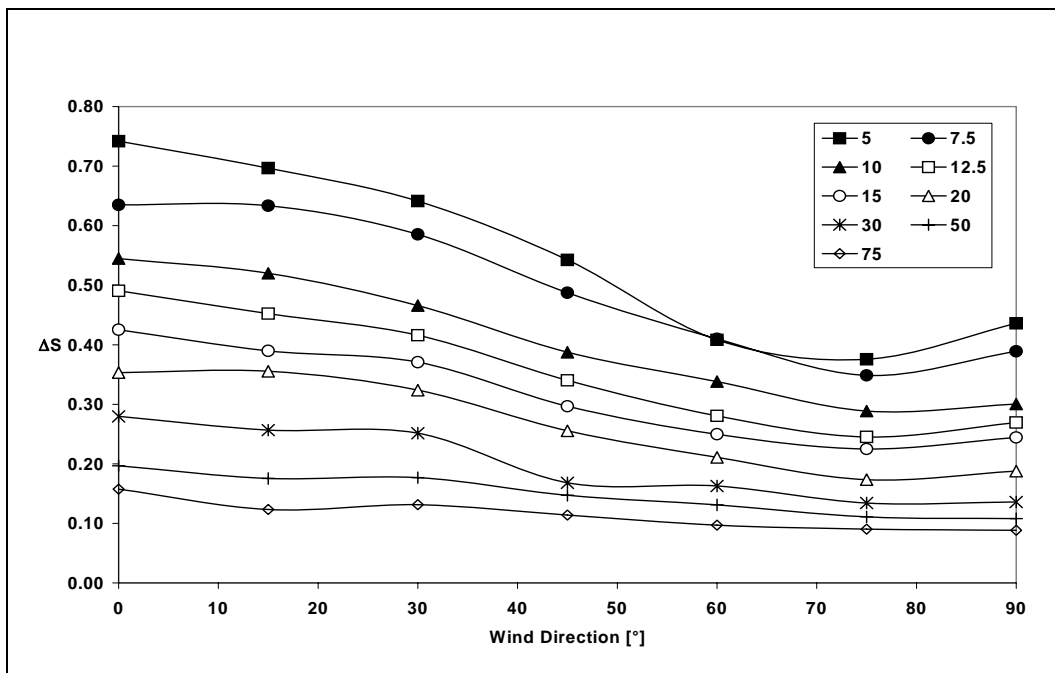


Figure 3-11 Speed-up factor versus wind direction for elliptical hill at hilltop. The wind direction from 0° is perpendicular to the ridgeline, from the 90° wind direction is parallel to the ridgeline.

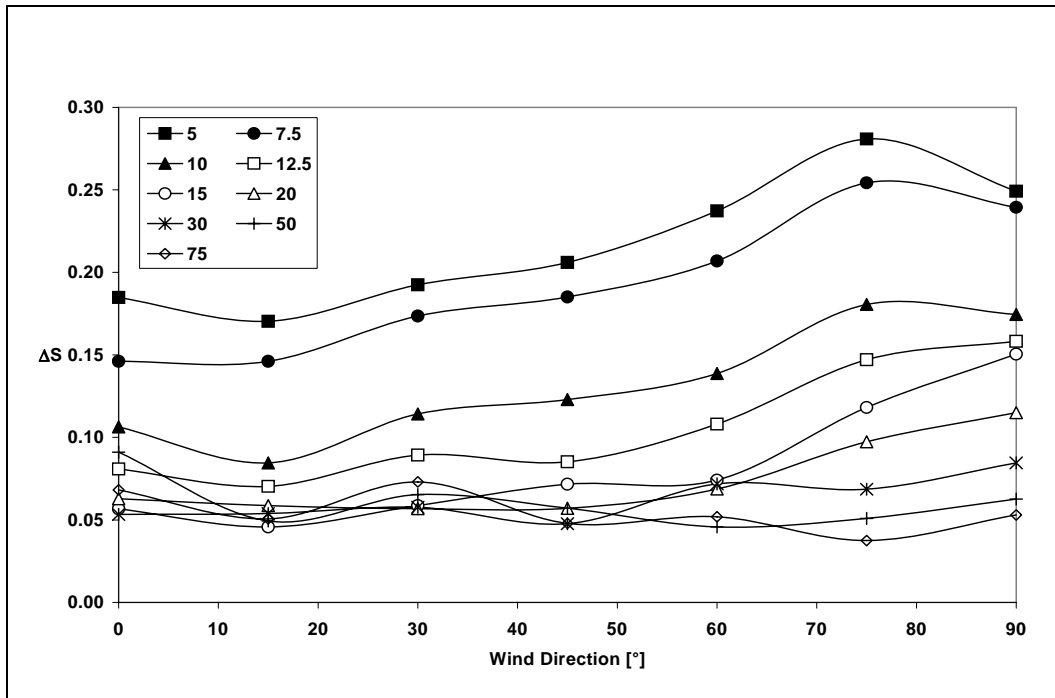


Figure 3-12 Speed-up factor versus wind direction for elliptical hill at half-height on slope. Wind from 0° is perpendicular to ridgeline, with measurement point on windward side. Wind from 90° is parallel to ridgeline.

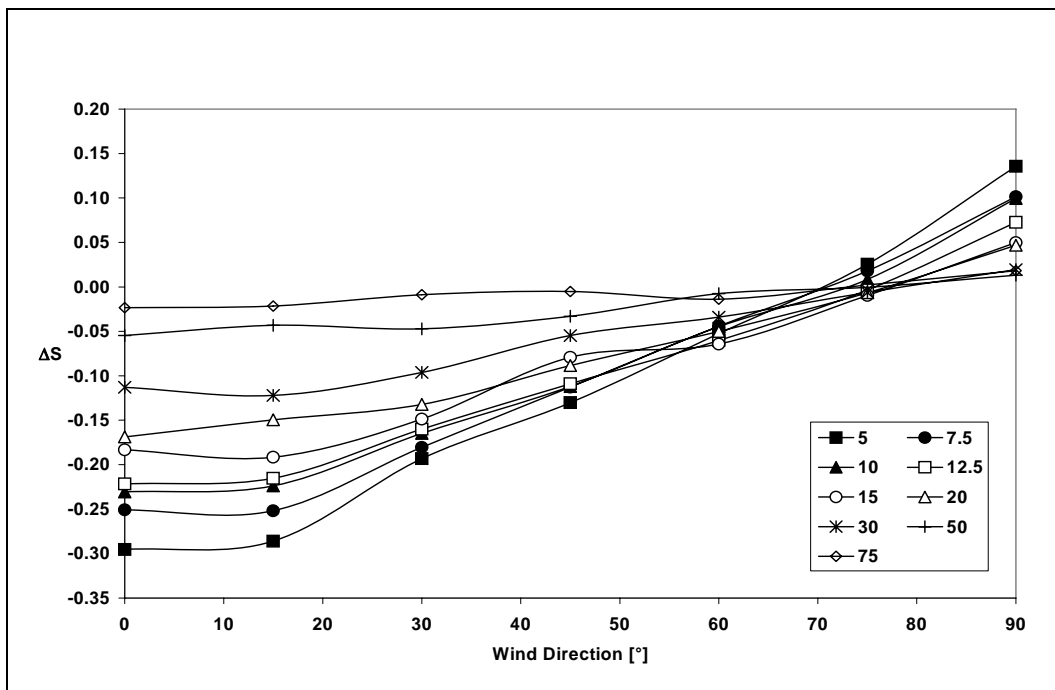


Figure 3-13 Speed-up factor versus wind direction for elliptical hill at base of hill. Wind from 0° is perpendicular to ridgeline, with measurement point on windward side. Wind from 90° is parallel to ridgeline.

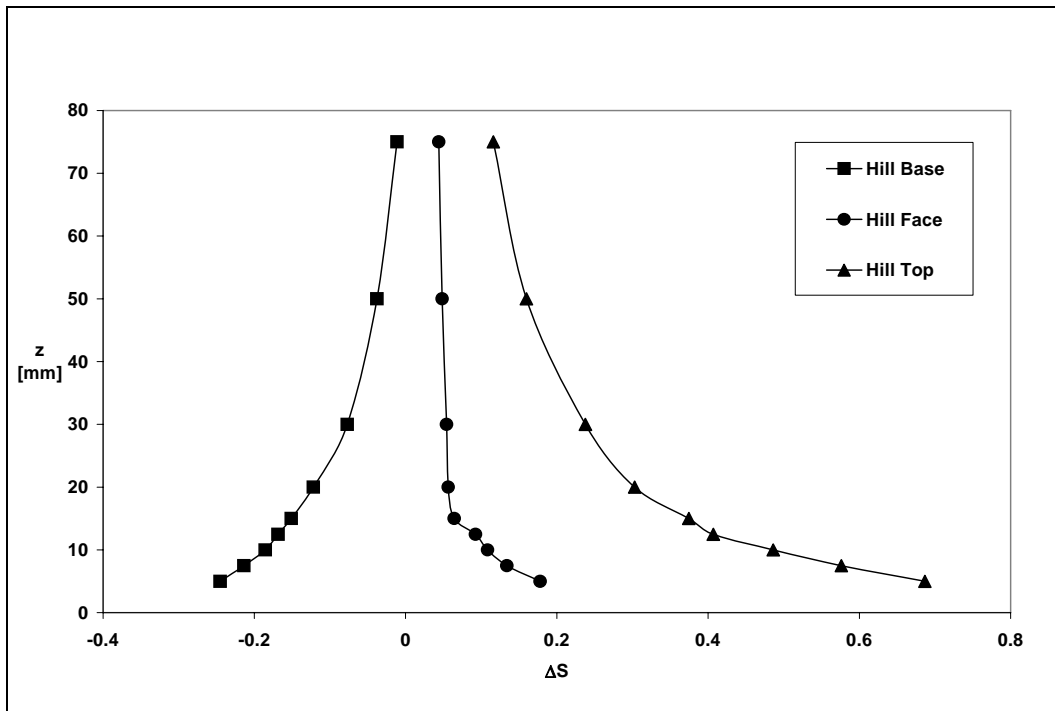


Figure 3-14 Speed-up factor versus height for circular hill at hilltop at top, face and base.

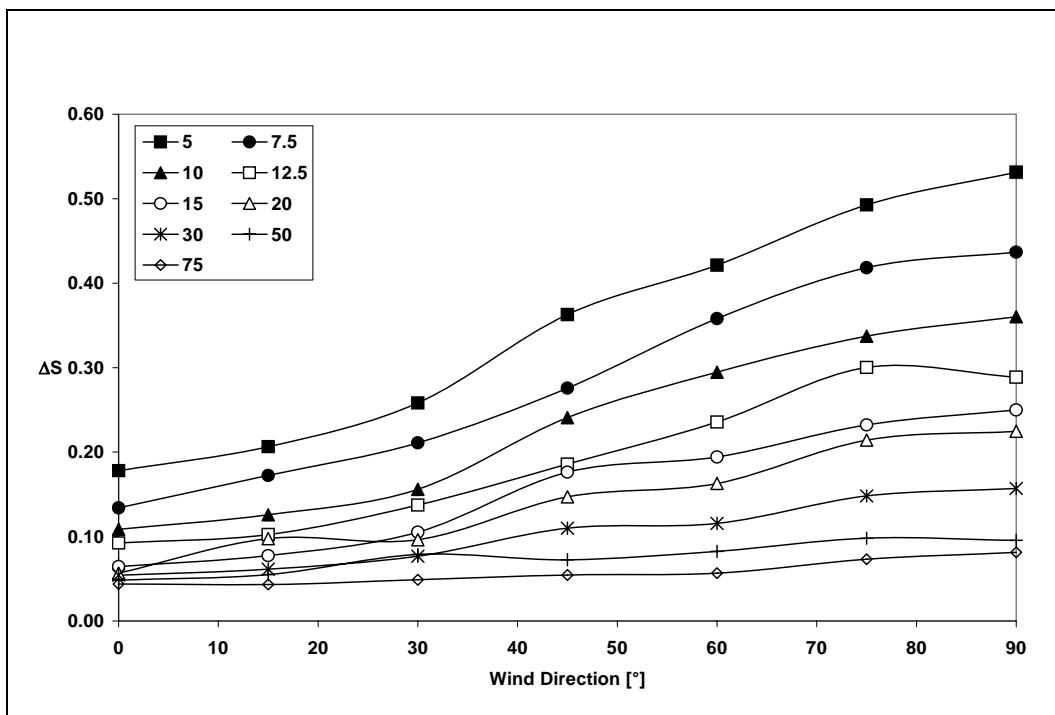


Figure 3-15 Speed-up factor versus wind direction for circular hill at half-height on slope. Point is centered on upwind face when wind is from 0°. Point is on shoulder of hill when wind is from 90°.

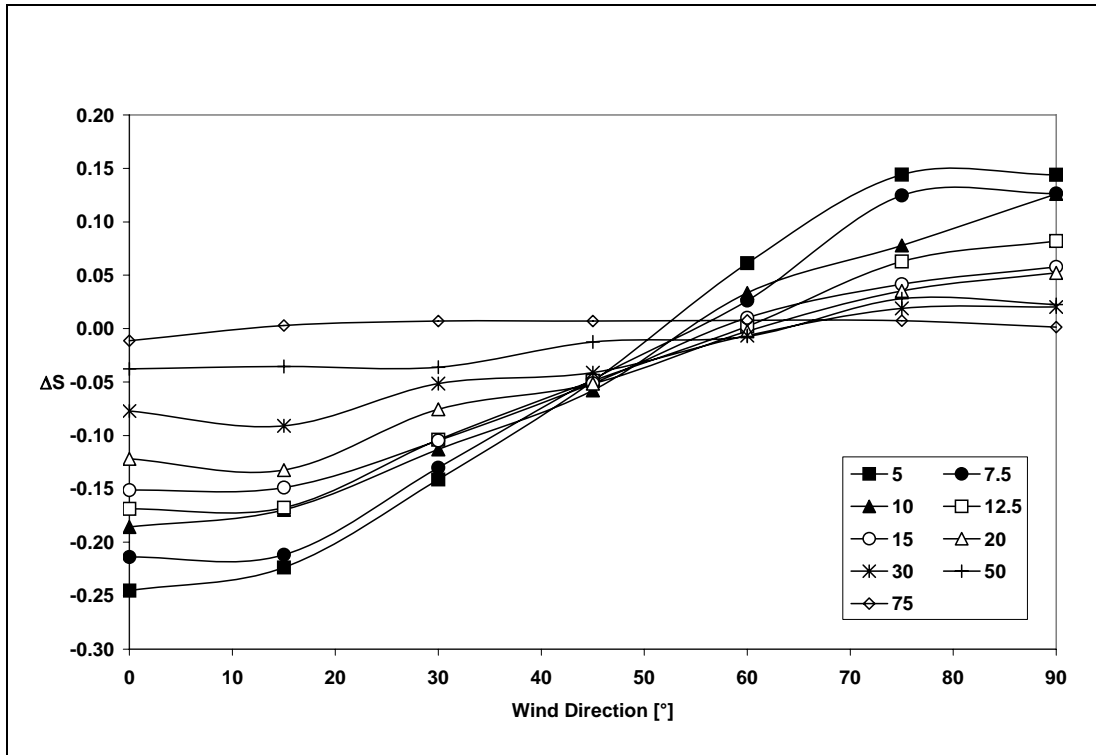


Figure 3-16 Speed-up factor versus wind direction for circular hill at base of hill. Point is directly upwind of hilltop when wind is from 0°. Point is on shoulder of hill when wind is from 90°.

Analysis of Prediction Schemes

For the hilltop of the two-dimensional ridge, the existing speed-up prediction algorithms can be modified in a straightforward manner to include wind direction effects. As well as the Baker and FAA interpolation methods described earlier, it is also possible to fit simple cosine curve to describe wind direction variation.

$$\Delta S(\theta) = \Delta S_o (0.5 + 0.5 \cos(2\theta)) \quad (3-9)$$

$$\Delta S(\theta) = \Delta S_o \cos(\theta) \quad (3-10)$$

The Baker method (Eqn. 3.7), the FAA method, and the two cosine fits were applied to the speed-up prediction algorithms for the top of the two-dimensional hill. Figure 3-17 shows the hilltop ΔS predicted at $z = 10$ mm by applying each of the four wind direction methods to the results of the Weng non-linear prediction algorithm. This allows comparison of the results obtained when the different wind direction methods are applied in an otherwise identical prediction algorithm. The FAA method was found to be more conservative (i.e., overpredicting speed-up) than the others.

The method of minimizing error between the predicted and wind tunnel measured speed-up factors was used to rank the prediction accuracy of each combination of prediction algorithm and wind direction interpolation. For each combination, the mean error (indicating bias) and mean absolute error in the predicted speed-up values were calculated for the elliptical and two-dimensional hill over all wind directions and all measurement heights. Table 3-6 presents the results, ordered from “best” to “worst” in the present context. Unfortunately, it is difficult to draw significant conclusions at this point, since the accuracy of each prediction algorithm cannot be separated from the accuracy of the wind direction interpolation.

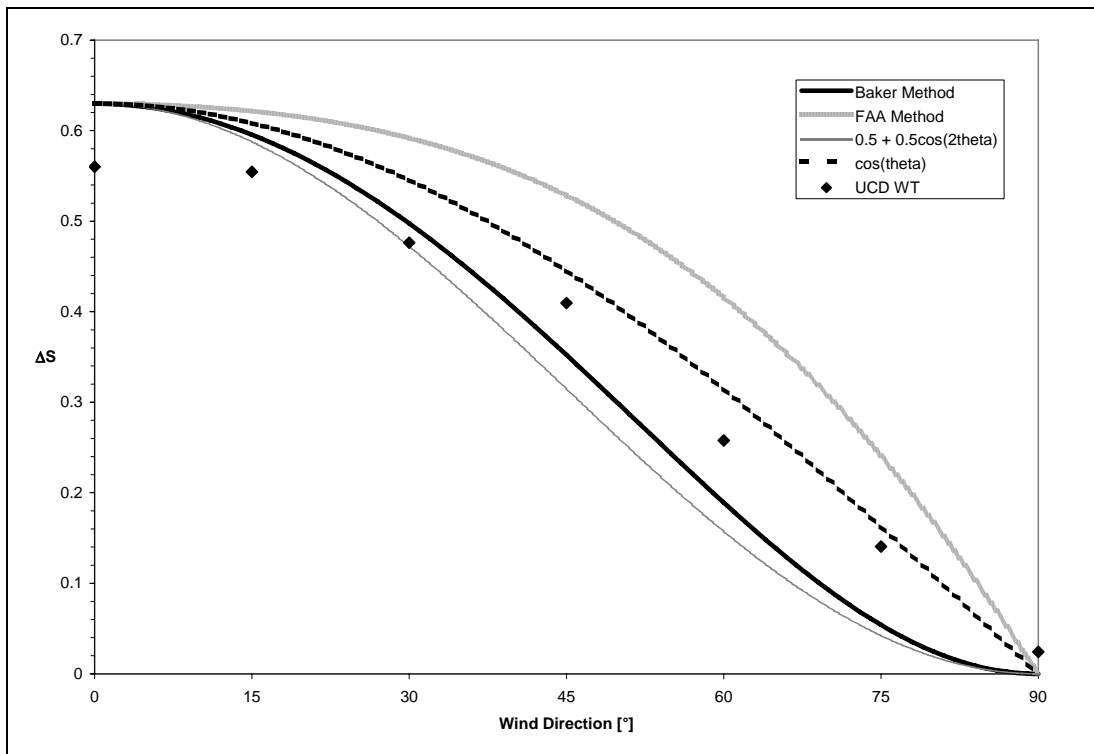


Figure 3-17 Speed-up factors for the two-dimensional hill top at $z = 10$ mm predicted by the non-linear Weng et al. formulation, using four different wind direction interpolation methods.

It is also noted that this approach of applying the pre-existing prediction algorithms and a wind direction interpolation does not translate to points that are not located on the hilltop. Therefore, it was necessary to formulate a new speed-up prediction algorithm to accomplish this goal. This was done by modifying the LSD method, the available method covering the greatest range of phenomena, to incorporate both wind direction dependence and the negative speed-up that are observed at the base of a steep hill.

Table 3-6 Hilltop speed-up prediction accuracy comparison for each combination of speed-up prediction algorithm and wind direction interpolation method.

Prediction Algorithm	Wind Direction Interpolation Method	ME	MAE
LSD	FAA	-0.01	0.08
LSD	cos(theta)	-0.01	0.08
LSD	0.5+0.5cos(2theta)	0.06	0.10
LSD	Baker	0.08	0.11
FAA	Baker	0.05	0.12
FAA	FAA	0.05	0.12
FAA	0.5+0.5cos(2theta)	0.05	0.12
FAA	cos(theta)	0.05	0.12
WTS	cos(theta)	0.12	0.20
W Non-Linear	cos(theta)	0.13	0.20
WTS	FAA	0.13	0.20
W Non-Linear	FAA	0.14	0.20
W Linear	cos(theta)	0.16	0.22
W Linear	FAA	0.17	0.23
WTS	0.5+0.5cos(2theta)	0.21	0.25
W Non-Linear	0.5+0.5cos(2theta)	0.22	0.26
W Linear	0.5+0.5cos(2theta)	0.25	0.28
WTS	Baker	0.35	0.36
W Non-Linear	Baker	0.36	0.36
W Linear	Baker	0.42	0.42

Modified LSD Prediction Scheme

A speed-up factor prediction scheme is presented below. This method is valid only when considering a point on the upwind side or ridgeline of the hill. It is based on the LSD method, with modifications that account for the negative speed-up factors that occur near the surface at the base of steeper ($h/L_1 > 0.4$) hills. Wind direction is also included by using a modified LSD method to estimate the speed-up at the point of interest for wind directions between $\theta = 0^\circ$ and $\theta = 90^\circ$ from its two orthogonal components. For wind directions between 0° and 90° , the speed-up factor is calculated as follows:

1. Calculate hill slope:

$$\phi = h_p / L_p$$

2. Calculate expected maximum speed-up at hilltop and minimum speed-up at base.

$$\text{If } \phi \leq 0.4: \quad \Delta S_{\max} = 1.75\phi \quad \Delta S_{\min} = 0$$

$$\text{If } \phi > 0.4: \quad \Delta S_{\max} = 0.7 \quad \Delta S_{\min} = \exp\{-2.5(\phi - 0.4)\} - 1$$

3. Calculate the expected speed-up for a wind blowing parallel to the x axis, adjusted for position on hill face and height above the surface:

$$\Delta S_{norm} = \frac{\Delta S_{min} + 0.5(\Delta S_{max} - \Delta S_{min})(1 + \cos(0.5\pi x / L_1))}{\left(1 + \frac{2z}{L_1}\right)^2}$$

4. Next, using the un-modified LSD method (Eqns. 2.5a, 2.5b), calculate ΔS_{orth} , the expected speed-up at the point if the wind was blowing from the “side” of the hill. That is, calculate the speed-up for wind parallel to the y axis, instead of wind parallel to the x axis. This can be done most easily by rotating the hill 90° in the coordinate system, noting that A, L_p and the coordinates of the point are all changed by this operation and then applying Eqns. LD1 and LD2.
5. Finally, interpolate vector between ΔS_{norm} and ΔS_{orth} to get ΔS at the required wind direction θ :

$$\Delta S = \Delta S_{norm} \cos \theta + \Delta S_{orth} \sin \theta$$

Applying this method to all of the points and heights measured in the wind tunnel, the mean absolute error of the ΔS predictions was 0.052, compared to 0.076 for the original LSD method, using the Baker wind-direction interpolation.

Generalized Hill Test Conclusions

The variation of speed-up over an elliptical hill varies considerably depending on the hill aspect ratio, wind direction, and the position of the point of interest on the hill. For the specific case of the hilltop of the two-dimensional ridge tested, a simple cosine of the wind direction was found to be a better interpolating factor than the other methods considered.

The wind tunnel test results highlighted the limitations of current empirical speed-up prediction models. For the most part, current models do not include the negative speed-up that occurs at the base of steep hills, effects of non-orthogonal wind directions, or the local horizontal component of flow acceleration that occurs on the sides of hills with aspect ratios near one. A method of extending the LSD method (currently the most complete model) to include these effects was developed, which are most pronounced for steeper hills, while maintaining the validity of the un-modified LSD method for hills with smaller slopes.

4

The Wind Farm Power Curve

The primary factor determining the power output of a wind turbine is the wind speed at turbine hub height. The function that predicts the power production of a turbine based on an input wind speed is called the power curve of the wind turbine. If the concept of the power curve is extended to an entire wind farm, it is called the "wind farm power curve" or "plant-scale power curve". In this case, the input wind speed is a reference wind speed within or near the wind farm, usually the wind speed measured at the wind farm's meteorological tower. The power output indicated by the plant-scale power curve at a given wind speed predicts the power production of the entire wind farm.

Determining an accurate wind farm power curve is more difficult than determining the power curve of a single turbine. The wind farm power curve is sensitive to additional factors such as wind direction, atmospheric stability, topography, and turbine wake effects on downwind turbines. The main difficulty is estimating how the wind speed at each turbine location varies relative to the wind speed at the meteorological tower (or other wind speed reference location). As described below, a novel approach is to use an ABLWT to map the variation of wind speed over the wind farm site. Individual turbine power curves could then be used to estimate the wind farm's power production if the wind speed at the meteorological tower is known. Alternatively, a numerical potential flow solver can be used to map the wind speed variation by simulating potential flow over the local terrain. Both of these methods are applied to the Altamont case study wind farm, and the results are compared to power curves generated using "traditional" methods using historical data and statistical analysis. The performance of the power curves is also evaluated in a forecast mode using a forecast archive supplied by AWS Truewind.

Power Curve Derived From Wind Tunnel Data

Wind Tunnel Modeling of Altamont Pass Terrain

Simulation of terrain in the atmospheric boundary layer wind tunnel (ABLWT) requires construction of a model of the terrain capable of simulating the full-scale three-dimensional flow. The scale of the terrain surface features of the model must be large enough so that the hot-wire anemometer, which has a finite length on the order of several millimeters, has sufficient resolution to measure flow variations caused by the surface features. The wind tunnel simulates a fully turbulent flow.

The first ABLWT investigation of the Altamont Pass wind farm site was performed at UC Davis by James Cheng in 2002. He demonstrated that the ABLWT could be used to predict the power output of wind turbines in complex terrain with reasonable accuracy (Cheng, 2002, White and

Cheng, 2002). This study involved a wind tunnel test simulating two clusters of wind turbines owned by Powerworks, Inc., in the Altamont Pass region. A model of the terrain was constructed at 1:2400 scale that simulated a region 2.6 km wide by 8.8 km long, with the long axis aligned with 240°, the prevailing wind direction format Altamont Pass. Wind-speed measurements were made at each turbine site at the scale hub height. Turbine wake effects were not considered. On-site meteorological ("met") towers recorded wind speed, which was used in conjunction with the wind tunnel measurements and the wind-turbine power curve to predict the power output of the wind farm for given meteorological conditions. The predicted power production was compared to the recorded power production, and the average error was 20% during the summer months and ±40% during the winter months, when power production was lower and more erratic. The tests also demonstrated that the wind tunnel predictions of near-surface winds were most accurate during seasons and times of day when neutral or unstable flow occurs (Cheng et al., 2004). This phase of the project was completed as part of the first California Energy Commission and Electric Power Research Institute California Wind Forecasting Project (EPRI 2003a and 2003b).

The research documented here is the continuation of the work initiated by Cheng (2002). Additional terrain models were constructed to characterize wind speed distributions when the wind direction was varied among four directions for one of the turbine clusters in the original study (called "Met 127").

Five wind tunnel model sections, each 46 by 48 inches, were constructed to simulate the Met 127 turbine cluster and surrounding areas (Figure 4-3). The first three sections were produced by a contractor, and reproduce the terrain in dense polystyrene foam in 2.5 mm steps (Figure 4-1). These three panels were used by Cheng (2002) and by the author to simulate the 240° and 60° wind directions. Two additional panels were constructed by the author. These panels were constructed in 12.7 mm steps. The steps were then filled with a plaster compound to form the shape of the terrain (Figure 4-2). The plaster surfaces were intentionally left rough to maintain turbulent flow along the surface. The expanded model was tested over four simulated wind directions, and the original prediction scheme used by Cheng (2002) was enhanced to use both wind speed and direction measured at the met tower as well as ambient air density to predict the power production of the Met 127 turbine cluster.

Wind speed and turbulence intensity were measured for many turbine locations on the model at simulated hub height, and for the met tower at anemometer height. In some cases, where turbines were closely spaced along ridgelines, every other turbine position was measured. Wind speeds for unmeasured turbine locations were estimated by averaging the measured wind speeds at the adjacent turbine locations on either side. The measurements were made for each of the simulated wind directions, $\theta = 60^\circ, 150^\circ, 240^\circ$ and 330° . At the end of the test, the resulting database presented in Appendix A contained four measurements of wind speed at the met tower and at each turbine location measured ($U_{\text{turb,tunnel}}$), one for each of the wind directions tested.



Figure 4-1 Model in wind tunnel simulating 60° wind direction. Met 127 turbine cluster is on center yellow panel. Met 225 turbine cluster (only tested for 240°) is on rearmost panel.



Figure 4-2 Model in wind tunnel simulating 150° wind direction. Wind blows towards camera.

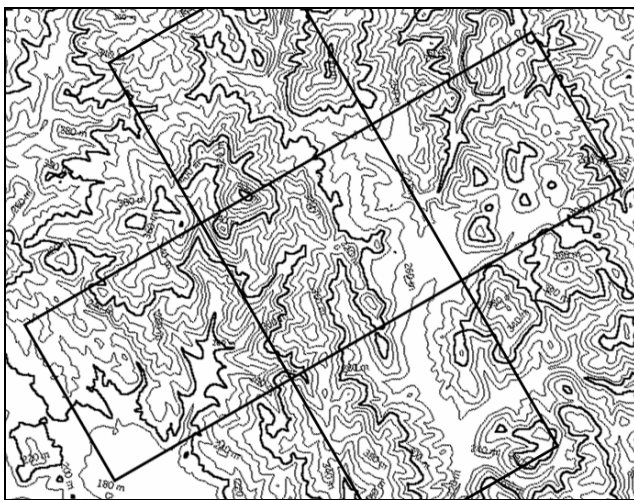


Figure 4-3 Map of modeled terrain, with area covered by model panels outlined. Mapped area is 9.6 km by 7.3 km. Contour interval is 20 m. North is vertically upward.

For each turbine location, four wind speeds $U_{\text{turb,tunnel}}(\theta = 60^\circ, 150^\circ, 240^\circ, 330^\circ)$ were measured; however, winds blow from all directions, and $U_{\text{turb,tunnel}}(\theta)$ is a continuous function of θ . Therefore, a curve was fit to the four points of wind speed data as a function of position along the ridge line of the wind farm areas. This fit used a cubic spline with a matching condition at 0° and 360° . For a wind turbine on a long ridge, $U_{\text{turb,tunnel}}(\theta)$ can be expected to exhibit two maximums that occur when the wind direction is roughly normal to the ridgeline, and two minimums when the wind is roughly parallel to the ridgeline.

Figure 4-4 shows the interpolated dimensionless wind speed, $R = U_{\text{turb,tunnel}}/U_{\text{ref}}$ versus the true wind direction in radians for Meteorological Tower 127, where U_{ref} is a reference "free-stream" wind speed measured outside the simulated boundary layer. A Matlab program was written to automatically perform these interpolations for each turbine location and store the results in a look-up file.

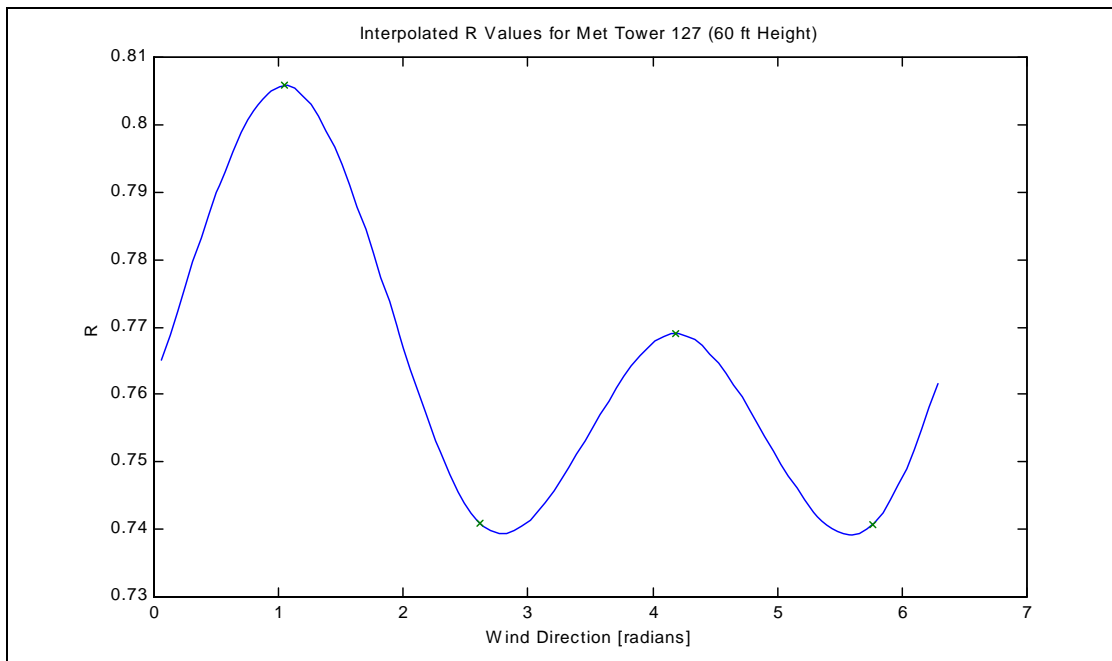


Figure 4-4 Curve fit predicting dimensionless wind speed (R) as a function of wind direction in radians.

Once the wind at each wind turbine site is characterized for all wind directions, the data can be used to predict the wind speed at each turbine site, or collectively for an area, and for a given wind speed and direction associated with a specific met tower. The wind farm operator provides the 30-minute average wind speed and direction values at the met tower, $U_{\text{mettower,full-scale}}(\theta)$, recorded every half hour. Using this information, the full-scale predicted wind speed at the turbine is

$$U_{\text{turb,full-scale}} = \frac{U_{\text{turb,tunnel}}(\theta)}{U_{\text{mettower,tunnel}}(\theta)} U_{\text{met,full-scale}} \quad (4.1)$$

where θ is the wind direction observed at the met tower.

The wind speed at each turbine site is applied to the wind turbine power curve to predict the power produced by each turbine or turbine area. For the Kennetech 56-100 turbines associated with Meteorological Tower 127, the electricity production in kilowatts (E) is described by the following segmented function of the mean wind speed at hub height in meters per second (U):

$$\begin{aligned}
 E &= 0 : U \leq 4.8319 \\
 E &= -0.0224U^3 + 1.8448U^2 - 11.559U + 15.308 : 4.8319 < U < 12.1704 \\
 E &= 107.5 : U \geq 12.1704 \leq U \leq 19.7 \\
 E &= 0 : U > 19.7
 \end{aligned}
 \tag{4.2}$$

This power curve was originally measured by the wind turbine manufacturer, Kennetech, and supplied by Powerworks (EPRI 2003b). Figure 4-5 illustrates the power curve described by Eqn. 4.2.

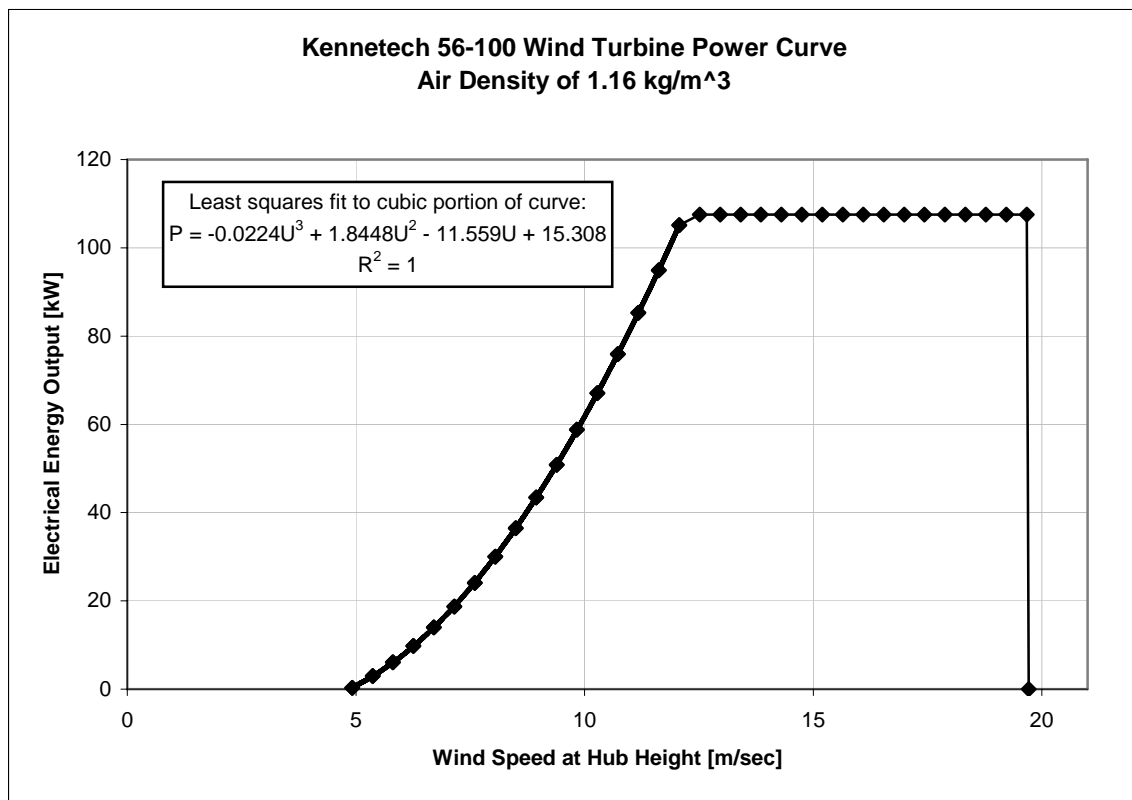


Figure 4-5 Power curve for a Kennetech 56-100 100 kW rated wind turbine. Power curve for a Kennetech 56-100 100 kW-rated wind turbine.

Air density affects the power production, and according to theory, the energy E available in the wind is proportional to air density ρ . Therefore, the predicted energy E from Eqn. 3.2 is adjusted by multiplying by the air density ratio, ρ/ρ_o ,

$$E_i = \frac{\rho}{\rho_o} E \quad (3.3)$$

where ρ is the actual density, as determined primarily by temperature, and ρ_o is the reference density of the power curve. The result E_i is the predicted power production for turbine number i .

Once the energy being produced by each turbine is predicted (E_i), the total power production of the wind farm over a half-hour period is determined by summing over all the turbine locations. The turbines that are offline are accounted for now by correcting the power estimate based on the number of turbines that are offline. This is done at this point, rather than at the individual turbine level, since the online status was recorded for the aggregate of all turbines in each cluster, but not for individual turbines at the Altamont site.

$$(P_{total}) = \sum_{i=1}^N E_i(U) \cdot t_{inc} \cdot \frac{t_{online}}{t_{available}} \quad (4.4)$$

where $t_{inc} = 0.5$ hours, and the ratio $t_{online}/t_{available}$ is the ratio of operating (or online) turbines in the farm over the total number of turbines in the farm. The resulting power prediction P_{total} is an estimate of the power production of the wind farm for a half-hour period and is in units of kWh / ½h.

Programs were written in both Matlab and Perl to perform the prediction scheme outlined above. First a Matlab program generates the interpolated R values for each wind turbine location. The resulting look-up table provides an R value for each turbine for each integer degree of wind direction. Powerworks made available power production, turbine online status, and meteorological tower data for 10 of their Altamont Pass wind turbine clusters, including the Met 127 cluster. The data were provided via FTP from a secure server in the form of ASCII text files, each containing either one day or one month of data for all 10 sites. The data were continuously archived for use in this project since June 26, 2001. Matlab and, later, Perl programs were written to extract data for a desired met tower from a set of these files and store the data in a single text file in comma-separated (CSV) format.

Matlab and Perl programs were then written to read in the interpolated R values and meteorological data and perform the series of calculations described above. The resulting predictions of power production were then compared to the actual power production recorded by Powerworks for the wind turbine cluster.

Atmospheric Stability

The wind tunnel models simulate a neutrally stable atmosphere. However, it has been observed at Altamont Pass that high winds often occur at night under stable conditions. Therefore, it was

expected that the wind tunnel would predict wind power production with greater accuracy during neutral or unstable flow regimes than during stable flow. While the Powerworks meteorological towers did not provide enough data to directly quantify the stability at the wind turbine cluster locations, for example by calculating Richardson numbers or Monin-Obukov lengths, it was still possible to get a first order approximation by observing that at certain times of day and seasons, the flow would, on average, be expected to be stable, while at other times it would be expected to be neutral or unstable. To estimate wind tunnel accuracy, it was decided to compare the relative wind speeds predicted for two meteorological towers for which wind speed data were available from Powerworks. For the 240° wind direction, measurements were taken at two meteorological tower sites, Met 127 and Met 225, roughly 2 km to the east of Met 127. The Met 127 to Met 225 wind speed ratio measured in the wind tunnel was 0.98.

The wind speeds observed at Met 127 and Met 225 were compared for the period between July 1, 2001, and June 30, 2002. It was observed that the median wind speeds were 6.84 m/s (15.3 mph) at Met 127 and 6.35 m/s (14.2 mph) at Met 225. The average ratio of Met 127/Met 225 wind speed ratio for the one year period was 1.19, with a standard deviation of 0.36, indicating that Met 127 generally experiences stronger winds than Met 225, even though the wind tunnel predicted that the wind speeds should be nearly equal.

It is believed that this variation is due to the neutral stability conditions in the wind tunnel during all measurements, while actual conditions exhibit varying degrees of stable flow in the Altamont Pass. Table 4-1 presents the average wind speed ratios observed for different seasons and for different three-hour time intervals. It is not surprising that the wind tunnel prediction of 0.98 is very close to the observed ratio between the hours of 15:00 to 18:00 local time, corresponding to hours 15 through 17 in Table 4-1 during spring and summer. At these times, strong solar heating of the surface can be expected to produce locally unstable conditions much of the time. Conversely, larger discrepancies are observed during night periods, and the fall and winter seasons, when cool surface conditions can be expected to produce stable flows most of the time.

Error Assessment of Prediction Scheme

Cheng (2002) performed a sensitivity analysis to determine the effect of wind speed on power production, using the power curve defined in Eqn. 4.2. An arbitrary mean wind speed of 10 m/s

Table 4-1 Average Met 127/Met 225 wind speed ratio for different seasons and times of day. (Winter is Dec., Jan., and Feb., spring is Mar., Apr., and May, and so on.) Wind tunnel prediction of average wind speed ratio for neutral conditions was 0.98.

Hours	Winter	Spring	Summer	Fall
0-2	1.25	1.18	1.35	1.23
3-5	1.30	1.17	1.28	1.22
6-8	1.22	1.14	1.21	1.24
9-11	1.19	1.08	1.18	1.15
12-14	1.18	1.08	1.13	1.12
15-17	1.31	1.06	1.07	1.17
18-20	1.27	1.11	1.14	1.30
21-23	1.17	1.19	1.30	1.22

was selected for the energy production comparison. For the first comparison group, a change in the mean wind speed of ± 0.1 m/s produced a change of in energy variation was $\pm 15\%$. Finally, at ± 1 m/s difference of wind speed, energy production varied by $\pm 30\%$. This analysis indicates that even with a fairly accurate wind speed estimate, the predicted power generation can vary significantly due to small uncertainty in wind speeds, since power is related to wind speed cubed.

The uncertainty in the final estimate of electrical energy production from a single turbine can be estimated by propagating the uncertainties of the input variables through Eqns. 4.1, 4.2, and 4.3. This analysis was performed using an Excel spreadsheet. The input variables this prediction scheme are two wind tunnel measurements, $U_{\text{turb,tunnel}}(\theta)$ and $U_{\text{met,tunnel}}(\theta)$, and the recorded wind speed at the meteorological tower $U_{\text{mettower,full-scale}}(\theta)$, all of which enter Eqn. 4.1.

For analysis purposes, independence of error between $U_{\text{turb,tunnel}}(\theta)$ and $U_{\text{met,tunnel}}(\theta)$ could not be assumed, however, uncertainty in $U_{\text{mettower,full-scale}}(\theta)$ was taken to be independent of the two wind tunnel measurements. Therefore, the uncertainties of the two wind tunnel measurements were summed, and the result added in a quadrature to predict the estimated percent uncertainty of the predicted wind speed at hub height $U_{\text{turb,full-scale}}$. This uncertainty then was propagated through Eqn. 4.2 and then through Eqn. 3.3, adding in quadrature the uncertainty of ρ and E from Eqn. 4.2. Uncertainty discussed here refers to " \pm " uncertainty. That is, a 10% uncertainty in the value of 5 would be $5 \pm 10\%$ or 5 ± 0.5 .

It became apparent that the power curve itself is a fairly significant potential error source. The third order polynomial in U causes any uncertainty in U to be magnified in the resulting predicted power. Generally, the uncertainty (expressed as percentage) of the result of the power curve was four times the percentage uncertainty of the input wind speed.

Uncertainty also varied with the uncertainty of the input R values, and the input met tower wind speed. Table 4-2 summarizes the resulting uncertainties of the power production predicted by the power curve (Eqn. 4.2) for different uncertainty levels of the R values and the wind speed measured at the meteorological tower. The meteorological tower and turbine R values are assumed to exhibit the same uncertainties. It should be noted that this table presents an extreme range of possible uncertainties: uncertainties of zero are unlikely to occur, while R value uncertainties of 0.1 and wind speed uncertainties of 1 m/s are both excessively conservative in practice.

Table 4-2 Percent uncertainty of predicted power production for different uncertainty levels of the R values and met tower wind speeds. Tabulated uncertainties are expressed as a percentage of rated turbine capacity (107.5 kW).

Uncertainty in Met Tower Wind Speed [m/s]	Uncertainty in Wind Tunnel R Values [dimensionless R value]				
	0	0.01	0.02	0.05	0.1
0	0.0	2.2	4.5	11.1	22.1
0.1	1.2	2.5	4.6	11.2	22.1
0.2	2.4	3.3	5.0	11.4	22.2
0.5	5.9	6.3	7.4	12.6	22.9
1	11.9	12.1	12.7	16.2	25.0

The increase in percent uncertainty from the density correction (Eqn. 4.3) was comparatively low (less than 1 percent), mainly because the uncertainty of the measured pressure is relatively low, the density correction is proportional to pressure, and hence the density correction results in only a small change in the predicted power production.

There are additional sources of error, including the error inherent in the power curve itself. In the calculations above, it was assumed that the power curve introduces error only due to the propagation of the wind speed uncertainty through the power curve. Lange and Waldl (2001) report that the uncertainty of the power prediction from a power curve is proportional to the first derivative of the power curve. This means that for intermediate wind speeds, where the power production changes rapidly with wind speed, some additional error could be expected due to uncertainty in the power curve itself. Additionally, Eqn. 4.2 describes a new turbine, while those at the Altamont site were installed over 20 years ago. Although the change in the power curve over time is difficult to estimate, it is also a source of potential uncertainty.

Error Levels of Power Production Prediction Schemes: July 1, 2001 – June 30, 2003

Four different power production prediction schemes were compared for the period between July 1, 2001 and June 30, 2003. A dataset comprised of data from all 11 of the Powerworks meteorological towers was assembled that included mean and maximum wind speeds, and means and standard deviations of wind directions, as well as the power generated by the associated turbine cluster, corrected to 100% turbine availability. The dataset also included the temperature and humidity recorded at Meteorological Tower 438, pressure from the LLNL Site 300 meteorological tower, and an air density calculated from these parameters using the ideal gas law

All data observations were recorded at half-hour intervals, resulting in 48 observations per day, and a total of 35,040 observations over the two-year period. Observed wind speed and direction are 30-minute averages. Observations for which all data were not available were removed from the dataset, resulting in a final dataset containing 31,035 observations.

As discussed earlier, during this period, some of the wind direction data are believed to be unreliable. Since it is not possible to verify the wind direction data, two datasets were used in the analysis. The first contained all of the observations "as is," while the second excluded 185 days of data judged to have unreliable wind direction data.

Four prediction schemes were considered:

First, a scheme was implemented that used the measured Met 127 wind speed only and the wind tunnel measurements for the 240° wind direction to estimate the power production of the wind turbines associated with Met 127. This method replicated the prediction scheme used by Cheng (2002).

The second scheme used the wind tunnel measurements for all four wind directions. The Met 127 wind speed and direction were used as inputs. The details of the scheme are outlined above, except that no density correction was made (Eqn. 4.3).

The third and fourth schemes applied Eqn. 3.3 to the second scheme to correct for air density. For the third scheme, $\rho_o = 1.16 \text{ kg/m}^3$, while for the fourth scheme, $\rho_o = 1.20 \text{ kg/m}^3$.

The dataset was analyzed using statistical analysis software (Intercooled Stata 7.0, Stata Corporation). Tables 4-3 and 4-4 summarize the results of the statistical analysis for a variety of cases. The observed Met 127 wind direction remained essentially constant at times, indicating a stuck vane, for periods ranging from a few hours to several months over the two years of data collection. Since these data would introduce artificial error into the direction-dependent prediction schemes, the statistical analysis was repeated after removing approximately 185 days of observations with unreliable wind direction data from the dataset. Tables 4-5 and 4-6 present the results.

Table 4-3 Uncertainty levels observed for each power production prediction scheme and for all conditions, day and night conditions, and conditions corresponding to each Pasquill-Gifford stability class observed at the LLNL mast. Uncertainties expressed as mean errors (ME) and mean absolute errors (MAE) of the predictions.

Prediction Type	Total	Day	Night	PG Stability Class A	PG Stability Class B	PG Stability Class C	PG Stability Class D	PG Stability Class E	PG Stability Class F
ME 240 Degrees Data Only	142	64	227	1	41	3	178	207	213
ME All Directions	86	7	171	-8	1	-54	105	164	164
ME All Directions w/ 1.16 kg/m ³ Ref. Dens.	88	4	179	-9	-4	-61	111	174	167
ME All Directions w/ 1.20 kg/m ³ Ref. Dens.	49	-34	139	-12	-28	-98	53	135	148
MAE 240 Degrees Data Only	277	236	323	33	144	203	380	273	243
MAE All Directions	267	238	297	29	144	211	374	250	210
MAE All Directions w/ 1.16 kg/m ³ Ref. Dens.	271	244	300	29	147	218	379	256	211
MAE All Directions w/ 1.20 kg/m ³ Ref. Dens.	272	256	290	30	154	235	387	239	198
Number of Observations	31035	16179	14856	163	3805	5115	11359	4120	6473

Table 4-4 Uncertainty levels observed for each power production prediction scheme for different wind directions and actual power production levels. Uncertainties expressed as mean errors (ME) and mean absolute errors (MAE) of the predictions.

Prediction Type	Total	1000 kW < Actual Power < 4000 kW				1000 kW < Actual Power < 4000 kW								
		Actual Power >= 4000 kW	Actual Power < 4000 kW	Actual Power <= 1000 kW		Wind Direction Between 335 and 45 Degrees	Wind Direction Between 45 and 135 Degrees	Wind Direction Between 135 and 225 Degrees	Wind Direction Between 225 and 315 Degree	Wind Direction Between 315 and 45 Degrees	Wind Direction Between 45 and 135 Degrees	Wind Direction Between 135 and 225 Degree	Wind Direction Between 225 and 315 Degree	Wind Direction Between 335 and 45 Degrees
ME 240 Degrees Data Only	142	177.84	154	-12.76	136	191	89	109	129	142	300	209		
ME All Directions	86	141.7	21	-24.78	126	99	26	38	112	-46	-17	-60		
ME All Directions w/ 1.16 kg/m ³ Ref. Dens.	88	144.23	29	-32.73	121	107	33	42	104	-28	25	-42		
ME All Directions w/ 1.20 kg/m ³ Ref. Dens.	49	135.89	-46	-132.3	60	70	21	17	23	-97	-43	-118		
MAE 240 Degrees Data Only	277	213.28	485	185.37	329	324	172	190	463	480	715	502		
MAE All Directions	267	189.49	494	193.35	325	306	157	181	461	488	711	539		
MAE All Directions w/ 1.16 kg/m ³ Ref. Dens.	271	191.48	501	201.54	332	309	158	184	471	494	709	546		
MAE All Directions w/ 1.20 kg/m ³ Ref. Dens.	272	185.71	493	245.27	335	310	156	186	449	496	703	554		
Number of Observations	31035	18428	7807	4800	10350	9842	2533	8370	3393	2816	293	1323		

Table 4-5 Uncertainty levels observed for each prediction scheme considering only data with wind directions considered reliable, for all conditions, day and night conditions, and conditions corresponding to each Pasquill-Gifford stability class observed at the LLNL mast. Uncertainties expressed as mean errors (ME) and mean absolute errors (MAE) of the predictions.

Prediction Type	Total			PG Stability Class A	PG Stability Class B	PG Stability Class C	PG Stability Class D	PG Stability Class E	PG Stability Class F
		Day	Night						
ME 240 Degrees Data Only	150	84	215	21	65	25	192	193	187
ME All Directions	121	52	187	12	42	-7	152	172	165
ME All Directions w/ 1.16 kg/m ³ Ref. Dens.	122	49	193	10	37	-14	157	179	166
ME All Directions w/ 1.20 kg/m ³ Ref. Dens.	88	16	158	6	17	-46	105	145	150
MAE 240 Degrees Data Only	264	231	296	40	143	195	380	247	215
MAE All Directions	250	221	279	37	134	186	365	232	199
MAE All Directions w/ 1.16 kg/m ³ Ref. Dens.	255	227	282	37	136	193	371	237	199
MAE All Directions w/ 1.20 kg/m ³ Ref. Dens.	252	233	271	38	138	204	374	222	187
Number of Observations	22115	10907	11208	49	2432	3495	7503	3238	5398

Table 4-6 Uncertainty levels observed in each prediction scheme for different wind directions and actual power production levels. Analysis includes only observations for which wind direction measurement was considered reliable. Mean errors (ME) and mean absolute errors (MAE) are given.

Prediction Type	Total	Actual Power >= 4000 kW				Actual Power <= 1000 kW							
		1000 kW < Actual Power < 4000 kW	Actual Power >= 4000 kW	1000 kW < Actual Power < 4000 kW	Actual Power >= 4000 kW	Wind Direction Between 225 and 315 Degree	Wind Direction Between 135 and 225 Degree	Wind Direction Between 45 and 135 Degrees	Wind Direction Between 335 and 45 Degrees	Wind Direction Between 225 and 315 Degree	Wind Direction Between 135 and 225 Degree	Wind Direction Between 45 and 135 Degrees	Wind Direction Between 335 and 45 Degrees
ME 240 Degrees Data Only	150	174.39	163	-12.61	155	201	45	110	153	120	175	1081	
ME All Directions	121	148.5	107	-15.18	144	151	16	79	136	27	-67	863	
ME All Directions w/ 1.16 kg/m ³ Ref. Dens.	122	151.13	109	-24.52	141	155	19	81	132	36	-32	883	
ME All Directions w/ 1.20 kg/m ³ Ref. Dens.	88	143.32	32	-128.4	86	119	14	77	51	-36	-91	811	
MAE 240 Degrees Data Only	264	207.04	497	178.86	324	329	114	133	469	475	761	1253	
MAE All Directions	250	187.35	493	181.23	318	312	104	109	465	480	752	1107	
MAE All Directions w/ 1.16 kg/m ³ Ref. Dens.	255	189.54	503	188.94	324	317	105	111	475	491	750	1122	
MAE All Directions w/ 1.20 kg/m ³ Ref. Dens.	252	183.57	486	230.96	321	316	103	107	449	489	743	1066	
Number of Observations	22115	14902	4619	2594	8125	7088	1885	5017	2573	1836	95	115	

In general, the schemes that incorporate the wind direction in the prediction show smaller magnitudes of mean error, indicating less bias error, than the 240° direction prediction. Levels of mean absolute error do not show a significant reduction vs. the 240° prediction until the observations with suspect wind direction measurements are removed. Even then, the MAE values show only a slight improvement (on the order of 10%) relative to the 240° prediction.

It should be noted that the Altamont Pass most commonly experiences winds from approximately 240°, and almost all of the strong winds that produce significant power come from this direction. This means that the 240° prediction scheme and the schemes using all of the direction data use essentially the same R values and therefore predict almost identical power production. During the two-year test period, the wind direction was in the range 220° to 260° 42% of the time overall and 78% of the time when the wind speed was exceeded 10 m/s.

Table 4-6 illustrates another interesting result in the right-most column., Significant mean error or bias (ME) occurred in the few instances when the wind direction was from the north (between 335° and 45°) and generated moderate power (between 1000 and 4000 kWh/0.5h) relative to when the wind direction was in the other quadrants. It is believed the reduced power output occurred because the wind direction was roughly parallel to the rows of turbines along the ridgelines. At these times, wake effects of the turbines become significant, as the turbines are spaced only a few rotor diameters apart along the ridges. Also, to reduce turbine wear while maximizing power production, the wind farm operator often shuts down every other turbine on the ridgelines; this may also account for the significant overprediction in this case.

Error Bias

Tables 4-5 and 4-6 suggest that applying the density correction (Eqn. 4.3) does significantly reduce ME or MAE. Also, it was noted that the maximum power production predicted by either the 240° only scheme or the all directions scheme, is 4676.25 kWh/0.5h (87 turbines × 107.5 kWh/0.5h/turbine). However, an analysis of the actual power production showed that this level was exceeded 7.5% of the time. For the period July 2001 to June 2003, the 92.5 percentile power production was 4677 kWh/0.5h, the 95th percentile was 4795 kWh/0.5h, and the 99.9th percentile was 4954 kWh/0.5h. This suggests that the prediction schemes underpredict the power production, perhaps because there could be a few additional turbines in the cluster than were modeled, or the power curve could be slightly wrong.

However, Tables 4-3 through 4-6 show that almost all of the ME values are positive, which indicates a bias towards overprediction of power. The ME is negative only when the power production exceeded 4000 kWh/0.5h, and it is strongly positive when power production was less than 4000 kWh/0.5h. Therefore, while it is tempting to simply add a scaling factor to slightly increase all of the power production estimates by say a factor of 4950/4676.25, this would also be expected to increase the ME and MAE at times of mid- and low-power production.

The data file supplied by Powerworks Inc. includes 93 turbines in the Met 127 cluster, but the wind tunnel records indicate only 87 turbines were modeled. The turbines not modeled are numbered 6, 7, 8, 9, 10, and 100. Adding these turbines increases the maximum possible predicted power to (93 turbines × 107.5 kWh/0.5h/turbine) 4998.75 kWh/0.5h. Since all but one of the missing turbines is located near the edge of the modeled area, the best that can be done is to adjust the results by multiplying by the factor 93/87.

Tables 4-7 and 4-8 show the error levels after applying this correction. The most significant result is that, in every case, the mean prediction is higher than the mean observed power production. Additionally, the schemes that use all directions of wind data tend to show some improvement in both ME and MAE relative to the 240° data case.

Atmospheric Stability

Table 4-7 illustrates the impact of atmospheric stability on the accuracy of the prediction schemes and the power production of the turbines in the Met 127 cluster. The results support previous research that indicated power production in the Altamont Pass is greatest at night and under stable conditions (Pasquill-Gifford classes D, E and F) and also show that power production varies with stability class.

For example, the most unstable Class A occurred infrequently (49 of 22,115 observations), and power production never exceeded about one-quarter of the wind farm capacity.

At the other extreme, the most stable Class F conditions occurred about 25% of the time (5,098 of 22,115 observations), but high power production also did not occur, perhaps because very high stability is generally associated with low wind speeds.

Table 4-7 Mean and mean absolute errors of power production prediction schemes, excluding data points with unreliable wind directions and increasing predicted power production by a factor of 93/87 to account for unmodeled turbines. Errors are reported for overall data, as well as those observed for day and night and each Pasquill-Gifford stability class observed at the LLNL mast. Percentile values are observed Met 127 power production corrected to 100% turbine availability.

Prediction Type	Total	Day	Night	PG Stability Class A	PG Stability Class B	PG Stability Class C	PG Stability Class D	PG Stability Class E	PG Stability Class F
ME 240 Degrees Data Only	236	162	309	29	110	100	332	282	223
ME All Directions	205	129	279	19	86	66	289	259	200
ME All Directions w/ 1.16 kg/m ³ Ref. Dens.	206	125	285	17	80	59	294	267	201
ME All Directions w/ 1.20 kg/m ³ Ref. Dens.	170	90	248	13	59	24	239	231	184
MAE 240 Degrees Data Only	309	260	355	43	163	214	443	313	248
MAE All Directions	290	246	334	38	149	200	422	295	229
MAE All Directions w/ 1.16 kg/m ³ Ref. Dens.	293	247	338	37	148	202	426	301	230
MAE All Directions w/ 1.20 kg/m ³ Ref. Dens.	271	234	308	37	140	193	393	271	215
Number of Observations	22115	10907	11208	49	2432	3495	7503	3238	5398
Mean Actual Power Production	1099	1052	1145	90	592	1065	1833	1093	343
Standard Deviation Actual Power Production	1628	1567	1684	201	1154	1528	1903	1650	796
25% Percentile Met 127 Power (kWh/0.5h)	0	0	0	0	0	0	0	0	0
50% Percentile Met 127 Power (kWh/0.5h)	24	27	19	0	0	111	1103	0	0
75% Percentile Met 127 Power (kWh/0.5h)	1869	1755	2013	61	572	1771	3849	2117	172
90% Percentile Met 127 Power (kWh/0.5h)	4240	4015	4412	380	2508	3877	4772	4202	1238
95% Percentile Met 127 Power (kWh/0.5h)	4742	4616	4795	661	3573	4574	4856	4649	2294
99% Percentile Met 127 Power (kWh/0.5h)	4897	4867	4908	900	4594	4869	4917	4871	3939

Although predicted power production varies with atmospheric stability as well as wind speed, efforts to develop a correction factor based on stability class were not successful.

Predictions Of Zero Power Production

It should be noted that, for many hours of the year, the wind speed at Altamont Pass is very low, and the turbines do not operate at all, especially during the fall and winter months. Since the power production prediction schemes predict non-zero power production only when the Met 127 wind speed is greater than about 4.78 m/s, they yield "perfect predictions" of zero power production at low wind speeds. A large number of perfect zero-power predictions can reduce the magnitude of both ME and MAE. While it is true that these are valid predictions, it also leaves the impression that the power predictions at higher wind speeds are more accurate than they really are.

Table 4-10 categorizes the number of observations during the two-year data collection period according to whether the power production was non-zero and whether the observed wind speed at Met 127 resulted in a prediction of non-zero power production. The total number of observations in the dataset is 22,115, the sum of the four categories.

Table 4-8 Mean and mean absolute errors (ME and MAE) of each power production prediction scheme vs. wind direction and actual power production level, excluding observations with unreliable wind direction measurements. For all schemes, predicted power production is multiplied by a factor of 93/87 to account for unmodeled turbines.

Prediction Type	Total	Actual Power		1000 kW < Actual Power < 4000 kW				1000 kW < Actual Power < 4000 kW				
		Actual Power <= 1000 kW	Actual Power >= 4000 kW	Wind Direction Between 225 and 315 Degree	Wind Direction Between 135 and 225 Degree	Wind Direction Between 45 and 135 Degree	Wind Direction Between 335 and 45 Degree	Wind Direction Between 225 and 315 Degree	Wind Direction Between 135 and 225 Degree	Wind Direction Between 45 and 135 Degree	Wind Direction Between 335 and 45 Degree	
ME 240 Degrees Data Only	236	193	338	304	297	295	58	123	333	286	319	1260
ME All Directions	205	166	277	301	285	242	27	89	315	188	61	1027
ME All Directions w/ 1.16 kg/m ³ Ref. Dens.	206	168	280	291	282	246	31	92	311	197	99	1049
ME All Directions w/ 1.20 kg/m ³ Ref. Dens.	170	160	197	180	223	207	25	87	224	120	36	972
MAE 240 Degrees Data Only	309	223	581	315	391	380	123	144	564	540	853	1408
MAE All Directions	290	201	565	316	384	354	109	117	556	522	784	1239
MAE All Directions w/ 1.16 kg/m ³ Ref. Dens.	293	203	574	309	386	359	111	119	563	535	794	1256
MAE All Directions w/ 1.20 kg/m ³ Ref. Dens.	271	197	539	223	348	337	108	115	518	514	771	1195
Number of Observations	22115	14902	4619	2594	8125	7088	1885	5017	2573	1836	95	115

Table 4-9 Number of observations at Met 127 turbine cluster, categorized by whether the predicted and actual power production levels are zero or non-zero.

	Met 127 Power Production = 0	Met 127 Power Production > 0
Predicted Power (All, No Dens. Cor.) = 0	7109	342
Predicted Power (All, No Dens. Cor.) > 0	3385	11279

The predicted power was generated using all observations and corrected for the missing six turbines by a factor of 93/87. No density correction was applied.

As already mentioned, a significant portion of the Met 127 wind direction data are suspect, and the anemometer may also give erroneous readings. Table 4-11 shows the number of non-zero power production observations recorded for low wind speeds, in some cases, less than 1 m/s. While in most cases, power production was zero at low wind speed. Table 4-11 indicates there are instances of significant power production at low observed wind speed at Met 127. This is unexpected because the power curve for the Kennetech 100 turbines (Eqn. 4.2) indicates the cut-in wind speed is 4.83 m/s, and no power generation should occur at lower wind speeds. This suggests that either there is significant uncertainty in the recorded wind speed data at times, or the wind speed is even more variable across the site than the wind tunnel predicts.

Table 4-10 Number of observations of Met 127 power production for several criteria of Met 127 recorded wind speed. Mean values, standard deviation and minimum and maximum values are reported for each set of observations. For the two year period considered, the total number of observations was 22,115.

Wind Speed	Observations of Non-Zero Power Prod.	Mean kWh/0.5h	Std. Dev. kWh/0.5h	Min. kWh/0.5h	Max. kWh/0.5h
< 5 m/s	8607	9.5	71.8	0	2834.9
< 4 m/s	6016	4.8	66.6	0	2834.9
< 3 m/s	3459	2.4	43.5	0	2079.8
< 2 m/s	1353	1.2	20.9	0	496.3
< 1 m/s	156	5.0	35.7	0	325.8

It is interesting to note that almost all of the extreme cases of non-zero power production and low reported wind speed occur during January through March. There are no cases of non-zero power production at wind speeds less than 2 m/s and temperatures at or below 0 degrees C or 273 degrees K. However, there are 10 observations of significant non-zero power production when wind speed is less than 2 m/s, all but one of them at temperatures less than 10 degrees C above freezing. The five observations above 100 kWh/0.5h production occurred on two days during January, suggesting a phenomenon associated with near-freezing temperatures, such as frost buildup, or an increase in bearing or lubricant friction in the anemometer.

Characteristics of the Error in the Prediction Schemes

There are many possible sources of error that could account for the ME and MAE error levels reported in Tables 4-7 and 4-8. Atmospheric stability and other meteorological variations are expected to contribute significantly. The power curve (Eqn. 4.2), supplied by the manufacturer, represents the power production of a new turbine under optimum conditions, while the turbines at Altamont are not new and may have experienced significant wear and tear. Another potential source of error is the possibility that bearing wear, siting, or other factors cause the anemometers to underreport wind speed.

To develop a correction factor equation to eliminate some of the remaining error, backward selection multiple linear regression was applied to 42 potential predictors, including the predicted power using data for all wind directions and the 1.16 kg/m^3 density correction from the historical dataset for July 2001 to June 2003. Observations with missing predictors were excluded, but those with suspected bad wind direction data for Met 127 were included.

The resulting regression equations predict two variables, the actual power production at Met 127 and the error in the power production vs. the actual power production. The "improved" power prediction is generated by adding the error predicted by the second multiple linear regression equation to the power predicted by the wind tunnel scheme. The predictions of both equations were disappointing, and the MAE values were slightly higher using four months of test data (July 2003 to October 2003) when the equations were applied relative to the MAEs for the "unimproved" output of the wind tunnel prediction scheme.

It appears that the reason the regression-based predictive equations fared so poorly is that the equations did not account for all variables. That is, the correlation appears to be poor between the magnitude of the error and the power production, or any other predictive variable, such as wind speeds, temperatures, or stability class. The power production relative to measured wind speed appears to be an inherently "noisy system."

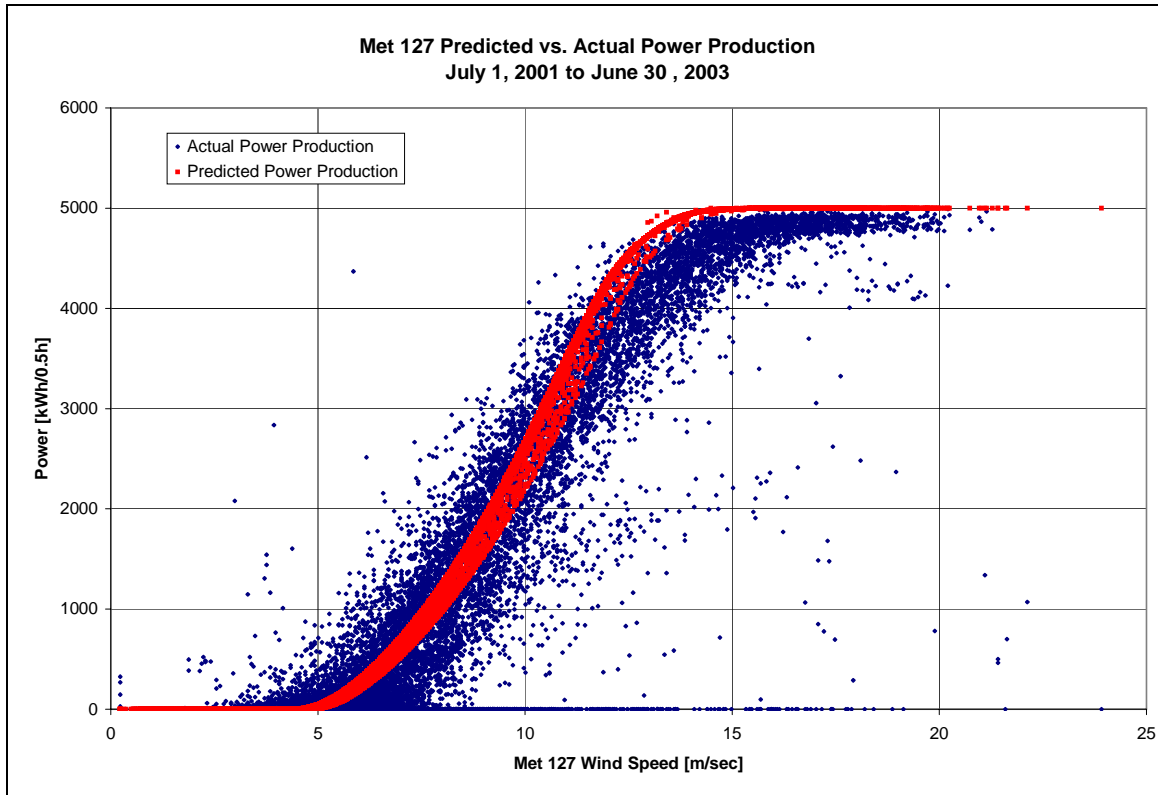


Figure 4-6 Predicted versus actual power production for the Met 127 turbine cluster between July 1, 2001, and June 30, 2003.

Comparison of Predictions with Varying Input Wind Speeds

One possible source of error that would affect prediction accuracy is an error bias in the wind speed reported by the Met 127 anemometer. As the anemometer ages, bearing deterioration would, for example, decrease the rotation speed at a given wind speed, therefore causing it to underreport the wind speed. It is known that this anemometer has not been routinely serviced during the time of this study. To determine if this could be occurring, the Perl script used to predict the power as outlined above was adjusted to predict all four of the schemes, but at several different wind speeds. In addition to a "baseline" prediction using the actual reported wind speed, additional predictions were generated for each of five adjustments to the measured wind speed, including -1.0 m/s, -0.5 m/s, +0.5 m/s, +1.0 m/s. This has the effect of shifting the power vs. wind speed curve to the right or left.

Table 4-12 summarizes the results of the predictions using the five wind speed corrections (-1, -0.5, 0, +0.5, +1 m/s). It is interesting to note that reducing the input wind speed to simulate a

"worn out" anemometer that underreports the true wind speed increased both ME and MAE, suggesting that the anemometer is not, in fact, underreporting wind speed. The shift of ME values from positive to negative between a correction factors of -0.5 m/s and -1.0 m/s suggests the prediction error reaches an overall minimum within this range.

Table 4-11 ME and MAE for power production schemes after adjusting the input wind speed by the specified amounts.

Units: kWh/0.5h	Input Wind Speed Correction				
	-1.0 m/s	-0.5 m/s	No Change	+0.5 m/s	+1.0 m/s
ME 240	-14	106	236	379	533
ME All	-37	79	205	341	489
ME All w/ 1.16 Ref. Dens.	-35	80	206	342	491
ME All w/ 1.20 Ref. Dens.	-64	48	170	303	447
MAE 240	261	261	309	407	545
MAE All	261	254	290	377	505
MAE All w/ 1.16 Ref Dens.	264	257	293	379	506
MAE All w/ 1.20 Ref Dens.	261	245	271	347	466

These results suggest that the anemometer may overreport the wind speed by 0.5 to 1.0 m/s. Of course, it should be noted that other factors also may influence the final accuracy of the predictions.

For the prediction scheme using all wind directions but without a density correction, the -0.5 m/s correction also seems to give the best results in the intermediate power production range between 1000 and 4000 kWh/0.5h. The ME and MAE for the -0.5 m/s correction in this range are -59.6 kWh/0.5h and 543.1 kWh/0.5h, respectively. For the -1.0 m/s correction, the corresponding results are -387.4 kWh/0.5h and 650.8 kWh/0.5h. The results for the uncorrected ("No Change") prediction were 276.7 kWh/0.5h and 5645 kWh/0.5h, respectively.

Optimum Prediction Scheme for Met 127

Based on the above results, the recommended configuration of the power production prediction scheme for operational use is:

- All-wind-direction input data.
- Density correction based on 1.20 kg/m^3 reference density.
- Input wind speeds based on the reported values minus 0.5 m/s.
- Resulting predicted power production multiplied by a factor of 91/87 to account for the six missing turbines and an apparent slight optimism in the power curve regarding the maximum power production of a turbine.

Table 4-12 presents the resulting ME and MAE values for the recommended prediction scheme and several others. It is believed that, if a more accurate power curve was available, the error could be reduced further. In addition, it appears that the power curve used applies to a new turbine and may no longer represent the performance of the aging turbines at the site.

Table 4-12 ME and MAE for recommended and four other power production prediction schemes, based on Met 127 observations between July 1, 2001, and June 30, 2003, excluding observations with missing data or unreliable Met 127 wind direction data. Units of ME and MAE are kWh/0.5h.

Directions of Wind-Tunnel Data Used	240 degrees	All	All	All	All
Correction Offset For Input Wind Speed	None	None	None	-0.5 m/sec	-0.5 m/sec
Density Correction	None	None	Ref.: 1.20 kg/m ³	Ref.: 1.20 kg/m ³	Ref.: 1.20 kg/m ³
Final Prediction Multiplier	93/87	93/87	93/87	93/87	91/87
ME	236	205	170	48	23
ME: Actual Power Production < 1000 kWh/0.5	193	166	160	91	87
ME: Actual Power Production 1000 - 4000 kWh/0.5	338	277	197	-128	-176
ME: Actual Power Production >= 4000 kWh/0.5	304	301	180	113	12
MAE	309	290	271	245	241
MAE: Actual Power Production < 1000 kWh/0.5	222	201	197	158	155
MAE: Actual Power Production 1000 - 4000 kWh/0.5	581	565	539	548	548
MAE: Actual Power Production >= 4000 kWh/0.5	315	316	223	206	183

Predicting Power Using A Statistically-Derived Equation

Multiple linear regression (MLR) was applied to derive an equation to predict the power production of the case study wind farm using the wind speed at the wind farm meteorological tower anemometer and the date and time as input data. For use in a forecasting system, the wind speed at the meteorological tower anemometer would have to be forecast first. A common statistical approach is to predict meteorological conditions at a specific location based on other measured data using multiple linear regression to generate a predictive equation for each predictand or measurement to be predicted. The method iteratively chooses from the potential predictors to minimize the number of predictors while maximizing accuracy. Wilks (1995) gives a good description of the statistical processes that were used.

It was desired to develop and evaluate the accuracy of a purely statistical approach to predicting the power production of the Altamont Pass wind turbine clusters. Statistical prediction offers several advantages over wind tunnel or CFD-based methods. Statistical prediction is generally computationally efficient. McCarthy (1997) generated equations to forecast next-day Altamont Pass daily average wind speeds that were programmed into a pocket calculator. Another important advantage is that statistical methods can automatically account for inaccuracies in the data that introduce errors into physics-based prediction methods, for example when an anemometer underreports the wind speed.

Screening MLR was used to generate an equation to predict the power production of the case study wind farm. Two years of historical wind speed vs. time data at the meteorological tower during the period July 1, 2001, to June 30, 2003, were used to generate a dataset with 13 potential predictor variables, including the logarithm and square root of the wind speed, wind speed to the first, second and third power, and sine and cosine functions with periods of half day, one day, and one year. Wind direction was not included in this equation (or used in the following “median-based” power curve) because the wind vane was apparently stuck in a single position for periods ranging from hours to months. In addition, within the two-year dataset, during some times of the year, the wind direction data are considered unreliable.

Screening MLR analysis eliminated the least important potential predictors and yielded the following regression equation to predict power P , a percentage of the observed wind farm capacity

$$P = -11.8278U + 2.281434U^2 - 0.07626U^3 - 7.74768A - 4.59537 \cos(2\pi Y) + 17.50517 \quad (4.6)$$

where U is the wind speed at the meteorological tower in m/sec; $A = 1$ if U is greater than the cut-in wind speed of the turbine, or $A = 0$ otherwise, and Y is the time of the year in decimal form (i.e., $Y = 0$ at time 0:00 on Jan. 1, $Y = 0$, and $Y = 1$ at time 23:59 on Dec. 31).

Power Curve Based on Curve Fitting Historical Data

If historical power production information is available for a wind farm, it also is possible to generate a wind farm power curve by performing a best fit to the power production as a function of wind speed.

For the case study wind farm, a power curve was generated using two years of power production data for the period, July 2001 to June 2003). Using the "histogram" method, each observation was grouped by wind speed in bins covering 1-m/s wind speed increments, i.e., the first bin interval was 0 to 1 m/s, the second was 1 to 2 m/s, and so on. For each wind speed bin, the median power production was assumed to be the power produced at the bin wind speed. Median values were used instead of mean values to reduce the effects of outlying data points on the curve fit. Figure 4-8 presents the resulting power curve.

Power Curve Based On Numerical Simulation

The ABLWT power curve prediction method has the significant advantage of not requiring an historical dataset to implement it. However, it does require the time-consuming tasks of constructing terrain models and taking measurements in an ABLWT. A method of deriving a power curve quickly, using neither historical data nor a wind-tunnel facility would be very useful. The approach of using the "speed-up" prediction methods discussed previously does not appear likely to provide the accuracy needed. One difficulty of the methods of Weng et al., Lemelin et al, and others is that the hill height and horizontal length scale must be estimated. Additionally, the effect of upwind terrain is not included in the speed-up estimate. In complex terrain, hills blend into each other, making it difficult to characterize the hill in terms of h and L_1 . Writing a program to estimate h and L_1 for large numbers of sites in complex terrain would be enormously challenging.

The analytical method of Jackson and Hunt is based on matching a potential flow solution to a viscous solution near the hill surface. Although intended only for smoothly varying hills of moderate slope, it has been reported to be surprisingly accurate for steeper terrain. It was postulated that perhaps a numerical model simulating potential flow above a transect of the terrain surrounding the hill and aligned with the wind direction could provide useful information.

A potential flow is much easier to solve than a viscous, turbulent flow, and solutions would require far less computational effort. A numerical model would have the additional advantage of not requiring "trained eye" intervention to estimate any parameters and would therefore lend itself to a fully automated computational process.

Two-Dimensional Potential Flow Simulation

Potential flow methods are used to simulate steady, inviscid, non-accelerating flows. Using the stream function ψ , the governing equation of the flow reduces to Laplace's equation $\nabla^2\psi=0$. In two dimensions, the equation is:

$$\frac{\partial^2\psi}{\partial x^2} + \frac{\partial^2\psi}{\partial y^2} = 0 \quad (4.7)$$

When this is solved with appropriate boundary conditions, lines of constant ψ represent streamlines. The flow velocity is greatest in regions where the streamlines are close together and lowest when they are far apart. The velocity components U and V are calculated from the gradients of ψ

$$U = \frac{\partial\psi}{\partial y} \quad V = -\frac{\partial\psi}{\partial x} \quad (4.8)$$

Laplace's equation can be solved using a finite difference formulation of the equation, by solving the resulting set of equations iteratively or using matrix inversion. As the number of grid points in the finite difference method increases, iterative methods are often less computationally intensive.

The traditional method of discretizing Laplace's equation generates an equation for $\psi(i,j)$ based on ψ at the four surrounding points. Using a Taylor series expansion in each direction, the second derivative of ψ in x is approximated by

$$\left. \frac{\partial^2\psi}{\partial x^2} \right|_{i,j} \approx \frac{\psi_{i-1,j} - 2\psi_{i,j} + \psi_{i+1,j}}{dx^2} \quad (4.9)$$

The value of $\psi_{i,j}$ can be estimated by substituting this, and a similar expression for the y direction, into Laplace's equation. The result is

$$\psi_{i,j} \approx \frac{\psi_{i-1,j} + \psi_{i+1,j} + \frac{dx^2}{dy^2}(\psi_{i,j-1} + \psi_{i,j+1})}{2\left(1 + \frac{dx^2}{dy^2}\right)} \quad (4.10)$$

This equation is valid for all interior points in the domain. The outer points must be specified as boundary conditions.

A program ("Potential.f90") was written in Fortran 90 to solve this equation over a large domain that incorporated variable terrain elevation along the lower boundary. Terrain was addressed by setting the values in the lower area of the domain to $\psi=0$ when they were at or below ground level. Effectively, the square cell surrounding each grid point was either "all air" or "all terrain." Although the program worked as expected, the flow solutions were not ideal. Use of a uniform grid required that the grid be relatively coarse near the hill to cover a high enough region above the terrain. Combined with the simple terrain boundary condition of setting $\psi=0$, this meant that the streamlines in the solution simulated flow over a "stair-stepped" surface instead of over a smoothly varying hill. Streamlines would be highly compressed near these sharp edges, resulting in localized extremes of velocity near each step. Results near the surface also varied significantly as the grid spacing was changed because the number and location of the steps varied with each grid. An improved solution was required.

After several program iterations, the final version of the program ("Potential10.f90") incorporated multiple refinements. The most significant was that for grid points adjacent to the surface, $\psi_{i,j}$ was approximated using the distance from point (i,j) to the actual surface location, instead of to the next grid point, either (i,j-1), (i-1,j) or (i+1,j). Making this modification turned out to be rather difficult: a new version of Eqn. 4.10 had to be derived that would allow dx and dy to vary, instead of being constants. The Taylor series derivation method quickly resulted in equations that would have been computationally expensive to solve. Therefore, an alternative discretization of Laplace's equation was developed.

The new method is limited to the four surrounding points, the same as the initial method. Solving Laplace's equation at a point requires estimating the second derivatives at that point. If a function is fit between the three points, the second derivatives could be estimated from the fit function. The lowest order polynomial function with non-zero second derivatives is a parabola, which conveniently can be fit between a set of three points. Letting

$$\psi(x) = a + bx + cx^2 \tag{4.11}$$

For this function, $d^2\psi/dx^2 = 2c$.

Assume that $\psi(x)$ is a continuous function. Consider this function at three points: ψ_{i-1} , ψ_i and ψ_{i+1} . These points are at arbitrary locations x_{i-1} , x_i and x_{i+1} respectively along the x axis, and the only constraint is that $x_{i-1} < x_i < x_{i+1}$. Define $dx_{i-1} = x_i - x_{i-1}$ and $dx_i = x_{i+1} - x_i$. Substituting these values into Eqn. 4.11 results in two equations in two unknowns:

$$\psi_{i-1} = \psi_i + bx_{i-1} + cx_{i-1}^2 \quad \psi_{i+1} = \psi_i + bx_{i+1} + cx_{i+1}^2 \tag{4.12}$$

Solving for c gives

$$c = \frac{\frac{\psi_{i+1} - \psi_i}{dx_i} + \frac{\psi_{i-1} - \psi_i}{dx_{i-1}}}{dx_i + dx_{i-1}} \quad (4.13)$$

A similar equation can be derived for the y direction. Both versions of 4.13 are then substituted into Laplace's equation and solved for $\psi_{i,j}$. At this point, a change of variables is introduced. Let $dx_{i-1} = dl$, $dx_i = dr$, $dy_{j-1} = dd$ and $dy_j = du$. The variables dx and dy have already been defined as the grid spacing in x and y . Away from the boundaries, this is also the distance between point (i,j) and its surrounding points. However, to better model the stream function near the surface, the next step will be to introduce "artificial points" on the terrain surface that do not necessarily coincide with the regular grid spacing. Therefore, the variables dl , dr , du , and dd are introduced to define the distance from the point (i,j) to the adjacent points in the left, right, up, and down directions respectively, as shown in Figure 4-7. When these approximations are substituted into Laplace's equation, the result is

$$\psi_{i,j} \approx \frac{\frac{\psi_{i+1,j}}{dr_{i,j}(dr_{i,j} + dl_{i,j})} + \frac{\psi_{i-1,j}}{dl_{i,j}(dr_{i,j} + dl_{i,j})} + \frac{\psi_{i,j+1}}{du_{i,j}(du_{i,j} + dd_{i,j})} + \frac{\psi_{i,j-1}}{dd_{i,j}(du_{i,j} + dd_{i,j})}}{\frac{1}{dr_{i,j}(dr_{i,j} + dl_{i,j})} + \frac{1}{dl_{i,j}(dr_{i,j} + dl_{i,j})} + \frac{1}{du_{i,j}(du_{i,j} + dd_{i,j})} + \frac{1}{dd_{i,j}(du_{i,j} + dd_{i,j})}} \quad (4.14)$$

This formulation has the significant advantage of requiring essentially the same computational effort as Eqn. 4.10, since all of the denominators involving dx and dy can be pre-calculated before iteration begins. Only a simple weighted average needs to be computed during iteration. However, the distance from (i,j) to each of the surrounding points can be varied independently.

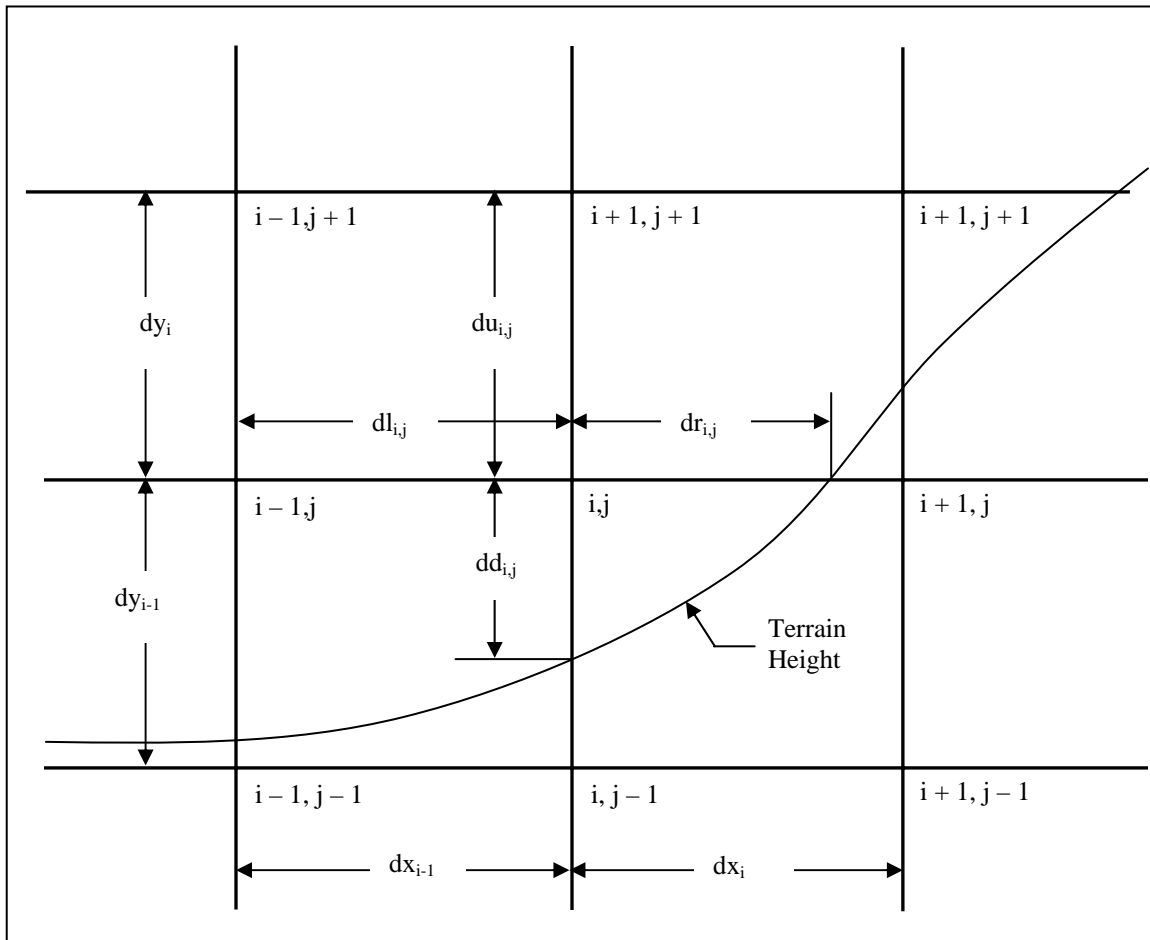


Figure 4-7 Grid layout and variable definitions used in Potential10.f90.

Near the surface, the stream function is defined as $\psi = 0$ for all points on and below the surface. There may be a discontinuity at the surface, as the potential gradient decreases immediately to zero at this point. Simply using the distance to the next grid point that is beneath the surface will cause the ψ gradient estimates to be too low because once past the actual surface, $\psi = 0$ by definition. Therefore, it is preferred to use data only at or above the surface to estimate ψ . This is done by adjusting dl , dr and dd to be the distance from point (i,j) to the surface when this distance is less than the distance to the next grid point. The program assumes no overhanging terrain. Therefore $du_{i,j} = dy_j$ at all times.

The terrain elevation as a function of x , $h(x)$, is defined in an input file as a series of regularly spaced spot elevations. The terrain elevation between two points is modeled as a linear fit. Then, *only* for grid points immediately adjacent to the surface,

$$\begin{aligned}
 dd_{i,j} &= y_{i,j} - h_i \\
 dl_{i,j} &= dx_{i-1} + \left(\frac{dx_{i-1}}{h_{i-1} - h_i} \right) (y_{i,j} - h_{i-1}) \\
 dr_{i,j} &= dx_i + \left(\frac{dx_i}{h_{i+1} - h_i} \right) (y_{i,j} - h_{i+1})
 \end{aligned}
 \tag{4.15}$$

These values also are pre-calculated before iteratively solving Eqn. 4.14.

Determining Speed-Up Factor

The boundary conditions imposed must represent an equilibrium flow. Since potential flow is inviscid, the flow field will not naturally form a boundary layer. Imposing upwind and downwind boundary conditions consisting of ψ distributions that correspond to logarithmic or power law velocity profiles will result in a flow that is not at equilibrium at the boundaries and in turn, will produce a flow field that is not physically realistic. Since evenly spaced streamlines are the equilibrium state in a potential flow, boundary conditions consistent with a constant value of $d\psi/dy$ are used, starting with $\psi = 0$ at the surface at both side boundaries.

Once the potential flow field is found, the final potential field is output to a file. Velocity components U and V are calculated using Eqns. 4.8. Bernoulli's equation is used to calculate pressure distribution. Fields of these variables are also stored in output files by the program. The primary measure of interest is the speed-up factor profile above the central point in the domain. Speed-up factor is essentially the deviation from the equilibrium potential gradient. Speed-up factor is calculated as

$$\Delta S = \frac{\left. \frac{\partial \psi}{\partial y} \right|_{i,j} - \left. \frac{\partial \psi}{\partial y} \right|_o}{\left. \frac{\partial \psi}{\partial y} \right|_o} = \frac{\frac{\psi_{i,j+1} - \psi_{i,j-1}}{du_{i,j} + dd_{i,j}} - \frac{\psi_{i,NY} - \psi_{i,NY-1}}{dy_{NY}}}{\frac{\psi_{i,NY} - \psi_{i,NY-1}}{dy_{NY}}}
 \tag{4.16}$$

Program Implementation

A program called "Potential10.f90" was written that applies Eqns. 4.14 and 4.15 to determine the stream function above a two-dimensional slice of complex terrain. The program was written in Fortran 90 using Microsoft Fortran Powerstation 4.0. The program should be compilable using other Fortran implementations, as only a few non-essential tasks (reading the command line arguments and displaying the elapsed iteration time) use the Microsoft libraries.

Run parameters, including grid size, names of input files, iteration parameters, are read from a setup file that can be specified on the command line when the program is run. If no filename is specified, a setup file named “Potential.inp” is assumed.

Terrain elevations are input to the potential program from two files: one stores a series of elevations that start at the point where speed-up is to be determined, with each subsequent elevation point being further from the origin in the upwind direction. A second file stores elevation points downwind of the origin. Both files contain the same number of points. The locations of the points in the file are used to set the size and spacing of the computational grid in the horizontal direction. Terrain files are generated from digital elevation model (DEM) files using Globalmapper 5.10. A Perl script is used to generate a Globalmapper script file that is used to extract elevation transects.

Each transect is stored in a separate file. These transects can be used directly with Potential10.f90; however, an additional Perl script is used to take a weighted average of the elevation at each distance out from the origin over a user-specified angle, typically 45°, with elevations in the center of the arc weighted highest. The 45° arc was chosen as representative of the upwind region that could be reasonably expected to be directly influencing the wind at the origin. For example, to simulate a wind from 240° at a met tower, the central upwind transect used would be one where the elevation points are on a 240° radial outward from the met tower location. However, this transect just might happen to include a small isolated butte that the wind blows easily around but is exactly 240° from the met tower. If only the 240° transect was used as the two-dimensional representation of the upwind terrain, this small three-dimensional feature could appear as a large ridge, potentially leading to an inaccurate solution. To minimize this effect, a weighted average is calculated of all the transects between 218° to 262°, and this averaged transect is used as the upwind terrain for a 240° wind. A Gaussian distribution was considered, since effects of wind direction are often distributed in this way. (Gaussian models are the standard in plume dispersion studies, for example.) However, a cosine weighting was ultimately used since it is mathematically simpler and does not “tail” at large angles, while still giving a distribution similar to Gaussian. For an averaging angle $\Delta\theta$ containing n transects and centered at angle θ_o , the weighting factor w_i of the i th transect, oriented at an angle of θ_i is

$$w_i = c_i / \sum_{i=1}^n c_i \quad c_i = 0.5 + 0.5 \cos \left[2\pi \left(\frac{\theta_o - \theta_i}{\Delta\theta} \right) \right] \quad (4.17)$$

Then the averaged elevation at a given distance from the origin $z_{\text{avg}} = \sum w_i z_i$ where z_i is the elevation in the i th transect.

Data in the input elevation files may be uniformly or variably spaced. For calculating speed-up at the central point in the terrain, variable spacing in which the smallest spacing is at the central point, and grid spacing increases with distance from the central point, allows the same span of terrain to be covered using a much smaller grid, which greatly reduced run times.

To account for regions of reduced flow in the wakes of hills, the program contains a terrain-filling algorithm that modifies the input terrain by “filling” in steep slopes so that the maximum

slope on the lee side of all hills is less than or equal to the user-specified slope ALPHA. This method approximately simulates the recirculation zone and very-low-speed wake regions in the lee of a steep hill by removing those areas from inclusion in the flow field (Myllerup et al., 2004). Several simulations of flow over a cosine hill (Table 3-13) were used to choose ALPHA = 7° (0.12) for this application. An example of the terrain changes due to filling is shown in Figure 3-8. ALPHA is set in the setup file. Setting ALPHA = 0.0 turns off the filling routine.

Table 4-13 Values of ΔS predicted for cosine hill for: NXIN = 251, DX = 10, Horizontal Spacing Factor = 1.0, NY = 90, DY = 1, DELTA = 1.1, UREF = 10, RHO = 1.2.

ALPHA	ΔS (0.5 m)	ΔS (10 m)	ΔS (99 m)
0 (No Fill)	0.531	0.482	0.230
0.04	0.343	0.305	0.155
0.06	0.373	0.332	0.167
0.12	0.439	0.394	0.194
0.25	0.508	0.459	0.221

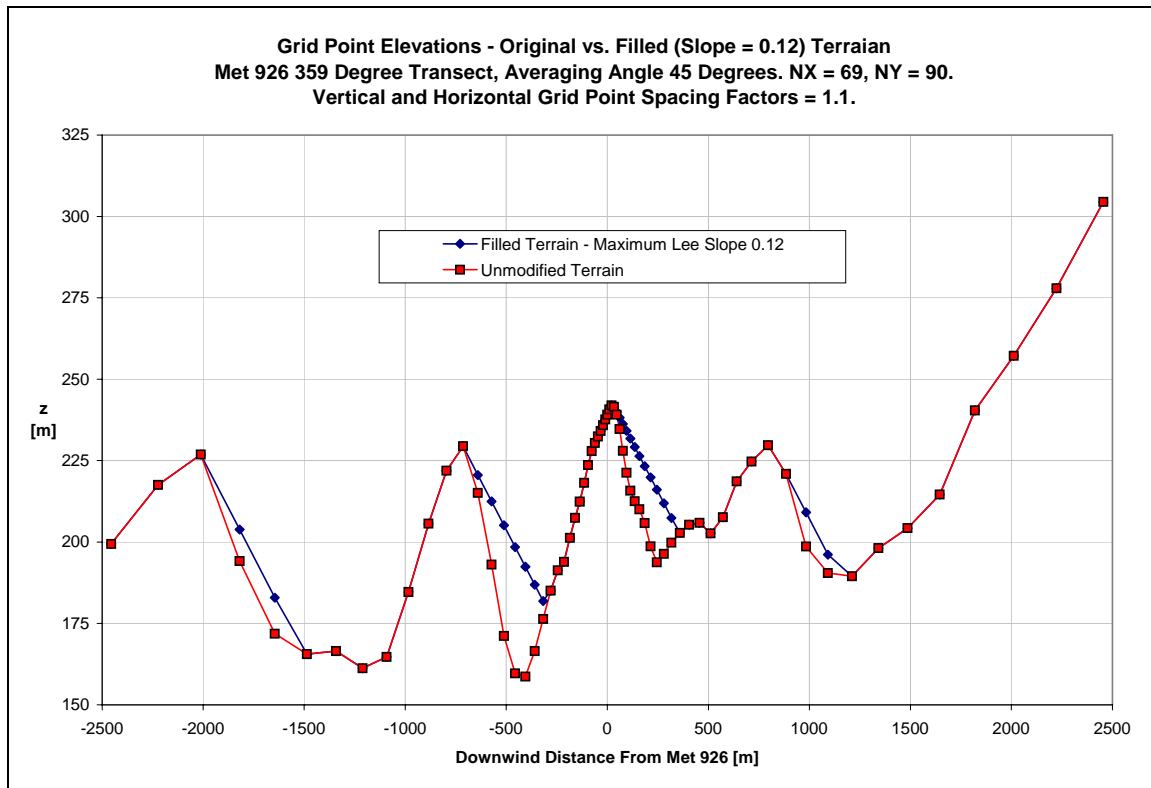


Figure 4-8 Example of the effect of lee slope filling (ALPHA = 0.12) on the Met 926 359° terrain transect. Each point on the traces represents the modeled terrain elevation for a specific horizontal grid location. Horizontal grid spacing factor is 1.1, resulting in more points near the origin, with greater grid spacing at greater distances upwind and downwind.

The vertical grid spacing is calculated in “Potential10.f90”. Spacing is based on the parameters DELTA and DY set in the setup file. The grid spacing at the elevation of the central point is set to DY. Starting at the elevation of the central point, grid point locations are extrapolated downward until the minimum terrain elevation is reached. Each grid point is spaced DELTA times further apart than the previous spacing (DELTA is typically set between 1.0 to 1.25). The grid is then generated upward from the central point terrain elevation, again making the spacing of each grid point DELTA times the spacing below until the maximum number of grid points, NY, has been reached. For a grid point that is i levels removed (either up or down) from the central grid point, the vertical distance to the $i+1$ grid point is $DY*(DELTA^{(i-1)})$. This approach concentrates grid points around the central point, while spacing points farther apart at greater distances, especially at high elevations far removed from the surface where flow variations occur over much larger length scales.

Upwind and downwind boundary conditions are set using a constant vertical stream function gradient ($d\psi/dy = UREF$) extrapolated upward from the surface on both the upwind and downwind boundary. UREF is set in the setup file. For all grid points below surface level, $\psi = 0$. Once ψ is fully defined on the upwind and downwind boundaries, the initial ψ field is calculated by linearly interpolating the two end conditions across the domain (again setting $\psi = 0$ at all points below surface level).

Equations 4.15 are pre-calculated for each grid point. Eqn. 4.14 is then solved iteratively using a Gauss-Seidel approach. This method incorporates updated values of ψ in subsequent calculations as soon as they are available. A modest increase in convergence rate was achieved by using four alternating sweeping methods in calculating updated values of ψ . (For example, the first iteration loop loops through “i” and then “j”. The second loops through “j” and then “i”. The third and fourth start at maximum values of “i” and “j” and finish at $i=1, j=1$.) Iteration is complete when none of the points in the domain change more than MAXDEV, or when a user-defined maximum number of iterations (MAXITERS) is reached. (MAXDEV and MAXITERS are set in the setup file.) Output files are generated of the stream function ψ , U and V velocity components, and pressure as determined using the Bernoulli equation. Finally, the speed-up factor profile at the central point is calculated and appended to a log file along with the run parameters. The “extract_profile...” series of Perl scripts can be used to determine the speed-up factors at user-specified elevations for all of the runs in the log file.

A large number of simulations (such as many directions around one or more locations) can be run by pre-generating the setup file for each run, using a batch file to call “Potential10” for each setup. This batch file can quickly be generated using a script such as “run_potential10_bat.pl.”

Iteration and Convergence

Initially, sample calculations were performed to simulate potential flow over both a single cosine hill and a offset of typical complex terrains. Results demonstrated that the potential flow calculation consistently converged, which was tested by comparing predicted stream function distributions and speed-up ratios and confirming that the absolute deviation at all points was less

than 0.001 after one more iteration cycle (Table 4-14). That is the calculation converged when MAXDEV was set to 0.001 or less. All tests were run with UREF = 10.0.

It also was found that a relatively large domain above the maximum terrain height was necessary when the results were to be used to determine speed-up factors. For example, for the typical Altamont Pass terrain, 3000 to 4000 meters of vertical calculation domain was needed above the surface to reliably converge to the same near-surface conditions. It was also found that DELTA = 1.1 would converge consistently to the same results as DELTA = 1.0 (i.e. uniform grid) when the domains covered the same physical space. Using DELTA = 1.1 and NY ≥ 90 resulted in consistent convergence to a solutions.

The time required to iterate a solution to the same level of convergence increases rapidly as the number of points in the domain increases. For example, solving a domain of 6210 points required 9 to 12 seconds (on a 3.2 GHz Pentium 4 computer), while solving a domain of 45,090 points required 250 to 300 seconds. Using a variable grid density, such as a spacing factor (i.e., DELTA) of 1.1 in both the horizontal and vertical directions to reduce the number of grid points was the most effective method of reducing run times.

Table 4-14 Values of ΔS predicted for the Met 127 0° transect. Inputs are NXIN = 35, Horizontal Spacing Factor = 1.1, NY = 90, DELTA = 1.1, UREF = 10, RHO = 1.2. Run time is the total time for iteration on a 3.2 GHz, Pentium 4 computer.

ALPHA	MAXDEV	ΔS (0.5 m)	ΔS (10 m)	ΔS (99 m)	Run Time (sec.)	Iterations
0.12	0.0000001	0.409	0.354	0.140	12	2363
0.12	0.000001	0.409	0.354	0.140	12	2363
0.12	0.00001	0.409	0.354	0.140	12	2363
0.12	0.0001	0.409	0.354	0.140	12	2341
0.12	0.001	0.409	0.354	0.140	9	1734
0.12	0.002	0.409	0.354	0.140	8	1466
0.12	0.005	0.410	0.355	0.141	6	1174
0.12	0.01	0.414	0.358	0.143	4	885
0 (No fill)	0.0001	0.476	0.414	0.153	9	1732
0 (No fill)	0.0005	0.476	0.414	0.153	9	1732
0 (No fill)	0.001	0.476	0.414	0.153	8	1584
0 (No fill)	0.002	0.477	0.414	0.153	7	1341
0 (No fill)	0.005	0.478	0.415	0.153	6	1101
0 (No fill)	0.01	0.482	0.419	0.156	4	816

For simulation of Altamont Pass terrain, the following run parameters were found to converge to results that could be verified using higher resolution runs with lower convergence criteria: DX = 10, DY = 1.0, DELTA = 1.1, NY = 90, MAXDEV = 0.001, MAXITERS = 20000, ALPHA = 0.12, UREF = 10, RHO = 1.2. The Altamont Pass wind turbine and met tower sites were simulated using terrain files using 35 elevations and a spacing factor of 1.1 between each

elevation, providing approximately 2.5 km of upwind and downwind terrain relative to the origin.

Initial Validation: Cosine Hills

The potential programs were initially validated using the simulation of a simple hill of cosine cross-section. The hill was modeled at various factors of h/L by setting $h = 100$ m, and varying L from 100 m to 1000 m. The ABLWT tests of the two-dimensional cosine hill at 0° relative wind angle are simulated when $h/L = 0.54$. The domain was uniformly spaced horizontally, with variable vertical spacing. ($DX = 10$, $DY = 1.0$, $DELTA = 1.1$, $NX = 501$, $NY = 90$). The filling function was disabled to simulate a true potential flow, for comparison with previous linear results. The speed-up factor at the top of the cosine hill was calculated for eight values of h/L , and Figure 4-9 presents the results.

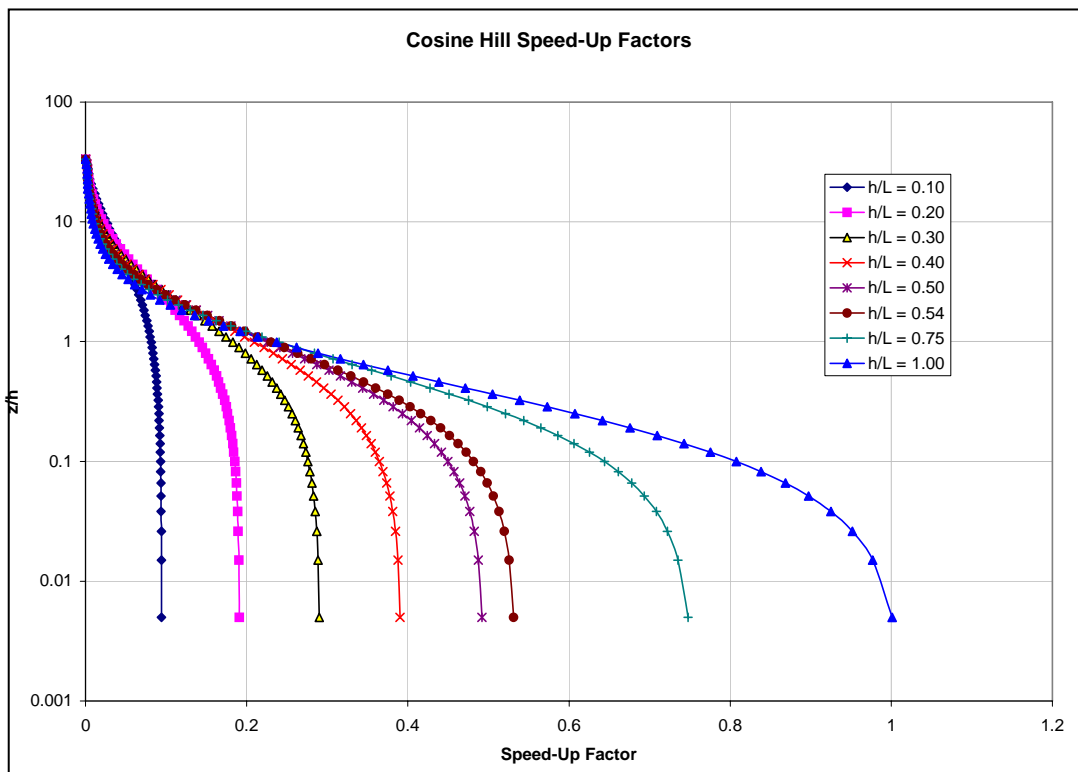


Figure 4-9 Potential flow solver predictions of hilltop speed-up factor versus height for cosine cross-section hills of varying h/L .

The results agree well with established results. As Jackson and Hunt (1975) showed, speed-up factor varies linearly with h/L , consistent with Figure 4-9. Speed-up factor also decays in an exponential manner with height. Figure 4-10 compares the results to various empirical speed-up prediction methods and the ABLWT wind tunnel results and indicates the potential flow solver underpredicts the speed-up factors, especially near the surface. This is also consistent with previous researchers who noted that linear or potential-based methods underpredict speed-up (Weng et al., 2000).

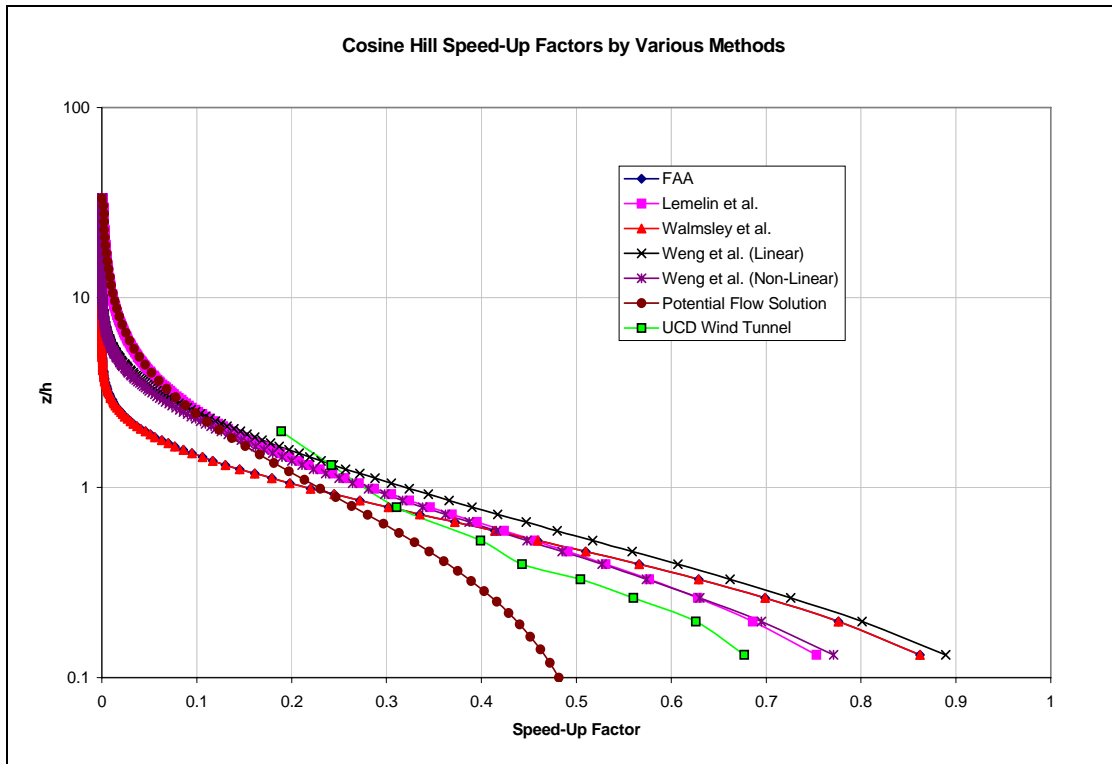


Figure 4-10 Hilltop speed-up factors predicted for cosine hill of $h/L = 0.54$ by empirical prediction methods, potential flow solver and UC Davis wind tunnel.

Powerworks Meteorological Towers

Speed-up factors were calculated using “Potential10.f90” for each of the Powerworks meteorological towers, and Figure 4-11 presents the resulting speed-up factors as functions of the wind direction. The curves were generated by running the model for each tower and wind direction from 0° to 359° degrees, in 1-degree increments. A variable grid of 71 by 90 cells was used for all simulations, with a spacing factor of 1.1 in both the x and y directions. The speed-up factor was calculated at the anemometer height of each meteorological tower.

Previously, it was noted that, for the 240° wind direction, the wind tunnel measurements predicted the wind speed ratio between Met 127 and Met 225 is $U_{127}/U_{225} = 0.98$. Based on the actual meteorological data, this ratio appears to be somewhat low. Depending on the time of day and season, the ratio actually varied between about 1.06 and 1.35 (Table 4-1), with higher values associated with higher atmospheric stability. The ratio of the 240° -model and Potential10.f90 model predictions is $\Delta S_{127}/\Delta S_{225} = 0.32/0.24 = 1.33$. Assuming an average reference wind speed of 7 m/s, this results in $U_{127}/U_{225} = 1.06$, which agrees well with the average observed velocity ratios for neutral/unstable periods.

The complexity of the ΔS vs. wind direction curves for the meteorological towers also should be noted. While the wind tunnel R value curve for Met 127 was a simple cubic fit through four points (Figure 4-4), the “Potential10.f90” results show more complicated dependencies

due to local topography. For example, the Met 127 curve shows a sharp reduction of ΔS around the 280° direction, where the local ridgeline extends upwind, with even higher terrain further upwind. Unless a large number of wind directions can be tested, this level of resolution is not easily reached in wind tunnel tests.

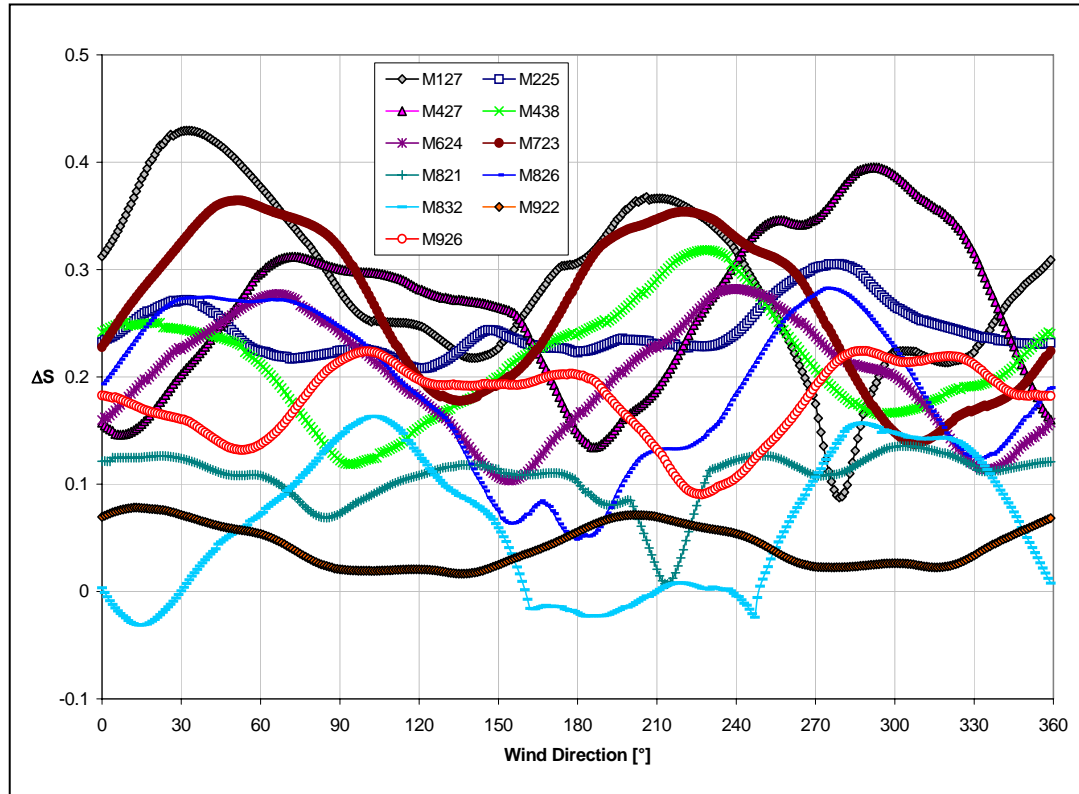


Figure 4-11 Potential10.f90 predictions of speed-up factor as a function of wind direction for the Powerworks meteorological towers.

Power Curve Generation Using the Potential Flow Solver

The program “Potential10.f90” was used to generate a power curve for the Powerworks Met 127 turbine cluster. The resulting power predictions are directly comparable to those produced by the method based on wind tunnel measurements described previously. The heart of the wind tunnel method was a database of velocity ratios (R values) defined as $R = U_{\text{turb}}(\theta) / U_{\text{met}}(\theta)$, where θ is the wind direction. The potential solver method was applied to generate an equivalent database using flow field predictions via multiple runs of “Potential10.f90”.

Elevation transects were determined for winds from 0° to 355°, in 5° steps, for each of the 93 turbine locations. Each transect contained 35 elevations starting with a 10 meter horizontal spacing at the origin, with spacing increased by a factor of 1.1 between each set of successive points, so that the final point was 2.454 km from the origin. The program was run for each of the 94 locations and 72 wind directions. R values for each turbine were then calculated based on the potential gradient at the height of the wind turbine or anemometer. The height of the anemometer

and most of the turbines is 18.3 m (60 ft), and six of the turbines are at 24.4 m (80 ft) height. That is, at a height $y = z$,

$$R_{turb}(z, \theta) = \frac{\left. \frac{\partial \psi}{\partial y}(z, \theta) \right|_{turb}}{\left. \frac{\partial \psi}{\partial y}(z, \theta) \right|_{met}} \quad (4.18)$$

The resulting potential flow solver R values were compared to those measured in the wind tunnel. Overall, the predictions by the potential solver method were similar to those based on the wind tunnel measurements. The mean difference between the corresponding R values predicted by the two methods is 0.008, and the mean absolute difference is 0.034. The average predicted R value is 0.934. Appendix A presents Tables listing the R-values predicted by both methods for all of the turbines and the four wind directions.

The wind tunnel prediction scheme was rerun using the new set of R values generated by the potential solver, and the power prediction accuracies of the potential flow and wind tunnel methods were compared. The results are described in the following sections.

Altamont Wind Farm Power Prediction Accuracy

Multiple wind farm power curves were derived using four different methods: 1) data from measurements in the ABLWT, 2) potential flow simulations of the wind farm area by the program “Potential10”, 3) fitting a curve to the median values of power production, binned by wind speed, for two years of historical data, and 4) screening multiple linear regression of two years of historical data. These methods will be referred to below as “ABLWT”, “Potential10”, “Median Fit,” and “SMLR” respectively.

Each of the methods was used to predict the power production of the Met 127 turbine cluster on a half-hourly basis during the period. June 25, 2001, to June 11, 2005. The inputs were the Met 127 meteorological tower wind speed and direction, temperature from Met 438 (the most representative data available), and the time of year. After deleting missing or incomplete data (6.9% of the total), 64,685 predictions were produced. The predictions were compared to the recorded observations, and ME and MAE values were calculated. Table 4-16 summarizes the overall performance of the methods .

It should be noted the first two years of the dataset include the data used to train the two data fit methods (July 1, 2001, to June 30, 2003); therefore the performance of these methods can strictly be evaluated only for times outside this time frame.

Another difficulty is the observed lack of reliability of the wind direction data: 51% of the almost four-year dataset includes unreliable wind direction data. It is not possible to construct a “representative year” because no reliable data are available during the period, April 12 to May

24, in any year. Evaluating ME and MAE for only those periods when wind direction data appeared acceptable, the relative performance of the power curves is similar (Table 4-17).

Table 4-15 Overall mean error (ME) and mean absolute error (MAE) of Met 127 power predictions, as percentages of observed wind farm capacity for four wind farm power curve methods, June 25, 2001, to June 11, 2005.

Prediction Method	ME (%)	MAE (%)
ABLWT (No Wind Direction)	3.24	6.12
ABLWT (w/ Wind Direction)	1.99	5.74
ABLWT (w/ Wind Direction and Density)	1.92	5.82
ABLWT (Optimum)	-0.36	5.74
Potential10 (No Wind Direction)	4.68	7.05
Potential10 (w/ Wind Direction)	2.47	6.31
Potential10 (w/ Wind Direction and Density)	2.40	6.31
Median Historical Data Fit	0.73	5.38
MLR Historical Data Fit	0.42	6.33

Table 4-16 Mean error (ME) and mean absolute error (MAE) of Met 127 power predictions, as percentages of observed wind farm capacity, for four different wind farm power curve methods. Includes only observations for which Met 127 wind direction data were considered acceptable between June 25, 2001, to June 11, 2005.

Prediction Method	ME (%)	MAE (%)
ABLWT (No Wind Direction)	2.55	6.18
ABLWT (w/ Wind Direction)	2.06	5.96
ABLWT (w/ Wind Direction and Density)	1.89	6.01
ABLWT (Optimum)	-0.38	5.80
Potential10 (No Wind Direction)	4.17	7.21
Potential10 (w/ Wind Direction)	3.10	6.77
Potential10 (w/ Wind Direction and Density)	2.92	6.74
Median Historical Data Fit	0.07	5.49
MLR Historical Data Fit	-0.34	6.49

The MAE of all methods is dependent on the wind speed (Figure 4-13), and the MAE is higher in the 5 to 12 m/s range, which corresponds to the steep portion of the Kennetech power curve, and very low below 4 m/sec, where power production and predictions are both generally zero. The non-zero values of MAE, particularly those between zero and 1 m/s, are due to reported non-zero power production from the wind farm.

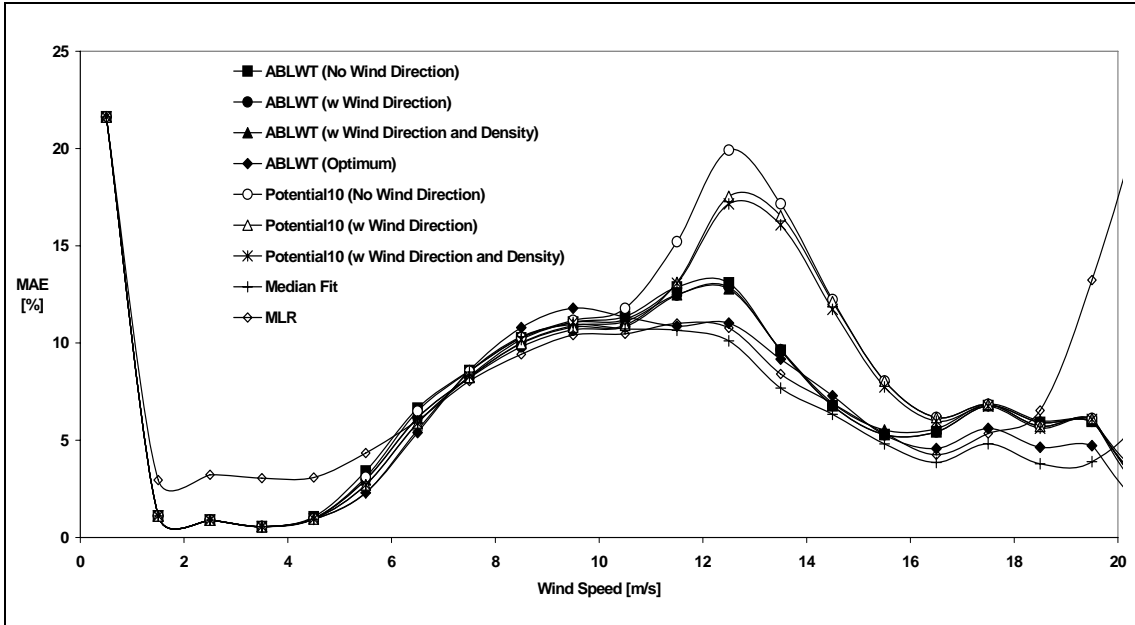


Figure 4-12 Mean absolute error (MAE) of Met 127 power predictions versus wind speed, as a percentage of observed wind farm capacity. Includes only observations for which Met 127 wind direction data were considered acceptable between June 25, 2001, and June 11, 2005.

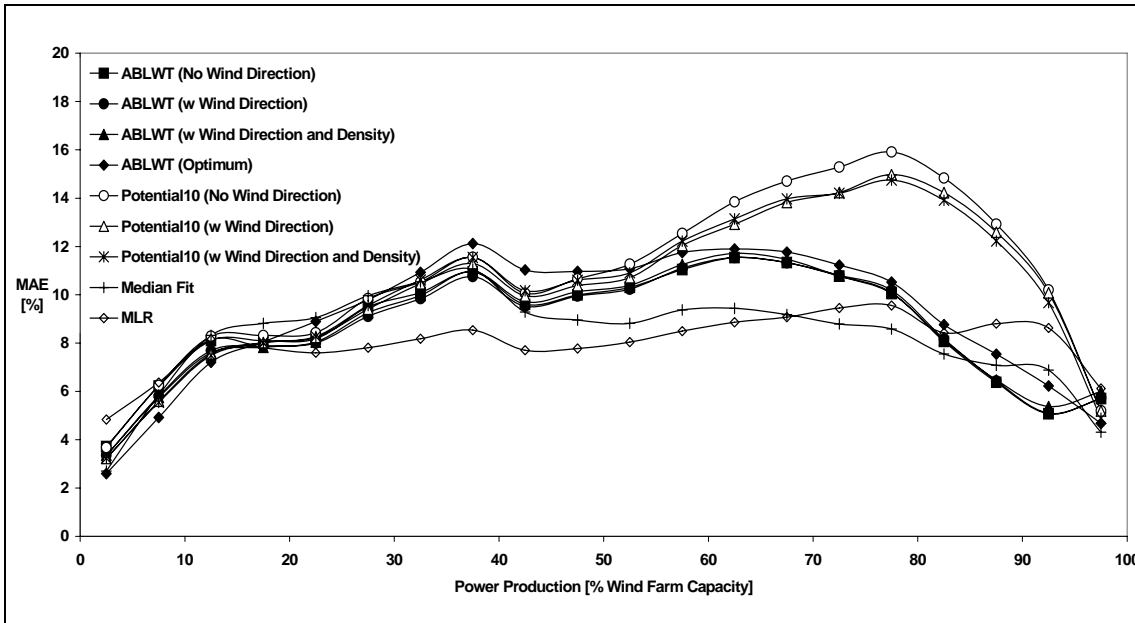


Figure 4-13 Mean absolute error (MAE) of Met 127 power predictions versus actual Met 127 power production, as percentages of observed wind farm capacity. Includes only observations for which Met 127 wind direction data was considered acceptable between June 25, 2001, to June 11, 2005.

The MAE is also a function of the power production (Figure 4-14). It should be noted that power production of less than 5% of the farm capacity accounts for 48% of the observations. Basically, the turbines are not generating power about half the time, a relatively easy case to predict. The

overall MAE is heavily weighted to the no power production case. Looking at MAE as a function of the actual power production, it becomes apparent that MAE is generally higher when power is being produced, with some decrease again when the farm approaches maximum power production.

Generally, the ABLWT method outperformed the Potential10 method, mainly due to a tendency of the Potential10 simulation to overpredict power production across a wide range of wind speeds. It should be noted that the ABLWT method has been more extensively developed than the Potential10 method. Therefore, it may be possible to improve the Potential10 method by refining the model, especially regarding the treatment of hill wake effects.

Forecasting with the Power Curves

Several wind farm power curves were developed based on (1) data from measurements in the ABLWT, 2) potential flow simulations of the wind farm area by the program Potential10, and 3) fitting a curve to the median values of power production, binned by wind speed, for two years of historical data. These methods are referred to as the “Wind Tunnel,” “Potential Simulation,” and “Historical Fit” methods, respectively.

All of the methods were used to forecast the power production of the Met 127 turbine cluster hourly for the period from December 1, 2001, to September 30, 2002. AWS Truewind provided the input data for the power curves, consisting of next-day forecasts of wind speed and direction at the Met 127 meteorological tower. The forecasts simulated a next-day operational forecast initialized at 0Z, so the forecast interval was dependent on the time of day. Density corrections were not applied.

After deleting forecasts for which Met 127 data were missing or incomplete (5.1% of the total), 6922 forecasts were generated for each method. In addition, power production was predicted using the actual wind speed and direction recorded at the meteorological tower (simulating a “perfect forecast”), and AWS Truewind provided another forecast of power production. The ME and MAE for this forecast were also calculated using the same data.

Table 4-17 Power curve performance for entire forecast period, December 1, 2001, to September 30, 2002. ME and MAE values are expressed as percentage of observed wind farm capacity.

	Power Curve Input Data			
	Actual Wind		Forecasted Wind	
	ME (%)	MAE (%)	ME (%)	MAE (%)
Wind Tunnel w/o Wind Dir.	2.59	5.64	0.52	15.29
Wind Tunnel w/ Wind Dir.	1.60	5.52	-0.68	15.17
Potential Simulation	1.83	6.32	-0.19	15.63
Historical Fit	0.03	5.22	-2.53	15.01
Truewind Forecast			0.25	15.28

Table 4-18 compares the overall performance of the power curves over the entire time period, using forecasted and actual meteorological data for inputs, and Tables 4-19 through 4-20 compare the performance for December 2001, May 2002, and July 2002. AWS Truewind used these months to represent periods of low-, medium-, and high power production.

Table 4-18 Power curve performance for December, 2001. ME and MAE values are expressed as percentages of observed wind farm capacity.

	Power Curve Input Data			
	Actual Wind		Forecasted Wind	
	ME (%)	MAE (%)	ME (%)	MAE (%)
Wind Tunnel w/o Wind Dir.	5.93	6.55	1.18	6.36
Wind Tunnel w/ Wind Dir.	5.08	5.81	0.51	5.93
Potential Simulation	4.95	5.85	0.73	6.18
Historical Fit	4.01	5.25	-0.65	5.52
Truewind Forecast			1.32	6.56

Table 4-19 Power curve performance for May 2002. ME and MAE values are expressed as percentages of observed wind farm capacity.

	Power Curve Input Data			
	Actual Wind		Forecasted Wind	
	ME (%)	MAE (%)	ME (%)	MAE (%)
Wind Tunnel w/o Wind Dir.	2.46	6.01	1.62	22.61
Wind Tunnel w/ Wind Dir.	-0.40	6.07	-2.89	22.51
Potential Simulation	-1.95	6.92	-4.75	22.15
Historical Fit	-0.97	5.77	-2.75	22.70
Truewind Forecast			1.75	22.65

Table 4-20 Power curve performance for July 2002. ME and MAE values are expressed as percentages of observed wind farm capacity.

	Power Curve Input Data			
	Actual Wind		Forecasted Wind	
	ME	MAE	ME	MAE
Wind Tunnel w/o Wind Dir.	1.21	4.72	0.77	17.22
Wind Tunnel w/ Wind Dir.	0.89	4.74	-0.14	17.27
Potential Simulation	3.43	6.84	2.79	18.91
Historical Fit	-1.83	4.74	-3.07	17.49
Truewind Forecast			-0.29	17.22

When used to predict power production using the actual recorded wind speed and direction, the power curve methods all performed in a manner consistent with the previously documented applications. The MAEs were between 5 and 7 percent of the observed capacity (Table 4-18). Using forecasted wind speed and direction instead of the actual values results in a significant, but

reasonable, increase in MAE to approximately 15 % to 16%, depending on the method (Tables 4-19 to 4-21).

The power curves are reasonably accurate the resulting power forecast MAEs are similar to those for AWS Truewind's operational power curve. This is a significant result because the wind tunnel and potential simulation methods require no historical power production or on-site meteorological data. These methods may be of most value in situations where historical wind farm data are not available, such as in resource assessment and turbine site selection for new wind farms.

5

Downscaling and Forecasting

Uncertainty of the Eta Regional Scale Forecast (RSF)

There is a perception that the majority of the uncertainty in commercial wind power forecasting results is due to the uncertainty in the output of the RSFs that are used as inputs to the forecasting systems. However, the measures of error made available by RSF operators rarely assess the error in the specific input variables used by wind power forecasters (such as wind speeds at geostrophic levels), or provide only averages of the error levels in a variable over many forecasts and therefore cannot be compared directly to specific wind power forecasts.

Comparison of Interpolation Methods: Bicubic, Bilinear, and Nearest Point

Weather conditions at a nearby radiosonde launching site (Oakland, CA, USA, 45 km west of Altamont Pass. WMO ID# 72943. (See Figure 5-1) were forecasted and compared to observations in an attempt to gauge the accuracy of the RSF. Forecasting in this context consisted only of interpolating the forecasted variables from the Eta grid points to the Oakland

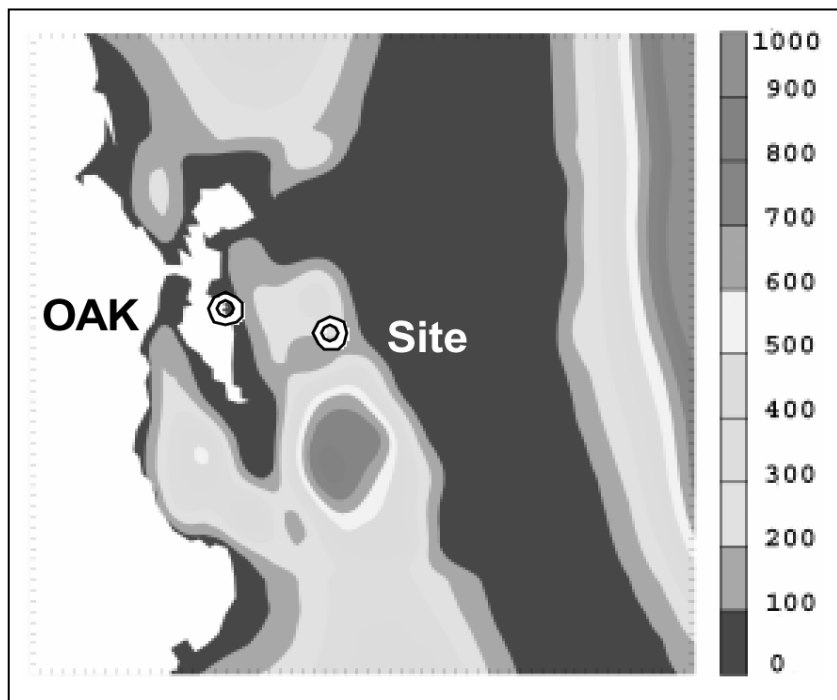


Figure 5-1 Map of Altamont Pass site ("Site") and Oakland radiosonde site ("OAK"). Elevations in meters. Map area is 240 km wide.

site. No statistical or other corrections were applied. It should be noted that since the Oakland site is in different terrain, near sea-level adjacent to the San Francisco Bay, the meteorological factors affecting downscaling will be somewhat different, especially for near-surface observations. The radiosonde is launched twice daily at 0:00 GMT and 12:00 GMT and reports wind speed and direction, temperature, and dew point at various altitudes from the surface to well into the stratosphere.

Initially, bicubic interpolation was used to extrapolate forecast weather conditions from the RSF grid points to the sounding location. However, it was suspected that the interpolation method itself also introduces error. Therefore, bilinear interpolation and a closest grid point method also were implemented to investigate the sensitivity of the error levels to the interpolation method. Any or all of these interpolation methods can be used in the UC Davis forecasting system to extrapolate gridded RSF data to wind farm meteorological tower locations. By interpolating the RSF output to the radiosonde location, many upper level variables forecasted by the RSF can be compared to field measurements on a forecast by forecast basis, and the level of uncertainty in the data from the RSF can be estimated.

The three interpolation methods were compared by using archived Eta forecasts for a 21-month period from November 30, 2002, through July 31, 2004. The Eta forecasted wind speed at each of the surrounding grid points was determined from the horizontal components of the wind speed at each grid point. This data then was interpolated to the sounding location using bicubic or bilinear interpolation. The third “interpolation” method involved using the data from the closest grid point to the sounding location. The radiosonde takes frequent measurements as it rises, typically one or more every few hundred meters. Readings were linearly interpolated to the pressure of Eta levels for analysis. No statistical or other corrections were applied.

The overall error level is measured by the mean absolute error (MAE), the absolute value of the forecasted minus the actual value. The MAEs of the wind speed forecasts were almost identical for the three interpolation methods implemented.

Figure 5-2 presents the wind speed MAE results at several different levels and at various forecast intervals. As expected, error levels increase over longer forecast intervals, and higher levels tend to be forecasted more accurately than lower levels. In absolute terms, MAE values varied between 1.5 m/s for the initialization runs at 700, 800, and 900 mb to 2.5 to 3 m/s for the 48-hour forecasts. The relatively high MAEs observed in the initialization runs “forecasting 0 hours ahead” were somewhat unexpected, since the sounding data are used to initialize the Eta model. However, the explanation is that the measured data must be interpolated to the grid points and modified to agree with other available data, thus increasing the discrepancy between actual and interpolated data. Additionally, each model run starts at minus 12 hours to ensure stability and consistency by hour zero, so only earlier sounding data are used. This provides additional opportunity for the initialization run to diverge from the measured data at hour zero.

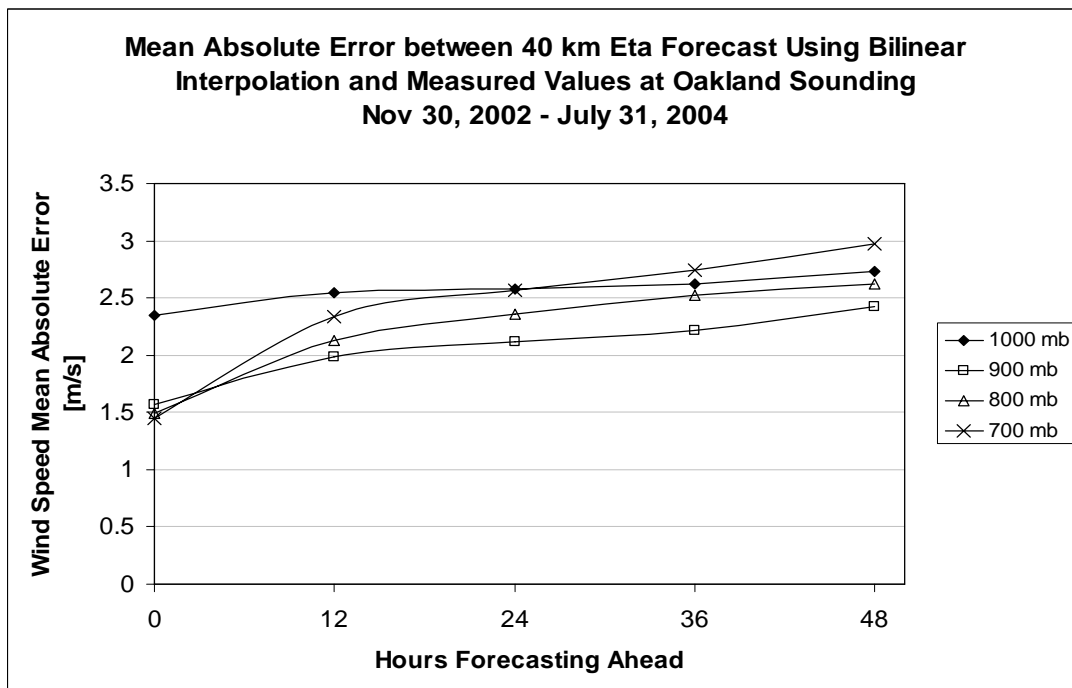
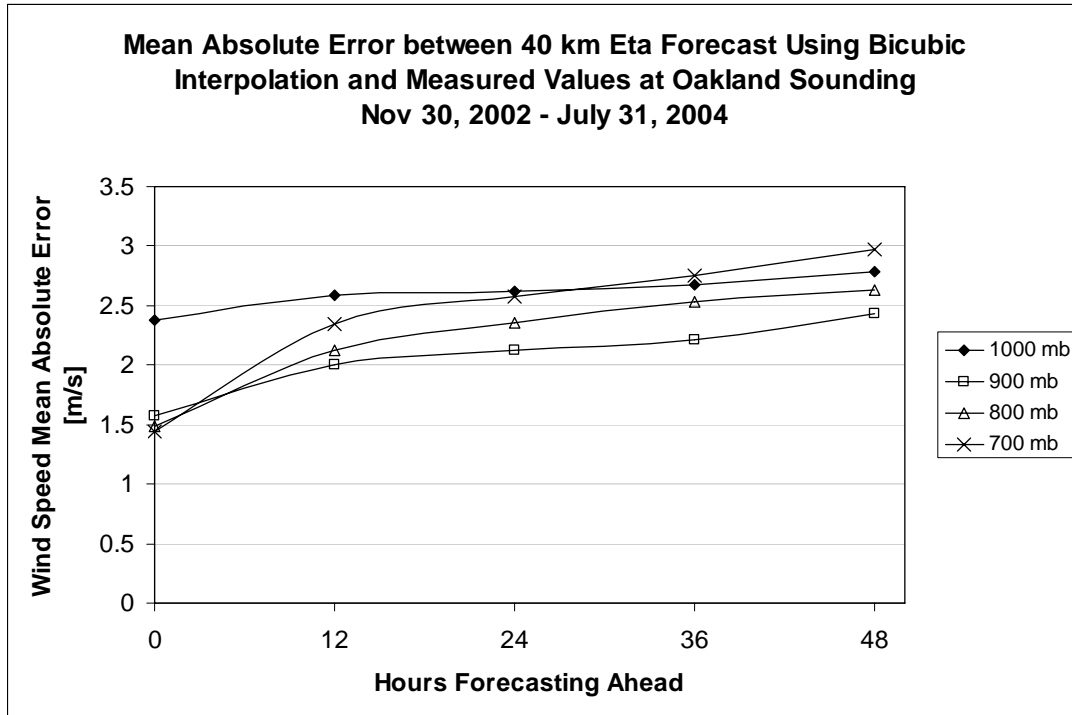


Figure 5-2 Mean absolute error in Eta forecasted wind speed at Oakland sounding location for four different levels as a percentage of the average measured wind speed observed at that level. Forecasted winds at the sounding location were determined from gridded Eta model output using bicubic interpolation (top), bilinear interpolation (middle), and the grid point closest to the sounding location (bottom). Results are given for forecast intervals from 0 hours ahead (initialization run) to 48 hours ahead.

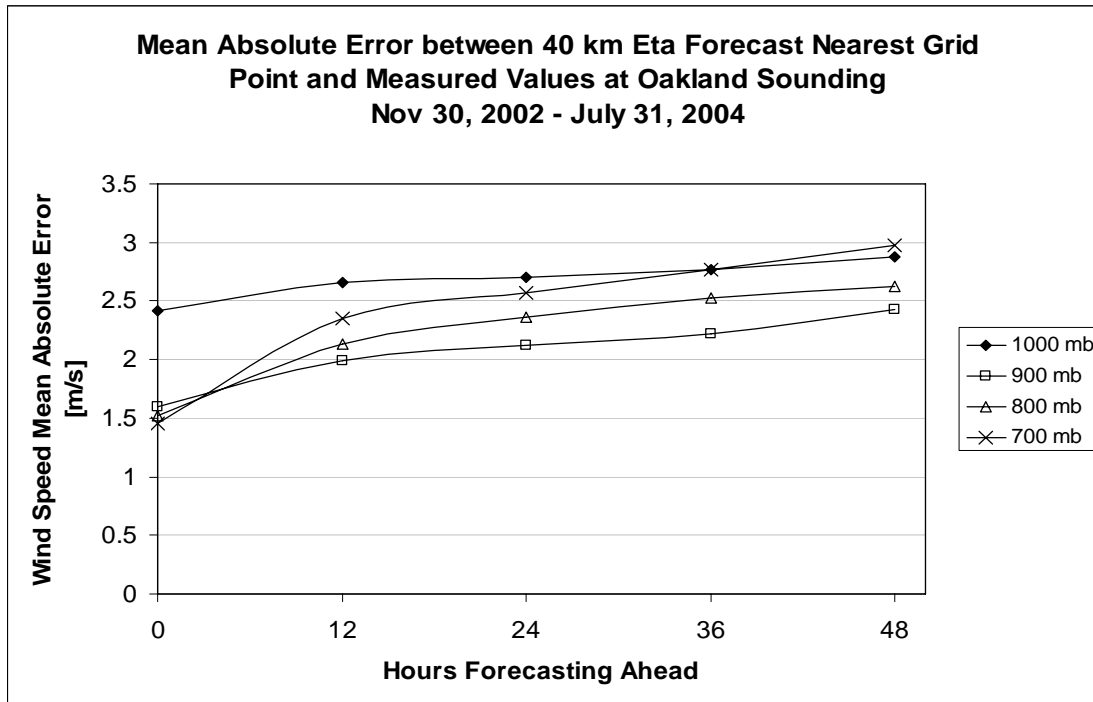


Figure 5-3 Mean absolute error in Eta forecasted wind speed at Oakland sounding location for four different levels (Continued).

Downscaling

Once a regional-scale forecast (RSF) is obtained, the resulting forecast data are used to forecast the near-surface wind speed. This is necessary since the RSF models have such coarse grid spacing (Eta's grid spacing is 40 km) that only the largest terrain features, such as large mountain ranges, can be represented. Even with much finer grid resolutions, the region near the surface where wind turbines are located is the most difficult region to model accurately. The process of taking upper-atmosphere RSF model data and extrapolating to surface conditions at a specific point is referred to as “downscaling.”

Geostrophic Drag Law

Landberg and Watson (1994) used the geostrophic drag law to forecast near surface wind speeds from upper air wind speeds taken from an RSF. This method involves the use of a few equations that can be solved iteratively with little computational effort. The neutral geostrophic drag law is a method of predicting surface shear stress, in the form of the friction velocity U^* , based on the wind speed at geostrophic height U_G :

$$U_G = \frac{U_*}{\kappa} \sqrt{\left[\ln\left(\frac{U_*}{fz_o}\right) - A \right]^2 + B^2} \quad (5.1)$$

where f is the Coriolis parameter, z_o is the surface roughness and κ is von Karmen's constant (≈ 0.4). A and B are constants. Zilitinkevich found that the median values of A and B reported in 16 studies gave $A = 1.7$ and $B = 4.5$. The angle of the surface shear stress direction from the direction of the geostrophic wind angle α is given by

$$\tan \alpha = \frac{-B}{\ln\left(\frac{U_*}{fz_o}\right) - A} \quad (5.2)$$

Landberg and Watson (1994) used Eqns. 5.1 and 5.2 in conjunction with the logarithmic law (Eqn. 2.2) to predict a reference wind speed at turbine hub height from upper atmosphere winds forecasted by HIRLAM. While Landberg reported success applying this method to sites in Denmark and other parts of northern Europe, the reliability of the geostrophic drag law appears to break down in the more complex terrain of the Altamont Pass, and this approach did not accurately predict the near-surface winds at the case study wind farm.

To determine if this method could be applied to the Altamont Pass region, archived initialization runs (i.e., “zero hour forecasts”) of Eta model output from November 30, 2002, to July 31, 2004, was used to predict the wind speed at the case study wind farm meteorological tower. To use this method, first a vertical level in the Eta output had to be chosen as being at the geostrophic height. Six different levels evenly spaced between 700 and 950 mb were used as geostrophic level on a trial basis. For a specific forecast, the overall wind speed at the geostrophic height was taken from the Eta model output. Eqns. 5.1, 5.2, and 2.7 then were used to predict the wind speed that would be seen at the meteorological tower if it were situated in flat terrain. A speed-up factor of 1.5 then was applied to the forecasted wind speed to account for the ridgetop location of the meteorological tower. The speed-up factor was determined by comparing wind speeds at simulated anemometer height in an ABLWT test of the complex terrain around the meteorological tower site, with a test of flat terrain.

Table 5-1 presents the results of the analysis for geostrophic heights at six different levels. Input wind speeds are from geostrophic height in Eta model initialization runs (“0 hour forecasts”) between November 30, 2002, and July 31, 2004. The average wind speed measured by the meteorological tower was 7.46 m/s. The R values are the correlation coefficients between the Eta model wind speed at each given geostrophic height and the measured wind speed at the meteorological tower.

The average forecasted wind speed at the meteorological tower anemometer was low for all of the “trial” geostrophic heights, even with the application of the speed-up factor. A closer look at the data revealed a significant lack of correlation between the wind speed at geostrophic height, and the wind speed at the meteorological tower location, with correlation coefficients ranging from 0.04 when compared to the 700 mb wind, to 0.34 when compared to the 950 mb wind. It is

Table 5-1 Mean Error (ME) and Mean Absolute Error (MAE) of predictions of wind speed at case study wind farm meteorological tower (in m/s) using geostrophic drag law.

	Geostrophic Level					
	700 mb	750 mb	800 mb	850 mb	900 mb	950 mb
ME	-0.86	-1.76	-2.46	-2.88	-3.03	-3.02
MAE	4.57	4.41	4.34	4.39	4.23	3.90
R	-0.04	-0.02	0.00	0.04	0.14	0.34

apparent that this lack of correlation represents a potentially large source of error in a forecast for the case study site.

Multiple Linear Regression

Burda et al. (1985) reported success predicting the average daily wind speed at an Altamont Pass site with an equation derived using multiple linear regression, using inputs of the zonal component of the 950 mb Oakland sounding wind speed and the maximum daily air temperature in San Francisco. Unfortunately, attempts to use multiple linear regression to derive equations to predict the wind speed at the meteorological tower anemometer at a specific time using variables from the Eta model output were unsuccessful, with no equation derived, even for specific cases (such as for specific times of day or seasons) have an R^2 value greater than 0.5. This was attributed primarily to the lack of correlation between the meteorological tower wind speed and the upper level wind speeds, temperatures and pressures.

For example, Figure 5-4 shows the relation between the wind speed at 700 mb in the Eta initialization runs ("zero hour forecasts") and the wind speed as measured at the meteorological tower.

Forecast Matching

Due to the lack of success predicting the wind conditions at the wind farm meteorological tower from the Eta output using the above methods, it was decided to use the archives of Eta forecasts and wind farm data compiled at UC Davis to directly predict the wind farm conditions.

UC Davis archives the information from each Eta forecast in a separate file after the forecast is downloaded. The corresponding data from the wind farm (wind speed and direction, and power production) for each forecast time interval are appended to the forecast file, so that each archived forecast file contains the measured wind farm conditions at the forecast time for future error analysis. A "matching forecast" can be generated by downloading a current Eta forecast and then searching the archive for a "matching" archived forecast; one with conditions closest to those predicted by the current forecast. Since the two "matched" forecasts are for two times with similar weather conditions, it is anticipated that the wind farm conditions for the current forecast will be close to those associated with the "matched" archived forecast: the archived wind speed and direction (and the power production) are used as a new forecast.

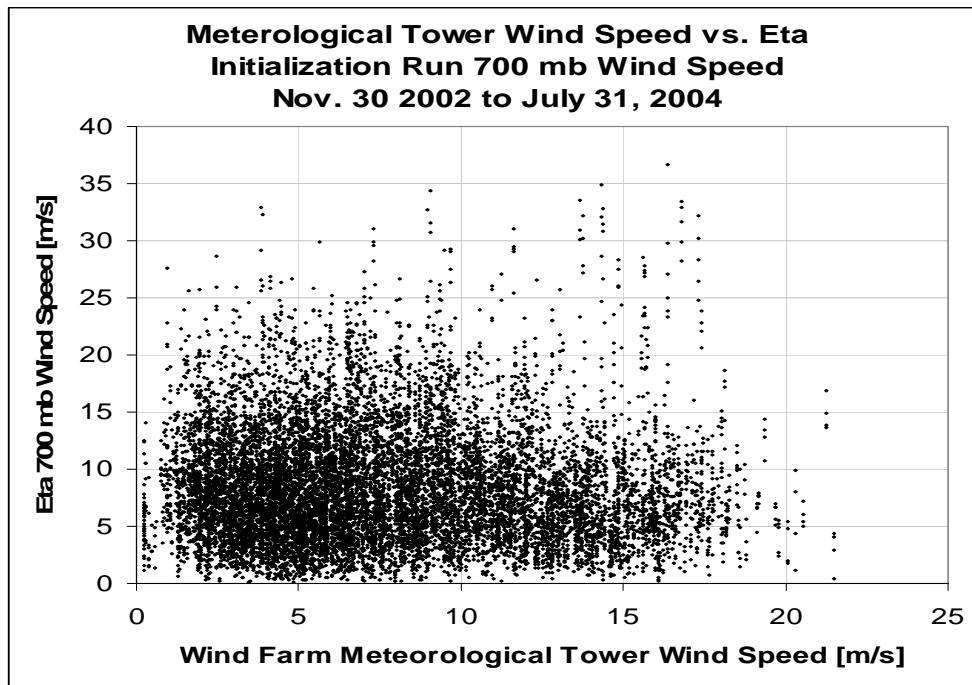


Figure 5-4 Comparison of the wind speed measured at the meteorological tower versus the wind speed at the 700 mb level of the Eta initialization ("zero-hour forecast") runs.

It was necessary to develop a means of quantifying the similarity between two Eta forecasts to find a match. A scoring system was devised to quantify the degree of difference between a set of corresponding variables in the current forecast and an archived forecast. The set of 19 variables chosen to compare archived and current forecasts included the "U" and "V" components of wind speed, temperature, elevation at 1000 mb, 900 mb, 800 mb, and 700 mb, sea-level pressure, and the horizontal components of the pressure gradient, determined via bicubic interpolation.

The "matching score" S of the two forecasts was then calculated as

$$S = \sum_{i=1}^n \left(\frac{A_i - F_i}{R_i} \right)^2 \quad (5.3)$$

where n is the number of variables (19 in this case), A_i and F_i are the archived and current forecast values of variable i (where $1 \leq i \leq n$), and R_i is a normalizing factor used to weight the importance of the variable. (Initially for each variable, R was arbitrarily set equal to the standard deviation of the variable observed in the dataset, divided by four to make many of the R values close to one. Only the relative values of R_i affect the scoring of the different variables.) A score is calculated for each archived forecast, with a lower score indicating greater similarity between an archived forecast and the current forecast. For a given current forecast, the wind farm conditions are taken from the file of the lowest scoring archived forecast.

The accuracy of the matching method was determined by forecasting the wind farm conditions corresponding to each of the archived forecasts. When a specific forecast was being determined, archive forecasts within four days of the one being used were excluded from the matching analysis. This ensures that the forecast is not matched to itself, or to a forecast close in time, representing the identical weather conditions in the forecast. Both wind speed at the meteorological tower anemometer and wind farm power production were forecast. Table 5-2 summarizes the ME and MAE results.

Table 5-2 Observed accuracy of the matching method at forecasting wind speed at the case study wind farm meteorological tower anemometer and the wind farm power production. Forecasts were prepared for each of the Eta forecasts in the UC Davis archive (consisting of forecasts from 0 to 48 hours in the future, initialized at 0:00 and 12:00 GMT)

	Wind Speed [m/s]		Power Production [% Wind Farm Cap.]		Obs.
	ME	MAE	ME	MAE	
All Data	-0.05	2.96	-0.46	18.0	12813
Power < 20%	0.84	2.53	8.33	10.6	7632
20% < Power < 80%	-0.78	3.26	-6.56	29.5	3293
Power > 80%	-2.38	4.22	-25.33	28.1	1888

Comparison of Matching Method to Persistence

The matching method was used to forecast four parameters for the Altamont Pass wind farm: power production for the entire Altamont farm and for the Met 127 cluster, plus the wind speeds at Met 438 and Met 127. The matching forecast MAE also is dependent on the forecast interval. For forecast intervals of less than six hours, the persistence method outperforms the matching method. However, as shown in Figure 5-4, the matching power forecasts generally have lower MAEs during the important 24- to 48-hour “next-day” interval. A comparison with persistence for the period between Nov. 20, 2002, and July 31, 2004 showed that the matching method exhibited roughly similar accuracy.

Confidence Interval Estimation

An unsuccessful attempt was made to develop a forecast confidence interval, or uncertainty, based on the standard deviation of the forecast variable in the 25 closest matching historical forecasts. As shown in Figure 5-5, there was essentially no correlation between the standard deviations of the wind speed or power variables in the 25 lowest scoring forecasts and the actual mean absolute errors of the forecast.

Comparison of Different Matching Variables

The use of different combinations of matching variables was examined. The original Eta forecasting algorithm used 19 variables: U and V components of wind speed, temperature and pressure height at 1000 mb, 900 mb, 800 mb, and 700 mb, plus sea level corrected atmospheric

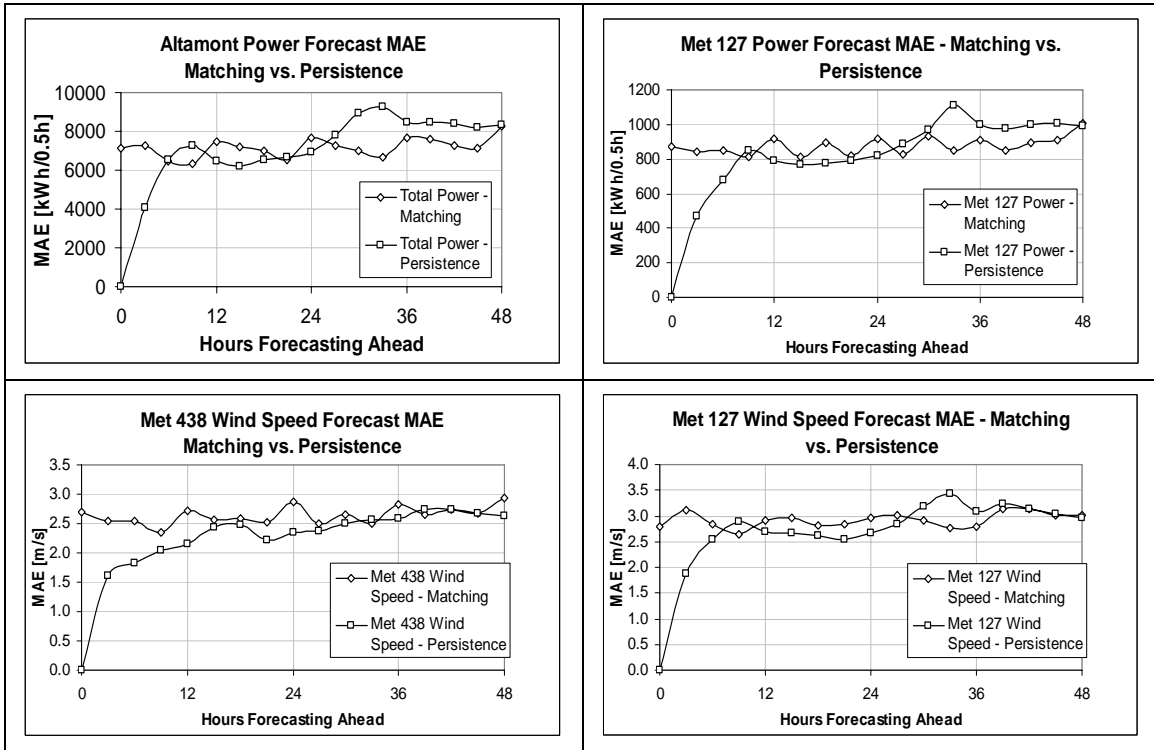


Figure 5-5 Mean absolute errors of match and persistence forecasts as functions of forecast interval. Forecasts were performed for the period, Nov. 30, 2002, and July 31, 2004. Results include forecasts of the power production of the entire wind farm (upper left), forecasts for the Met 127 turbine cluster (upper right), and forecast wind speeds at the Met 438 (lower left) and Met 127 (lower right) meteorological towers.

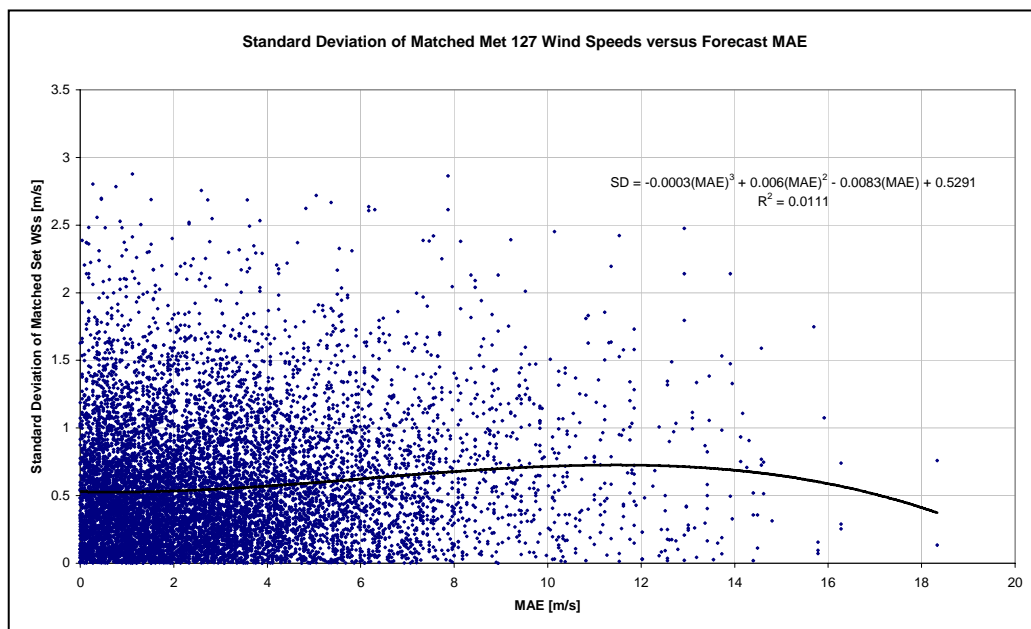


Figure 5-6 Comparison of Met 127 wind speed forecast MAE versus the standard deviation of the Met 127 wind speed in the 25 closest matching historical forecasts.

Table 5-3 ME and MAE of Eta matching forecasts using different combinations of matching Eta variables, compared with persistence forecasting.

Variables Used	Number of Variables	ME 127 WS [m/s]	ME 127 Pwr [%]	ME Tot Pwr [%]	ME 438 WS [m/s]	MAE 127 WS [m/s]	MAE 127 Pwr [%]	MAE Tot Pwr [%]	MAE 438 WS [m/s]
Persistence	N/A	-0.15	-0.40	-0.92	0.10	2.85	17.5	14.9	2.39
All (Baseline Case)	19	-0.09	-0.93	-0.63	-0.15	2.91	17.8	14.5	2.67
Press and 1000	7	-0.06	-0.22	-0.14	-0.14	3.04	18.6	14.9	2.67
Press and Tmp	7	0.04	-0.36	-0.30	-0.08	3.10	19.0	15.6	2.86
All But WS	11	0.03	-0.07	-0.15	-0.09	3.13	19.0	15.6	2.86
WS Only	8	-0.13	-1.28	-0.85	-0.13	3.22	20.5	16.3	2.80
Press and Hgt	7	0.03	0.00	-0.02	-0.05	3.31	20.7	16.9	2.96
WS 700 and WS 1000	4	-0.08	-0.56	-0.38	-0.10	3.41	21.7	17.7	2.92
Press and 700	7	-0.05	-1.05	-0.91	-0.13	3.40	22.3	17.8	3.00
Press Only	3	0.06	0.16	0.19	0.01	3.53	23.5	18.8	3.14
WS 1000	2	-0.03	-0.28	-0.20	-0.04	3.54	23.3	18.8	2.99
WS 700	2	-0.02	-0.12	-0.18	-0.01	4.54	32.5	27.3	3.74

pressure and the X and Y components of the pressure gradient (as returned by the bicubic interpolation).

Times-Series Matching

A second application of the matching method was tested, this time using only a historical database of the variable to be forecast. The idea was to see if a matching approach could improve on persistence. The four days leading up to the time to start forecasting from were compared, on a daily interval, to four day sets of data taken from a large set of historical data during the period, July 1, 2001, to June 30, 2004. Equation 5.3 was used to calculate a matching score for each possible set of data in the historical dataset, with the lowest scoring data set being taken as the "match." The four days of data following the matched data set were then used as the forecast of the variable of interest from 0 to 96 hours in advance.

The method was tested by producing daily forecasts of Altamont total power, up to 96 hours ahead, for three years (July 2001 to June 2004) of Altamont data, using the same data set as the source for the matching files. As in the Eta matching, the closest four days of data were excluded from matching for each individual forecast. Since Altamont wind farm data is provided daily, with a full day of data (0:00 to 23:30) being reported, each forecast started at 0:00 PST. For comparison, corresponding persistence forecasts also were produced, using the last known power production before the start of each forecast (i.e. the power production at 23:30 on the day before the forecast). Figure 5-6 presents the resulting MAEs of the persistence and time-series matching forecasts of power production s. forecast interval.

Comparison to Other Forecasting Methods

Previously, Risoe National Laboratory of Denmark, and AWS Truewind, produced energy generation forecasts for the same Altamont Pass facility over a one-year period ending

September 2002 (EPRI, 2003). A series of match forecasts was performed to be as comparable as possible to these previous forecasts, and each forecast covered a one-year period. The Eta forecast database contained 16,882 individual forecasts collected between December 2002 and March 2005. Each forecast was for a single time between 0 to 48 hours after initialization time.

Unfortunately, the previous forecasts covered the period October 2001 to September 2002, and it was not possible to generate matching forecasts for the same period. Instead, the matching forecasts were generated for 2004 to evaluate the matching method. Each 2004 forecast in the database was used as the “current” forecast and matched to the most similar forecast in the database. Forecasts within four days of the “current” forecast were excluded from the matching process to prevent matching two forecasts of the same meteorological events.

Figure 5-7 shows the matching forecast mean absolute error (MAE) as a percentage of the wind farm capacity for the matching method and persistence forecasts, versus the wind speed recorded at a nearby meteorological tower. Interestingly, MAE for both methods is highly dependent on wind speed, and increases significantly with wind speed. (The variability of MAE at high winds is due to the small number of times those high winds occurred.) Performance also varies significantly depending on the time of year. During the winter months when turbines are often idle for days or weeks at a time, MAE was low for both methods, with persistence outperforming matching forecasts (Figure 5-8). During several summer months, when power production is

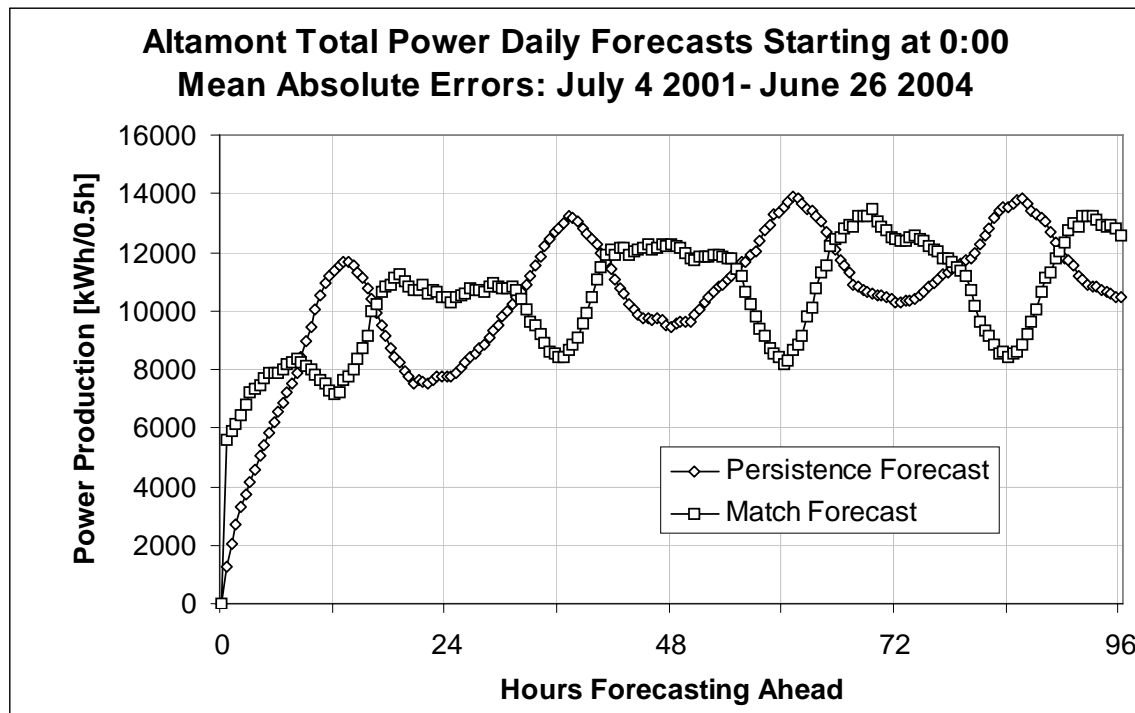


Figure 5-7 Mean absolute error of time-series matching and persistence forecasts of total Altamont power production between July 2001 and June 2004. All forecasts start at 0:00 local time and forecast out to 96 hours in the future.

highest at Altamont, the MAE was well above 20% rated capacity for both methods, with match forecasting outperforming persistence.

The energy forecast MAE also is dependent on the forecast interval (Figure 5-9). For forecast intervals of less than six hours, the persistence method outperforms the matching method. However, as shown below, the matching forecast has lower MAEs in the important 24- to 48-hour “next-day” interval. Therefore, it appears that the match forecast is of most value for predicting next-day power production during the higher power producing summer periods.

Table 5-4 presents the overall MAE results of the two previous forecasting studies, the match forecast, and persistence forecasts. Skill score (S) is defined as $S = 1 - MAE_f / MAE_p$, where MAE_f is the MAE of the trial forecast method and MAE_p is the MAE for persistence forecasts during the same time period. The match forecasting was less accurate than the more sophisticated methods but more accurate than persistence.

Table 5-4 Mean absolute error(MAE) as a percentage of observed wind farm capacity for four different forecast methods at the Altamont Pass wind farm. Skill score is percentage improvement in MAE relative to persistence.

Forecast *Oct. 2001 – Sept. 2002 **Jan. – Dec. 2004	MAE [% Cap.]	Skill Score vs. Persistence
Risø*	14.4	21.6%
TrueWind*	13.8	30.8%
Matching**	16.2	7.1%
Persistence**	17.4	0.0%

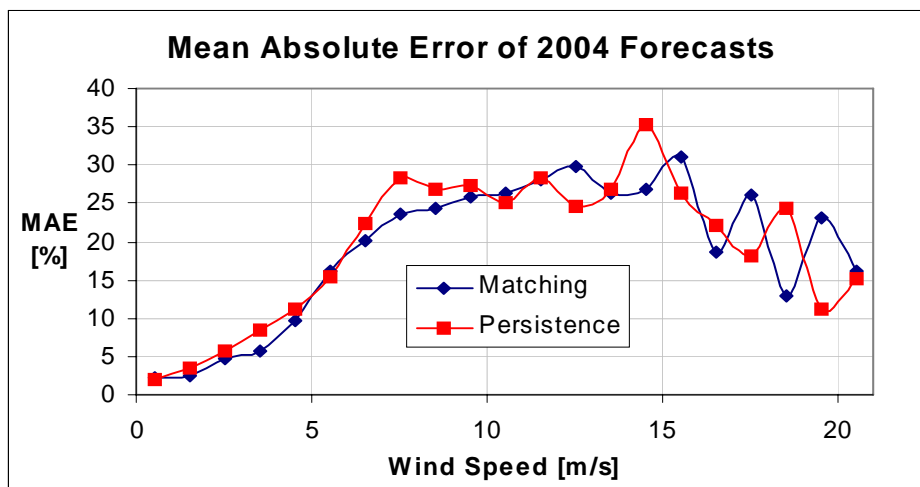


Figure 5-8 Mean absolute error (MAE) of the match and persistence forecasts as a function of wind speed. January 1 to December 31, 2004.

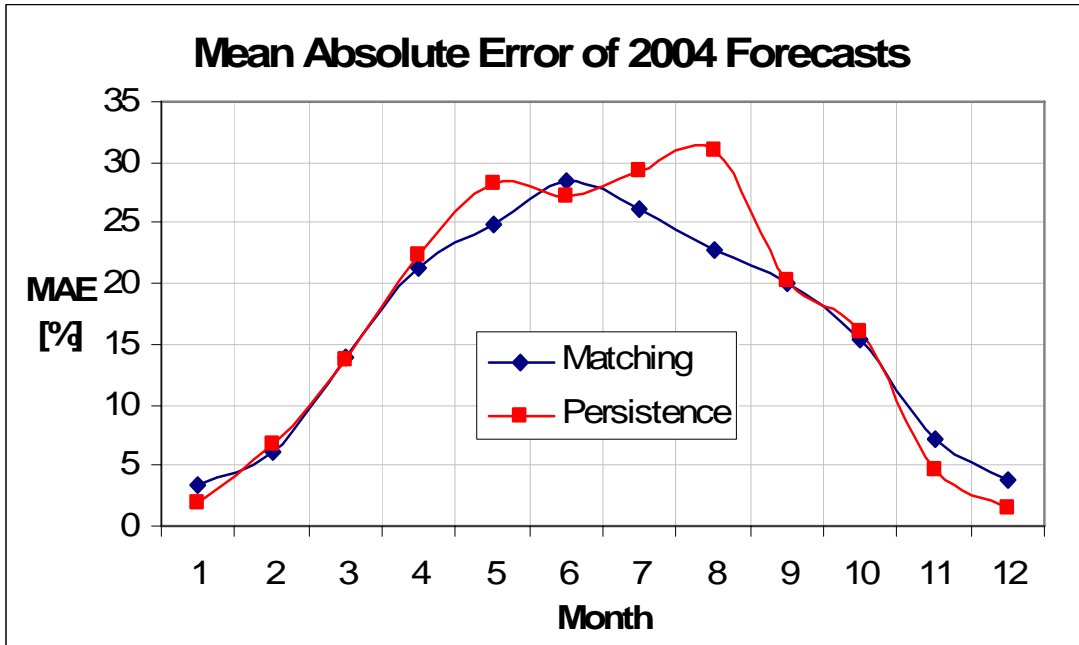


Figure 5-9 Mean absolute error (MAE) of the match and persistence forecasts as a function of month for the period January 1 to December 31, 2004.

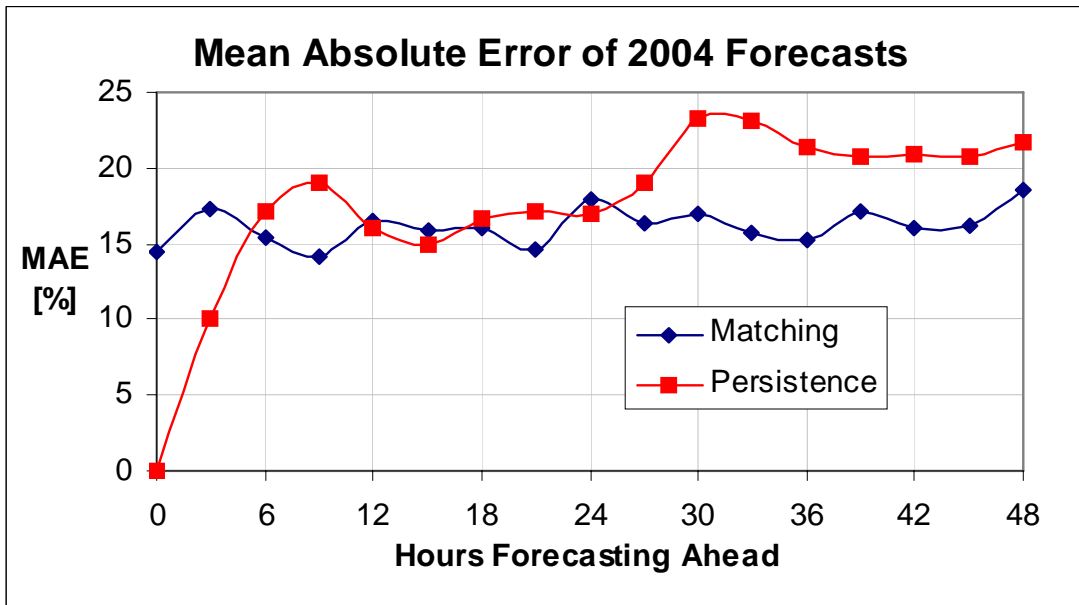


Figure 5-10 Mean absolute error (MAE) of the match and persistence forecasts as a function of wind speed. January 1 to December 31, 2004.

Effect of Database Size

The most significant factors in match forecasting accuracy are the number of parameters matched (as discussed earlier) and the size of the matching database. For evaluation purposes, two different database sizes were used to “diagnostically” match forecast the period from November 30, 2002, to July 31, 2004. The “small database” consisted of 10,427 archived forecasts within this time frame, while the “large database” contained the entire small database, plus an additional 8100 forecasts between August 1, 2004, and June 10, 2005. Persistence forecasts were also generated for the same time period. Mean and mean absolute errors and skill scores were calculated for all three forecast methods. The skill score is the percentage improvement of a forecast method relative to persistence.

Table 5-5 presents the results for the entire forecast set. The results in Table 5-5 include all forecasts, from initialization (“nowcasts”) to 48 hours in advance.

The high skill scores for temperature and humidity are due to the strongly diurnal nature of these parameters, which is not well predicted by a persistence forecast at non-24-hour forecast intervals (Figure 5-10). For wind speed and power production, the large database match forecast generally performs better than the small database. Interestingly, power production match forecasts appear to be more skillful than those for wind speed, at least partially due to the broad range of meteorological conditions that result in zero power production.

Since persistence performs well for forecasts less than six hours in advance, while next day performance is the goal here, the forecast performance is next determined as a function of forecast interval. Figures 5-11 and 5-12 present the forecast MAE as a function of forecast interval for wind speed and power production, respectively.

Table 5-5 Overall performance of small and large database matching forecasts relative to persistence for six parameters.

Forecasted Parameter	Persistence		Small Database			Large Database		
	ME	MAE	ME	MAE	S (%)	ME	MAE	S (%)
Met 127 Wind Speed (m/s)	-0.13	2.85	-0.09	2.91	-2.26	-0.08	2.83	0.73
Met 438 Wind Speed (m/s)	0.08	2.44	-0.15	2.67	-9.48	-0.26	2.66	-8.79
Met 127 Power (% Cap.)	-0.16	17.40	-0.93	17.75	-2.04	-1.51	17.15	1.42
Total Power (% Cap.)	-0.77	16.25	-0.70	16.16	0.59	-1.18	15.47	4.86
Met 438 Relative Humidity (%)	-2.35	18.35	0.52	16.76	8.63	1.88	16.01	12.72
Met 438 Temperature (K)	0.68	4.37	-0.04	2.92	33.30	-0.10	2.81	35.81

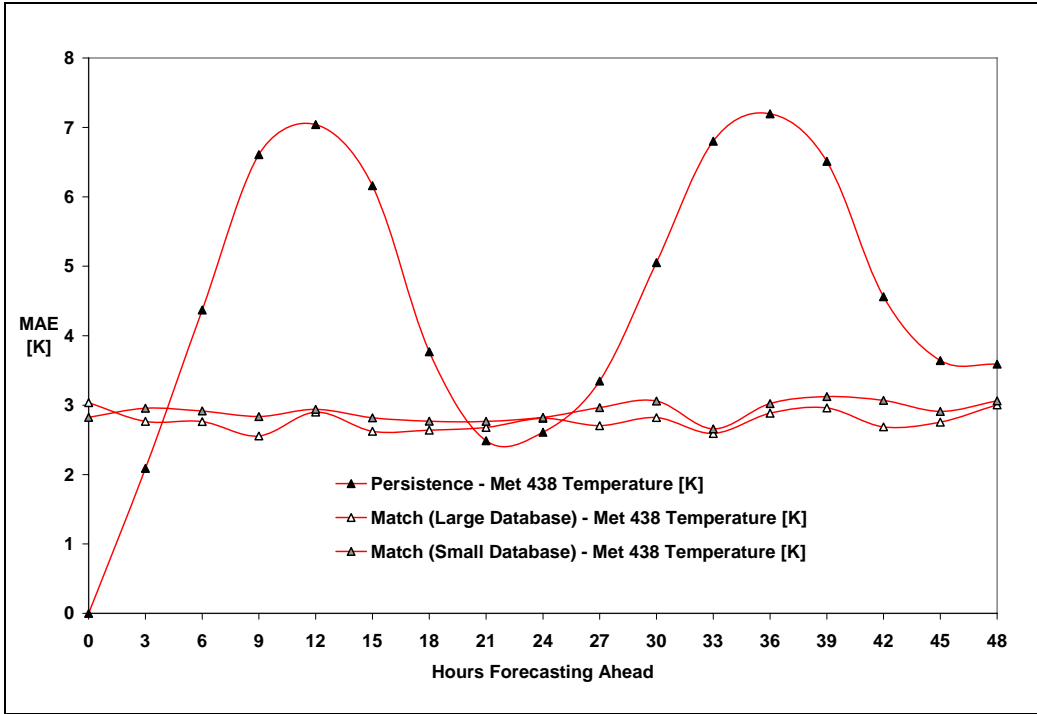


Figure 5-11 Mean absolute error (MAE) versus forecast interval for persistence, small database match and large database match temperature forecasts. Forecast period is November 30, 2002, to July 31, 2004.

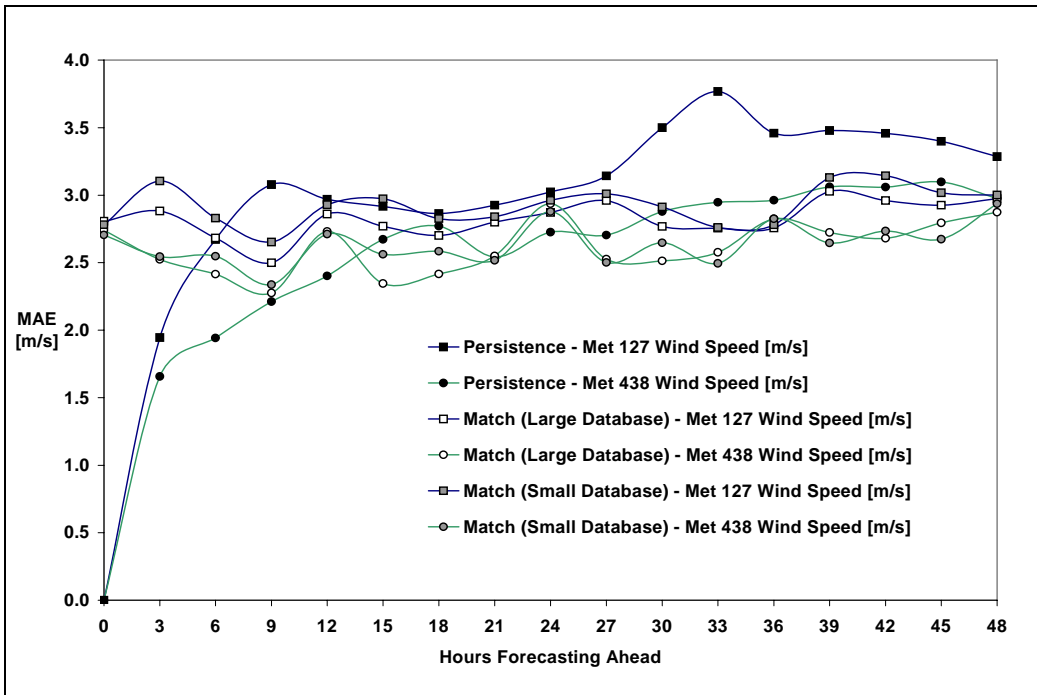


Figure 5-12 Mean absolute error (MAE) versus forecast interval for persistence, small database match and large database match wind speed forecasts. Forecast period is November 30, 2002, to July 31, 2004.

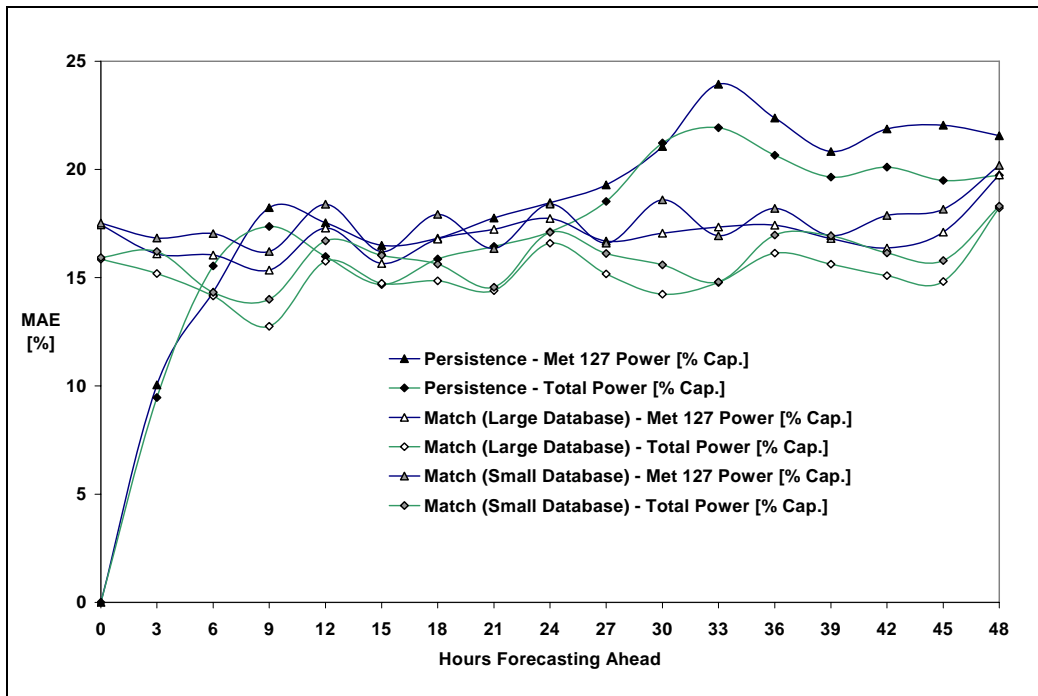


Figure 5-13 Mean absolute error (MAE) versus forecast interval for persistence, small database match and large database match power production forecasts. Forecast period is November 30, 2002, to July 31, 2004.

For the 24- to 48-hour power production forecasts, the match method generally outperforms persistence, with the large database providing better results than the small database. Forecasts of power production seem to benefit most from a large database matching method, while the forecasts of meteorological parameters are less sensitive to the database size at this scale.

Matching Using Different Input Regional Scale Forecasts

The performance of match forecasting using different RSFs was evaluated by forecasting the same time period (June 1, 2004, to May 31, 2005) using databases generated by three forecast models, including the 40-km Eta model and two resolutions of the COAMPS model (12-km and 4-km) provided by the National Atmospheric Release Advisory Center (NARAC) at Lawrence Livermore National Laboratory (LLNL).

For each RSF, an equivalent historical forecast database was compiled. The COAMPS model output was provided hourly, while Eta was available only every third hour. For consistency, only COAMPS forecasts from every third hour (corresponding to the hours available for Eta) were used in the forecast database. Similarly, all results presented below consider only match forecasts for every third hour. Nineteen matching variables were used to calculate the similarity score. For Eta, the same variables were used as described in the previous sections. For COAMPS, the analogous variables were taken from the four levels closest to 1000, 900, 800, and 700 mb (Levels 9, 17, 19, and 21). As in the previous investigations, a forecast was generated for each

forecast in the historical database, and the closest four days were excluded from matching to prevent matching of the same weather phenomenon as in the current forecast. Table 5-6 shows the overall error levels for each forecast for several parameters. Power production values are normalized by the appropriate observed wind farm capacity (10 MW for Met 127, 100 MW for Total).

Interestingly, for the six variables considered, the best overall performance was achieved using the low resolution Eta model, followed by the 12-km COAMPS model. It is postulated that for this forecasting method, higher spatial resolution may result in a decrease in accuracy due to the ability of the model to forecast a wider range of variability in local conditions. It is believed that the relatively poor performance of all the match forecasts compared to persistence is due to the small (one year) size of the historical databases used for matching.

Table 5-6 Overall mean error (ME) and mean absolute error (MAE) of match forecasts of several Altamont Pass wind power and meteorological parameters between June 1, 2004, and May 31, 2005. Match forecasts were generated using data from three regional scale forecasts: 40-km Eta, 12-km COAMPS and 4-km COAMPS. Results for persistence forecast are shown for comparison. Total power forecasts are the combined power production of all 11 Powerworks turbine clusters.

Parameter	40 km Eta	12 km COAMPS	4 km COAMPS	Persistence
ME - Met 127 Wind Speed [m/s]	-0.01	0.00	0.02	0.04
ME - Met 438 Wind Speed [m/s]	0.10	0.10	-0.07	0.25
ME - Met 127 Power [% Cap.]	0.33	0.20	0.61	0.08
ME - Total Power [% Cap.]	0.35	0.27	0.29	-0.27
ME - Met 438 Temp [K]	0.06	0.39	0.31	0.77
ME - Met 438 Rel. Humidity [%]	1.38	-0.18	0.36	-2.43
MAE - Met 127 Wind Speed [m/s]	2.95	3.17	3.11	3.20
MAE - Met 438 Wind Speed [m/s]	2.89	2.91	2.83	2.57
MAE - Met 127 Power [% Cap.]	17.48	19.46	20.48	18.03
MAE - Total Power [% Cap.]	13.46	15.77	16.78	14.96
MAE - Met 438 Temp [K]	2.92	3.37	2.89	4.27
MAE - Met 438 Rel. Humidity [%]	15.65	16.80	15.41	18.43

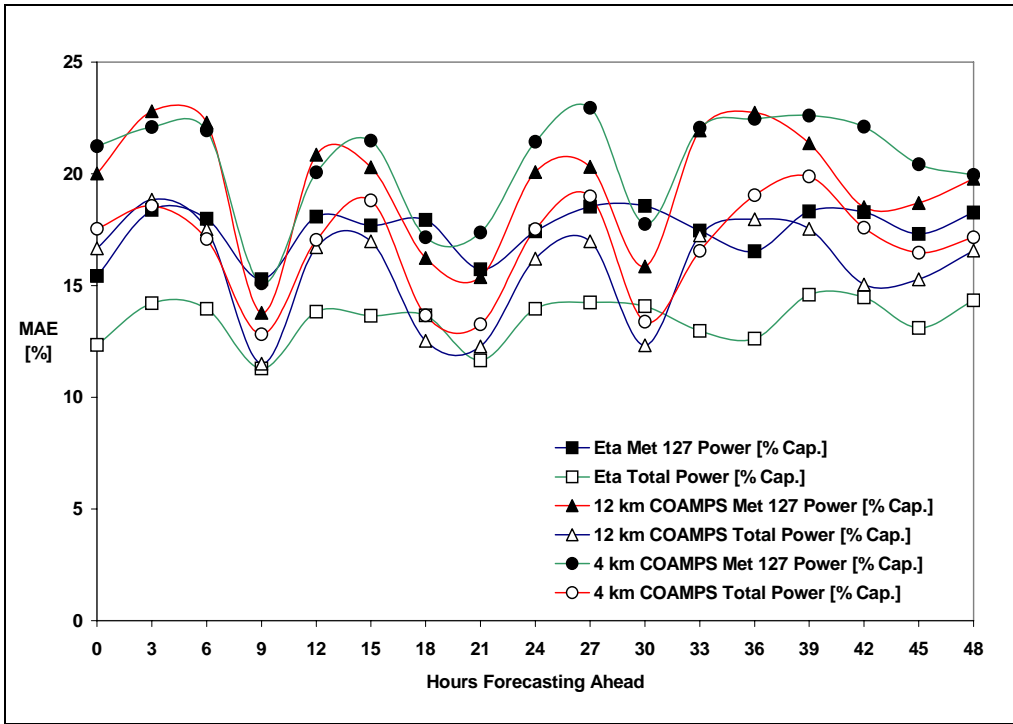


Figure 5-14 Mean absolute errors of the Eta- and COAMPS-based power production match forecasts as functions of the forecast interval during the period, June 1, 2004, to May 31, 2005.

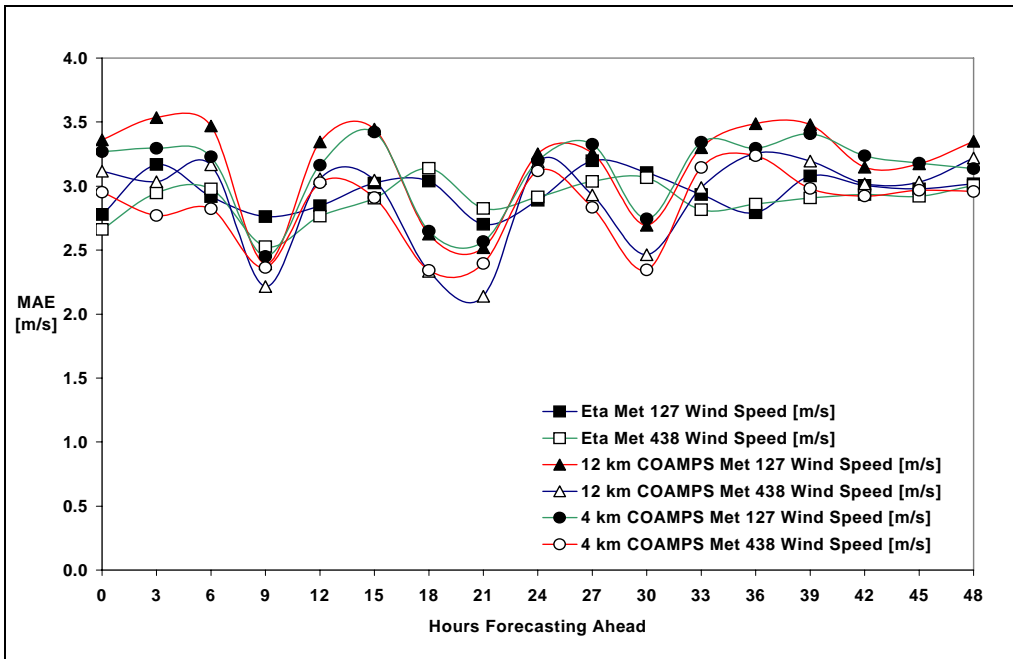


Figure 5-15 Mean absolute errors of the Eta- and COAMPS-based wind speed match forecasts as functions of the forecast interval during the period June 1, 2004, to May 31, 2005.

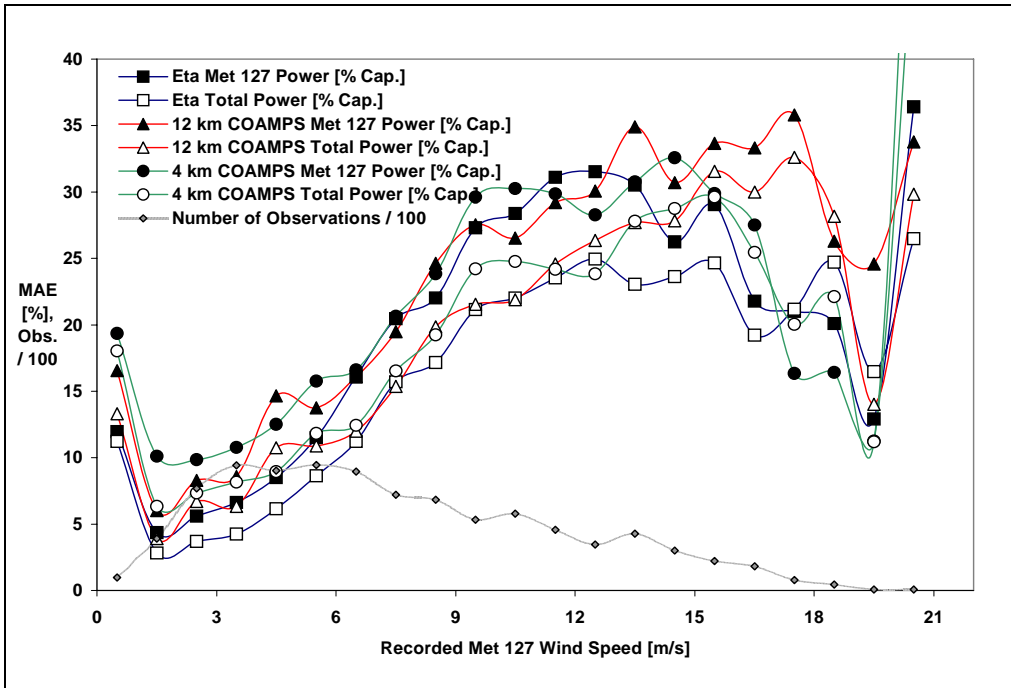


Figure 5-16 Mean absolute errors of the Eta- and COAMPS-based power production match forecasts as functions of the Met 127 observed wind speed during the period, June 1, 2004, to May 31, 2005. The chart also shows the number of observations in each 1 m/s wind- speed bin.

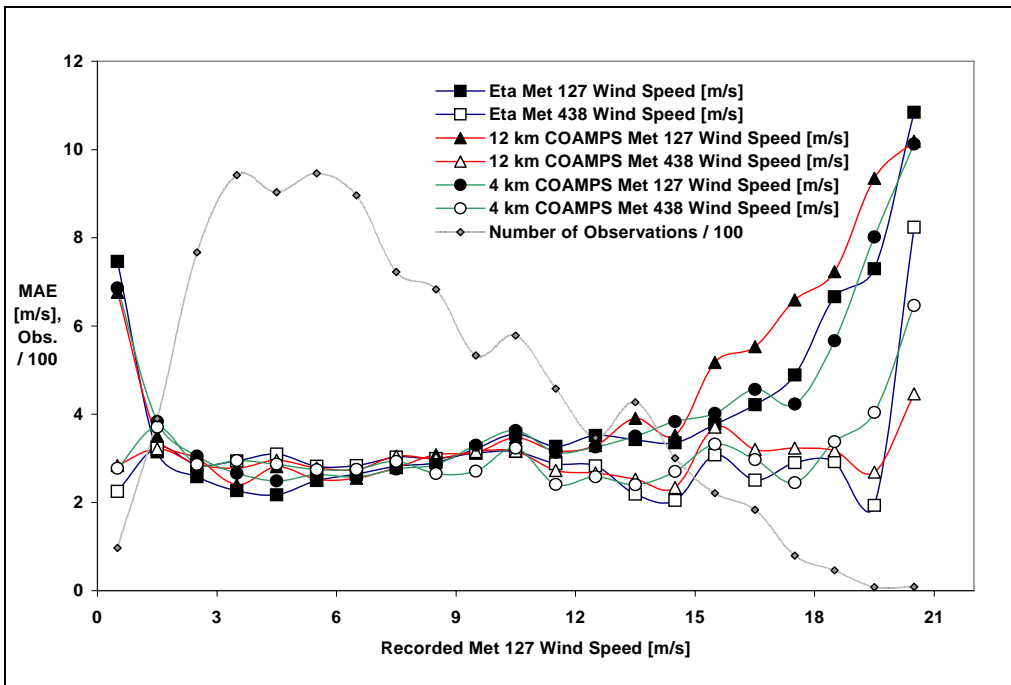


Figure 5-17 Mean absolute errors of the Eta- and COAMPS-based wind speed match forecasts as functions of the Met 127 observed wind speed during the period, June 1, 2004, to May 31, 2005. The chart also shows the number of observations for each 1 m/s wind speed bin.

6

CONCLUSIONS

The goal of the wide range of research conducted at UC Davis was to find methods of improving wind power forecasting, especially through the use of non-computationally intensive methods.

A wind farm power curve based on wind tunnel data was developed. This power curve featured several refinements of the wind tunnel power curve developed by Cheng (2002), including wind direction and air density as additional inputs. Slight improvement, as measured in wind power prediction mean absolute error (MAE), was observed over the results of Cheng. Evaluation of the new power curve was hampered by the fact that power producing winds at the Altamont Pass study site come primarily from the southwest, and the wind direction measurements from the study site did not appear to be reliable for significant portions of the study time period. Power prediction MAEs of 5 to 7 percent were observed for the new power curve, depending on the year and duration of the evaluation period.

Estimating wind speed at specific times for specific turbine locations in complex terrain using “speed-up” prediction methods did not yield sufficient accuracy for use in operational wind power forecasting. An alternate approach to the “empirical” power curve method was developed based on simulating potential flow over laterally weighted two-dimensional transects of the wind farm terrain. This method proved capable of making power predictions based on meteorological tower wind speed and direction almost as accurately as the wind tunnel method, without requiring construction of a large physical model of the wind farm terrain. It also required only a small amount of computational resources and could be applied to any location for which digital elevation data is available. When forecasted wind data provided by Truewind was used, both the empirical and wind tunnel-based power curves were found to produce forecasts with similar MAEs to the Truewind power forecasts.

Several methods of downscaling from regional scale forecast (RSF) model output to a near-surface location were investigated. The geostrophic drag law and multiple linear regression were not sufficiently accurate to be of use. A forecasting method based on finding (“matching”) past RSFs in a database of historical forecasts that are similar to the current RSF was found to be more successful. The number of matched RSF variables and the time period covered by the database were determined to be the most significant factors in forecasting performance. The “matching” method was found to be capable of out-performing a persistence forecast when applied to the Powerworks sites at the Altamont Pass, with mean absolute errors decreasing as the size of the matching database was increased. It was also observed that the use of a higher resolution RSF (as tested using two resolutions of the COAMPS model) did not result in lower MAEs with the matching method, when used for wind speed or power production forecasts.

7

REFERENCES

1. American Wind Energy Association, “Wind Project Database: California,” Washington, D.C., <http://www.awea.org/projects/california.html>, April 2006.
2. Baker, C. J., “The Determination of Topographical Exposure Factors for Railway Embankments,” J. Wind Engineering and Ind. Aerodynamics, (21) 1985, pp. 89 – 99.
3. Barnard, J., Wegley, H., Hiester, T. “Improving the Performance of Mass-Consistent Numerical Models Using Optimization Techniques.” J. of Climate and Applied Meteorology, Vol. 26, no. 6, pp. 675-686. 1987.
4. Black, T. Meteorologist, Mesoscale Modeling Branch, NOAA. Personal communication Sept. 23, 2003.
5. Bowen, A. J. “Modelling of Strong Wind Flow Over Complex Terrain at Small Geometric Scales.” J. Wind Engineering and Industrial Aerodynamics. Vol. 91, pp. 1859-1871. 2003.
6. Bowen, A., Lindley, D. “A Wind Tunnel Investigation of the Wind Speed and Turbulence Characteristics Close to the Ground Over Various Escarpment Shapes.” Boundary-Layer Meteorology. Vol. 12, pp. 259-271. 1977.
7. Brown, A., Watt, J. “The Design and Construction of 25 MW Wind Farm.” Journal of Wind Engineering and Industrial Aerodynamics, Vol. 27, no. 1-3, pp. 319-325. 1988.
8. Burda, T., Wilson, J., Hiester, T., Germain, A. “Significance of Upper Air Meteorological Conditions in Altamont Pass Wind Resource Assessment.” AWEA Windpower '85 Conference Proceedings. San Francisco, CA, USA. Aug. 27-30, 1985.
9. Carpenter, P., Locke, N. “Investigation of Wind Speeds Over Multiple Two-Dimensional Hills.” J. Wind Eng. & Ind. Aero. Vol. 83, pp. 109-120. 1999.
10. Cermak, J. E. “Wind Tunnel Development and Trends in Applications to Civil Engineering.” J. Wind Eng. and Industrial Aerodynamics, Vol. 91, pp. 355-370. 2003.
11. Chapman, R. K. and Gouveia, F. J., *Building III Wind Flow Study: July 1987*, Lawrence Livermore National Laboratory, Livermore, California, 1987.
12. Cheng, J., Wind Energy Forecasting of a Wind Turbine Farm in the Altamont Pass Through Wind Tunnel Modeling. Master of Science Thesis, University of California, Davis, 2002.

References

13. Counihan, J., "Adiabatic Atmospheric Boundary Layer: A Review and Analysis of Data From the Period 1880-1972," *Atmos. Env.*, Vol. 9, no. 10, pp. 871-905, 1975.
14. Davis, E., Nierenberg, R. *Wind Prospecting in Alameda and Solano Counties: Volume 1*. Pacific Gas and Electric Company. Consultant Report to California Energy Commission (P500-80-054). May 1980.
15. Deaves, D. "Computations of Wind Flow Changes Over Two-Dimensional Hills and Embankments." *J. Wind Eng. And Ind. Aero.*, Vol. 6, pp. 89-112. 1980.
16. Derickson, R. G., Peterka, J. A. Development of a Powerful Hybrid Tool for Evaluating Wind Power in Complex Terrain: Atmospheric Numerical Models and Wind Tunnels. AIAA Paper No. 2004-1005. Proceedings of AIAA/ASME Wind Energy Symposium 2004. Reno, NV, USA. Jan. 2004.
17. California Energy Commission (Energy Commission) and Electric Power Research Institute (EPRI), 2003a: *California Wind Energy Forecasting System Development and Testing Phase 1: Initial Testing*. EPRI Palo Alto, CA, California Energy Commission, Sacramento, CA: 2003. 1003778.
18. California Energy Commission (Energy Commission) and Electric Power Research Institute (EPRI), 2003b: *California Wind Energy Forecasting System Development and Testing Phase 2: 12-Month Testing*. EPRI Palo Alto, CA, California Energy Commission, Sacramento, CA: 2003. 1003779.
19. California Energy Commission (Energy Commission) and Electric Power Research Institute (EPRI), 2006a: *California Regional Wind Energy Forecasting System Development, Volume 1: Executive Summary*. EPRI Palo Alto, CA, California Energy Commission, Sacramento, CA: 2006. 1013262.
20. California Energy Commission (Energy Commission) and Electric Power Research Institute (EPRI), 2006b: *California Regional Wind Energy Forecasting System Development, Volume 2: Wind Energy Forecasting System Development and Testing and Numerical Modeling of Wind Flow over Complex Terrain*, EPRI Palo Alto, CA' California Energy Commission, Sacramento, CA: 2006. 1013263.
21. California Energy Commission (Energy Commission) and Electric Power Research Institute (EPRI), 2006c: *California Regional Wind Energy Forecasting System Development, Volume 3: Wind Tunnel Modeling of Wind Flow over Complex Terrain*. EPRI Palo Alto, CA, California Energy Commission, Sacramento, CA: 2006. 1013264.
22. California Energy Commission (Energy Commission) and Electric Power Research Institute (EPRI), 2006d: *California Regional Wind Energy Forecasting System Development, Volume 4: California Wind Generation Research Dataset (CARD)*. EPRI Palo Alto, CA, California Energy Commission, Sacramento, CA: 2006. 1013265.
23. EPRI, 2003: *Wind Energy Forecasting Applications in Texas and California: EPRI - California Energy Commission - U.S. Department of Energy Wind Energy Forecasting Program*, Electric Power Research Institute, Palo Alto, CA: 2003. 1004038.

24. Engineering Sciences Data Unit. Strong Winds in the Atmospheric Boundary Layer Part 1: Mean-Hourly Wind Speeds. ESDU Publication 82026, March 1990.
25. Federal Aviation Administration. Siting Guidelines for Low Level Wind Shear Alert System (LLWAS) Remote Facilities. FAA Publication 6560.21, Feb. 1988.
26. Finnigan, J. J. Air Flow Over Complex Terrain. In: Flow and Transport in the Natural Environment: Advances and Applications, Steffen W. L. and Denmead, O. T., Eds. pp. 183-299. Springer-Verlag. 1988.
27. Gong, W., Ibbetson, A. A “Wind Tunnel Study of Turbulent Flow Over Model Hills.” Boundary-Layer Meteorology. Vol. 49, pp. 113-148. 1989.
28. Holets, S. H. “Wind Speed Variability in the California Altamont Pass Area.” AWEA Windpower '85 Conference Proceedings, pp. 411-416. San Francisco, CA, USA, Aug. 27-30, 1985.
29. Hunt, J. C. R., Leibovich, S., Richards, K. J. “Turbulent Shear Flow Over Low Hills.” Quarterly Journal of the Royal Meteorological Society. Vol. 114, pp. 1435-1470. 1988.
30. Jackson, P. S., Hunt, J. C. R. “Turbulent Wind Flow Over a Low Hill.” Quarterly Journal of the Royal Meteorological Society. 1975. Vol. 101, pp. 929-955.
31. Jensen, M., “The Model-Law for Phenomena in a Natural Wind,” Ingenioren, Int. Ed., Vol. 2, no. 4, 1958.
32. Kaimal, J., Finnigan, J. “Atmospheric Boundary Layer Flows – Their Structure and Measurement.” 1994. Oxford University Press.
33. Kim, H. G., Lee, C. M., Lim, H. C., Kyong, N. H. “An Experimental and Numerical Study on the Flow Over Two-Dimensional Hills.” Journal of Wind Engineering and Industrial Aerodynamics. 1997. Vol. 66, pp. 17-33.
34. Kim, H. G., Patel, V. C., Lee, C. M. “Numerical Simulation of Wind Flow Over Hilly Terrain.” Journal of Wind Engineering and Industrial Aerodynamics. 2000. Vol. 87, pp. 45-60.
35. Landberg, L., Watson, S. J. “Short-Term Prediction of Local Wind Conditions.” Boundary-Layer Meteorology. Vol. 70, pp. 171-195. 1994.
36. Lange, B., and Hojstrup, J. “Evaluation of the Wind-Resource Estimation Program WAsP for Offshore Applications.” Journal of Wind Engineering and Industrial Aerodynamics. 2001. pp. 271-291.
37. Lemelin, D., Surry, D., Davenport, A. “Simple Approximations for Wind Speed-Up Over Hills.” J. Wind Eng. And Ind. Aero. Vol. 28, pp. 117-127. 1988.

References

38. Lindley, D., Neal, D., Pearse, J. R., Stevenson, D. C. The Effects of Terrain and Construction Method on the Flow Over Complex Terrain Models in a Simulated Atmospheric Boundary Layer. Proceedings of the Third British Wind Energy Association Wind Energy Conference, pp. 195-211. Cranfield, U.K. April, 1981.
39. Mason, P., Sykes, R. “Flow Over an Isolated Hill of Moderate Slope.” Quarterly Journal of the Royal Meteorological Society. Vol. 105, pp. 383-395. 1979.
40. McCarthy, E. F. *Stably Stratified Flow in Altamont Pass.* U.S. Windpower, Inc. May 15, 1987. Personal communication.
41. McCarthy, E. F. “Wind Speed Forecasting in the Central California Wind Resource Area.” AWEA Windpower '97 Conference Proceedings. Austin, TX, USA. June 15-18, 1997.
42. Miller, C. A., and Davenport, A. G. “Guidelines for the Calculation of Wind Speed-Ups in Complex Terrain. 1998.” Journal of Wind Engineering and Industrial Aerodynamics. Vol. 74-76. pp. 189-197.
43. Nierenberg, R. D. *Macro-Scale Wake Effects.* AWEA Windpower '89 Conference Proceedings, pp. 14-19. San Francisco, CA, USA, Sept. 24-27, 1989.
44. Schlichting, H. *Boundary-Layer Theory.* 7th Ed. McGraw-Hill. 1979.
45. Taylor, G. J., Smith, D. Wake Measurements Over Complex Terrain. Proceedings of the 13th BWEA Conference: Wind Energy Conversion 1991. Swansea, UK, Apr. 10-12, 1991.
46. Taylor, P. A. “Turbulent Boundary-Layer Flow Over Low and Moderate Slope Hills.” Journal of Wind Engineering and Industrial Aerodynamics. 1998. Vol. 74-76. pp. 25-47.
47. Taylor, P. A., Teunissen, H. W. “The Askervein Hill Project – Overview and Background Data.” Boundary-Layer Meteorology. 1987. Vol. 39 (1-2), pp. 15-39.
48. Weng, W., Taylor, P. A., Walmsley, J. L. “Guidelines for Airflow Over Complex Terrain: Model Developments.” Journal of Wind Engineering and Industrial Aerodynamics. 2000. Vol. 86. pp. 169-186.
49. White, B.R. and Cheng, J. Wind Tunnel Forecasting of a Wind Turbine Farm in the Altamont Pass Through Wind Tunnel Testing, Final Report EPRI Contract EP-P2101/C924. 2002.
50. Wilks, D. S. “Statistical Methods in the Atmospheric Sciences.” Academic Press,1995.

A

APPENDIX - MET 127 R VALUES DETERMINED BY ABLWT AND POTENTIAL FLOW SIMULATIONS

"R values" were calculated for each turbine in the Met 127 turbine cluster. In the Atmospheric Boundary Layer Wind Tunnel (ABLWT) tests, R denotes a dimensionless mean wind speed, defined as the wind speed at a measurement point divided by a reference wind speed. In this instance,

$$R = \frac{U_{\text{turb,tunnel}}}{U_{\text{met,tunnel}}}$$

where $U_{\text{turb,tunnel}}$ is defined as the hub-height mean wind speed at a turbine location on the wind tunnel model, and $U_{\text{met,tunnel}}$ is the mean anemometer-height mean wind speed measured in the wind tunnel at met tower 127.

Table A-1 presents the wind speed ratios calculated using both the Potential10 flow model and ABLWT measurements of the wind speed ratio between each wind turbine and the reference met-tower location. Four values are calculated for each method, one for each wind direction, 60°, 150°, 240° and 330°.

Table A-2 presents the differences between the Potential10 model and ABLWT measurements of the wind speed ratios for each turbine.

Table A-1 Potential10 and ABLWT Wind Speed Ratios (R)

Potential10 R Values (U _{turb} /U _{met}) (Fill = 0.12)					ABLWT R Values using (U _{turb} /U _{met})				
	Wind Direction					Wind Direction			
	60	150	240	330		60	150	240	330
Minimum	0.831	0.763	0.840	0.759	Minimum	0.860	0.719	0.769	0.704
Mean	0.953	0.910	0.960	0.913	Mean	0.954	0.913	0.973	0.929
Maximum	1.030	1.041	1.055	1.034	Maximum	1.046	1.004	1.173	1.034
Turbine	Wind Direction				Turbine	Wind Direction			
	60	150	240	330		60	150	240	330
6	1.001	0.988	0.898	1.001	6				
7	1.001	0.911	0.908	0.954	7				
8	0.988	0.839	0.912	0.919	8				
9	0.981	0.802	0.913	0.886	9				
10	0.961	0.839	0.936	0.786	10				
11	0.979	0.917	0.971	0.915	11	0.975	0.962	1.001	0.937
12	1.001	0.957	0.990	0.964	12	0.980	0.970	1.010	0.952
13	1.008	0.986	1.000	0.994	13	0.985	0.978	1.020	0.967
14	1.023	1.009	0.999	1.013	14	0.994	0.991	1.025	0.981
15	1.022	0.995	0.976	1.000	15	1.003	1.004	1.030	0.994
16	1.018	0.947	0.968	0.959	16	0.996	0.973	1.022	0.962
17	1.016	0.914	0.968	0.925	17	0.988	0.942	1.016	0.930
18	1.005	0.877	0.960	0.888	18	0.974	0.914	1.000	0.908
19	0.990	0.838	0.960	0.850	19	0.959	0.886	0.983	0.886
20	0.993	0.878	0.978	0.845	20	0.969	0.888	1.035	0.862
21	1.030	0.938	1.009	0.935	21	0.980	0.890	1.088	0.837
34	0.854	0.867	0.862	0.878	34	0.896	0.906	0.836	0.923
35	0.854	0.873	0.857	0.884	35	0.896	0.898	0.802	0.908
36	0.835	0.863	0.854	0.870	36	0.896	0.891	0.769	0.892
37	0.831	0.845	0.840	0.848	37	0.911	0.900	0.811	0.904
38	0.862	0.900	0.877	0.893	38	0.939	0.942	0.854	0.920
39	0.895	0.951	0.917	0.959	39	0.963	0.972	0.893	0.977
40	0.934	1.009	0.952	1.019	40	0.987	1.002	0.931	1.034
41	0.956	1.041	0.969	1.034	41	0.970	0.993	0.915	1.025
42	0.948	1.011	0.955	0.993	42	0.952	0.985	0.900	1.017
43	0.922	0.963	0.937	0.954	43	0.950	0.953	0.887	0.997
44	0.903	0.930	0.926	0.924	44	0.948	0.922	0.873	0.978
45	0.891	0.879	0.916	0.895	45	0.917	0.851	0.866	0.916
46	0.868	0.796	0.896	0.858	46	0.886	0.781	0.860	0.855
47	0.878	0.763	0.906	0.806	47	0.873	0.781	0.865	0.827
48	0.899	0.806	0.916	0.777	48	0.860	0.781	0.870	0.799
49	0.929	0.848	0.934	0.840	49	0.892	0.829	0.927	0.845
50	0.938	0.890	0.945	0.884	50	0.925	0.877	0.930	0.890
51	0.957	0.928	0.967	0.935	51	0.924	0.880	0.993	0.907
52	0.965	0.942	0.967	0.947	52	0.924	0.884	1.001	0.924
53	0.959	0.918	0.956	0.920	53	0.929	0.870	0.990	0.921
54	0.942	0.867	0.940	0.879	54	0.934	0.856	0.977	0.918
55	0.932	0.818	0.934	0.829	55	0.930	0.835	0.944	0.893
56	0.932	0.794	0.934	0.798	56	0.926	0.814	0.912	0.868
57	0.941	0.831	0.938	0.826	57	0.925	0.849	0.925	0.870
58	0.952	0.876	0.942	0.880	58	0.924	0.883	0.936	0.872
59	0.963	0.908	0.942	0.920	59	0.945	0.874	0.952	0.890
60	0.961	0.874	0.933	0.896	60	0.966	0.864	0.967	0.909
61	0.954	0.810	0.933	0.849	61	0.930	0.872	0.969	0.886
62	0.923	0.769	0.908	0.807	62	0.937	0.823	0.965	0.842
63	0.906	0.808	0.890	0.759	63	0.884	0.719	0.930	0.704
64	0.952	0.954	0.953	0.986	64	0.942	0.978	1.059	0.947
65	0.992	0.984	0.971	1.021	65	0.944	0.990	1.066	0.973
66	0.999	0.986	0.971	1.008	66	0.947	1.002	1.075	0.999

Table A-1 Potential10 and ABLWT Wind Speed Ratios (R) (Cont'd)

Turbine	Wind Direction				Turbine	Wind Direction			
	60	150	240	330		60	150	240	330
67	1.000	0.971	0.973	0.980	67	0.929	0.965	1.046	0.979
68	0.992	0.955	0.970	0.954	68	0.912	0.927	1.016	0.959
69	0.982	0.954	0.970	0.946	69	0.918	0.948	1.016	0.974
70	0.984	0.982	0.973	0.960	70	0.924	0.969	1.016	0.989
71	0.976	0.996	0.973	0.959	71	0.930	0.978	0.971	0.981
72	0.971	0.995	0.969	0.943	72	0.930	0.987	0.928	0.973
73	0.950	0.958	0.965	0.919	73	0.948	0.940	0.884	0.924
74	0.937	0.908	0.954	0.902	74	0.948	0.964	0.861	0.949
75	0.918	0.857	0.945	0.888	75	0.930	0.949	0.841	0.900
76	0.957	0.881	0.964	0.872	76	0.930	0.937	0.862	0.897
77	0.967	0.877	0.949	0.869	77	0.937	0.926	0.862	0.893
78	0.967	0.878	0.931	0.868	78	0.884	0.930	0.862	0.898
79	0.954	0.894	0.923	0.882	79	0.884	0.935	0.862	0.903
80	0.885	0.870	0.941	0.846	80	0.886	0.838	0.958	0.862
81	0.901	0.892	0.961	0.887	81	0.918	0.894	0.969	0.899
82	0.924	0.917	0.979	0.933	82	0.951	0.950	0.979	0.936
83	0.944	0.951	0.995	0.975	83	0.968	0.966	0.988	0.968
84	0.952	0.971	0.993	0.981	84	0.985	0.983	0.996	1.000
85	0.942	0.971	0.972	0.964	85	0.993	0.987	0.970	0.999
86	0.950	0.996	0.973	0.977	86	1.002	0.992	0.944	0.997
87	0.947	1.021	0.963	0.987	87	0.981	0.974	0.926	1.007
88	0.921	1.002	0.925	0.958	88	0.959	0.956	0.909	1.017
89	0.875	0.855	0.916	0.833	89	0.948	0.814	1.000	0.828
90	0.902	0.875	0.951	0.877	90	0.969	0.883	1.021	0.865
91	0.921	0.907	0.978	0.894	91	0.989	0.951	1.042	0.902
92	0.945	0.947	1.016	0.945	92	0.996	0.966	1.043	0.946
93	0.956	0.991	1.038	0.998	93	1.003	0.980	1.043	0.990
94	0.953	0.998	1.016	0.992	94	1.008	0.978	1.023	0.999
95	0.961	0.992	1.017	0.972	95	1.013	0.975	1.004	1.008
96	0.962	0.973	0.993	0.950	96	0.976	0.961	0.958	0.995
97	0.938	0.881	1.031	0.919	97	0.973	0.915	1.074	0.956
98	0.948	0.892	1.032	0.920	98	0.993	0.911	1.113	0.952
99	0.965	0.912	1.037	0.929	99	1.014	0.907	1.153	0.947
100	0.993	0.938	1.055	0.955	100				
101	1.003	0.940	1.050	0.953	101	1.040	0.904	1.173	0.972
102	1.013	0.937	1.054	0.946	102	1.043	0.874	1.148	0.956
103	1.021	0.926	1.048	0.931	103	1.046	0.845	1.124	0.940
104	1.023	0.905	1.049	0.907	104	1.042	0.851	1.111	0.936
105	1.018	0.879	1.041	0.879	105	1.038	0.858	1.098	0.931
106	1.005	0.850	1.023	0.853	106	1.012	0.844	1.036	0.904
107	0.991	0.828	1.000	0.828	107	0.985	0.831	0.977	0.877
108	0.954	0.830	0.967	0.831	108	0.983	0.871	1.025	0.914
109	0.964	0.863	0.972	0.864	109	0.958	0.874	1.074	0.909
110	0.972	0.884	0.965	0.888	110	0.950	0.863	1.068	0.915

Table A-2 Differences Between Potential10 and ABLWT Wind Speed Ratios (R)

Difference Between Potential10 and ABLWT R Values (Potential10 - ABLWT)				
	Wind Direction			
	60	150	240	330
Minimum	-0.080	-0.091	-0.123	-0.083
Mean	-0.003	-0.001	-0.011	-0.016
Maximum	0.084	0.089	0.103	0.098

Turbine	Wind Direction			
	60	150	240	330
6				
7				
8				
9				
10				
11	0.003	-0.045	-0.031	-0.022
12	0.021	-0.013	-0.020	0.012
13	0.022	0.008	-0.020	0.026
14	0.028	0.018	-0.026	0.032
15	0.019	-0.009	-0.054	0.006
16	0.022	-0.026	-0.054	-0.003
17	0.027	-0.028	-0.048	-0.005
18	0.032	-0.036	-0.040	-0.020
19	0.031	-0.048	-0.023	-0.036
20	0.024	-0.010	-0.057	-0.016
21	0.050	0.047	-0.079	0.098
34	-0.042	-0.039	0.026	-0.045
35	-0.042	-0.026	0.054	-0.024
36	-0.061	-0.028	0.086	-0.022
37	-0.080	-0.055	0.029	-0.056
38	-0.077	-0.042	0.022	-0.027
39	-0.068	-0.021	0.024	-0.018
40	-0.053	0.007	0.020	-0.015
41	-0.014	0.048	0.054	0.009
42	-0.004	0.026	0.055	-0.024
43	-0.028	0.009	0.050	-0.043
44	-0.045	0.008	0.054	-0.054
45	-0.026	0.028	0.050	-0.021
46	-0.017	0.015	0.037	0.004
47	0.005	-0.018	0.041	-0.022
48	0.039	0.025	0.046	-0.022
49	0.036	0.019	0.007	-0.004
50	0.013	0.013	0.016	-0.006
51	0.033	0.048	-0.026	0.027
52	0.041	0.059	-0.034	0.022
53	0.030	0.048	-0.034	-0.001
54	0.008	0.011	-0.037	-0.039
55	0.002	-0.018	-0.010	-0.064
56	0.005	-0.020	0.023	-0.071
57	0.016	-0.018	0.014	-0.044
58	0.028	-0.006	0.006	0.008
59	0.018	0.034	-0.010	0.029
60	-0.005	0.010	-0.034	-0.013
61	0.024	-0.061	-0.036	-0.037
62	-0.013	-0.054	-0.056	-0.035
63	0.023	0.089	-0.040	0.055
64	0.010	-0.024	-0.105	0.039
65	0.048	-0.007	-0.095	0.048
66	0.053	-0.016	-0.104	0.009

Turbine	Wind Direction			
	60	150	240	330
67	0.071	0.007	-0.073	0.001
68	0.081	0.028	-0.045	-0.005
69	0.065	0.006	-0.045	-0.028
70	0.060	0.012	-0.043	-0.029
71	0.045	0.018	0.001	-0.022
72	0.041	0.008	0.040	-0.030
73	0.002	0.018	0.081	-0.005
74	-0.011	-0.056	0.093	-0.048
75	-0.012	-0.091	0.103	-0.012
76	0.027	-0.056	0.101	-0.025
77	0.030	-0.049	0.087	-0.024
78	0.084	-0.053	0.069	-0.030
79	0.071	-0.040	0.061	-0.021
80	-0.001	0.032	-0.017	-0.016
81	-0.017	-0.002	-0.007	-0.012
82	-0.027	-0.033	0.000	-0.004
83	-0.024	-0.016	0.006	0.006
84	-0.033	-0.011	-0.003	-0.019
85	-0.051	-0.016	0.002	-0.034
86	-0.052	0.005	0.029	-0.020
87	-0.033	0.047	0.037	-0.021
88	-0.038	0.046	0.016	-0.060
89	-0.073	0.041	-0.084	0.005
90	-0.067	-0.008	-0.070	0.012
91	-0.068	-0.044	-0.063	-0.008
92	-0.051	-0.019	-0.027	-0.001
93	-0.047	0.011	-0.005	0.008
94	-0.055	0.020	-0.008	-0.007
95	-0.051	0.016	0.013	-0.036
96	-0.014	0.012	0.035	-0.045
97	-0.035	-0.035	-0.043	-0.037
98	-0.045	-0.019	-0.082	-0.032
99	-0.049	0.005	-0.116	-0.018
100				
101	-0.036	0.036	-0.123	-0.019
102	-0.030	0.063	-0.095	-0.010
103	-0.025	0.082	-0.076	-0.010
104	-0.020	0.054	-0.061	-0.029
105	-0.020	0.022	-0.057	-0.052
106	-0.007	0.006	-0.014	-0.051
107	0.006	-0.002	0.024	-0.049
108	-0.030	-0.041	-0.057	-0.083
109	0.006	-0.011	-0.102	-0.045
110	0.022	0.020	-0.102	-0.027

Absolute Difference Between R Values
ABS(Potential10 - ABLWT)

	Wind Direction			
	60	150	240	330
Minimum	0.001	0.002	0.000	0.001
Mean	0.034	0.028	0.046	0.026
Maximum	0.084	0.091	0.123	0.098